

Alma Mater Studiorum - Università di Bologna

DOTTORATO DI RICERCA IN
INGEGNERIA CIVILE, CHIMICA, AMBIENTALE E DEI MATERIALI

Ciclo 35

Settore Concorsuale: 08/B2 - SCIENZA DELLE COSTRUZIONI

Settore Scientifico Disciplinare: ICAR/08 - SCIENZA DELLE COSTRUZIONI

WIND LOADING PREDICTIONS USING COMPUTATIONAL FLUID DYNAMICS

Presentata da: Jin Xing

Coordinatore Dottorato

Alessandro Tugnoli

Supervisore

Stefano de Miranda

Co-supervisore

Luca Patruno

Esame finale anno 2023

Acknowledgements

First, I would like to thank my supervisors, Prof. Stefano de Miranda and Prof. Luca Patrino, to whom I am deeply indebted for their invaluable guidance throughout my study. They give me great care and help me with patience and tolerance, making my time abroad a warm experience.

I want to thank each one in my research group for their friendship. Giorgio Cortelli, Antonio Maria D'Altri, Gregorio Bertani, Mao Xu, Luigi Manes, Nicolò Lo Presti, Simian Lei. Each of them has made the work at LAMC enjoyable.

My great appreciation is dedicated to my parents. I can never arrive at the end of this thesis without their understanding and support. I'm proud of my family for giving me such huge potential to achieve my aim.

Last but not least, I would greatly thank China Scholarship Council (CSC). This thesis and all my efforts at University of Bologna are dedicated to my country, China.

Jin XING
University of Bologna
May 15, 2023

List of Abbreviations

ABL	A tmospheric B oundary L ayer
AIJ	A rchitectural I nstitute of J apan
BLWT	B oundary- L ayer W ind T unnel
CFD	C omputational F luid D ynamics
CWE	C omputational W ind E ngineering
CAARC	C ommonwealth A dvisory A eronautical R esearch C ouncil
DNS	D irect N umerical S imulation
ESWL	E quivalent S tatic W ind L oad
HFFB	H igh- F requency F orce B alance
HFPI	H igh- F requency P ressure I ntegration
LES	L arge E ddy S imulation
LDA	L aser- D oppler A nomometry
PRFG³	T hree-dimensional P rescribed-wavevector R andom F low G enerator
PSM	P roper S kin M ode
POD	P roper O rthogonal D ecomposition
PIV	P article I mage V elocimetry
RANS	R eynolds- A veraged N avier- S tokes
ROM	R educed O rder M odel
SGS	S ub- G rid S cale
URANS	U nsteady R eynolds- A veraged N avier- S tokes
VBIC	V ariationally B ased I nflow C orrection
WALE	W all- A dapting L ocal E ddy-viscosity
WTT	W ind T unnel T est

Abstract of thesis entitled

Wind Loading Predictions Using Computational Fluid Dynamics

Submitted by

Jin XING

for the degree of Doctor of Philosophy

at University of Bologna

in May, 2023

Using Computational Wind Engineering, CWE, for solving wind-related problems is still a challenging task today, mainly due to the high computational cost required to obtain trustworthy simulations. In particular, the Large Eddy Simulation, LES, has been widely used for evaluating wind loads on buildings. The present thesis gives an assessment of the capability of LES as a design tool for wind loading predictions through three cases.

The first case is using LES for simulating the wind field around a ground-mounted rectangular prism with an aspect ratio of 1:3:5, standing in Atmospheric Boundary Layer (ABL) flow. The numerical results are validated with experimental results for seven wind attack angles, giving a global understanding of the model performance. The case with the worst model behaviour is investigated, including the spatial distribution of the pressure coefficients and their discrepancies with respect to wind tunnel results. Furthermore, the effects of some numerical parameters are investigated for this case, aiming at understanding their effectiveness in modifying the obtained numerical results.

The second case is using LES for investigating the wind effects on a high-rise building located in the city center of Milan, Italy, aiming at validating the performance of LES as a design tool in practical applications. The building has

been recently studied using wind tunnel tests. The numerical results are validated with the experimental results in terms of the distribution of the pressure statistics, the peak pressure values, and the global forces. The mesh sensitivity and the computational cost are also analyzed.

The third case is using LES for studying the wind effects on the new large-span roof over the Bologna stadium, aiming at informing the subsequent stages of the structural design. The dynamic responses are analyzed and design envelopes for the structure, representing the extreme actions expected for all structure members, are obtained. Although it is a numerical simulation before the traditional wind tunnel tests, i.e. the validation of the numerical results are not performed, the preliminary evaluations can effectively inform later investigations and provide the final design processes with deeper confidence regarding the absence of potentially unexpected behaviours.

Contents

Acknowledgements	ii
List of Abbreviations	iii
Abstract	v
1 Introduction	1
1.1 Background	1
1.2 Investigation approaches in Wind Engineering	6
1.3 Structure of the thesis	10
2 Simulation of a ground-mounted prism in ABL flow using LES: on overview of error metrics and distribution	13
2.1 Introduction	14
2.2 WTT and LES description	16
2.2.1 WTT description	16
2.2.2 LES description	17
2.2.3 Inflow	18
2.3 Results and discussion	22
2.3.1 Mesh	22
2.3.2 Pressure coefficients statistics	23
2.3.3 Global forces and moments	26
2.3.4 Prediction errors for 45° case	29
2.4 Sensitivity study	32
2.4.1 Mesh	32
2.4.2 Subgrid scale model	36
2.5 Conclusion	38

3	Wind loads prediction using LES: Inflow generation, accuracy and cost assessment for the case of Torre Gioia 22	41
3.1	Introduction	41
3.2	Case description	44
3.3	Wind tunnel tests	44
3.4	Numerical model	45
	3.4.1 Computational domain	46
	3.4.2 Mesh	48
	3.4.3 Models and numerical schemes	50
	3.4.4 Boundary conditions	50
	3.4.5 Synthetic turbulence	51
3.5	Results	53
	3.5.1 Inflow	53
	3.5.2 Mesh sensitivity	55
	3.5.3 Polar	59
	3.5.4 Global forces	64
	3.5.5 Peak pressures	65
	3.5.6 Computational costs	68
3.6	Conclusions	70
4	Early stages wind load assessment using Computational Fluid Dynamics: The new Bologna Stadium roof	73
4.1	Introduction	73
4.2	Numerical model	76
	4.2.1 Description of the stadium	76
	4.2.2 Numerical model for the wind flow simulation	77
	4.2.3 Synthetic turbulence inflow generation	81
4.3	Characterization of the flow field	83
	4.3.1 Instantaneous flow field	84
	4.3.2 Proper Orthogonal Decomposition	85
	4.3.3 Peak pressure distribution	87
	4.3.4 Global forces	88
4.4	Characterization of the structural response	91
	4.4.1 Mechanical model	92

4.4.2	Sensitivity studies	95
4.4.3	Design envelopes	98
4.5	Conclusions	102
5	Conclusions	105
5.1	Simulation of an isolated prism in ABL flow	105
5.2	Wind loads prediction for the Torre Gioia 22	106
5.3	Early stages wind load assessment for the new Bologna Stadium roof	106
A	Appendix	109
A.1	PRFG ³	109
A.2	VBIC	111
A.3	ESWL	112
	Bibliography	115

1 Introduction

1.1 Background

Wind, mainly driven by atmospheric pressure differences due to distinct solar radiation on the Earth's surface and the forces resulting from the Earth's rotation [1], is a natural phenomenon that influences our daily life in various aspects. On the one hand, wind is considered an important renewable energy source when it is used, for example, to power windmills and turbines in electricity production [2]. On the other hand, throughout history, a dramatic portion of property losses and deaths can be attributed to wind events like hurricanes, thunderstorms and tornadoes.



Fig. 1.1. Examples of wind energy utilization and wind hazards: the wind turbines on the Thorntonbank Wind Farm, Belgium [3] (left); the Tacoma Narrows Bridge collapsed due to wind-induced vibration in 1940 [4] (right).

People have been starting to pay attention to wind effects on structures since ancient time, probably around the 17th century, when the painting of the wind

god—Fujin—was created by Tawaraya in Japan [5]. Early wind engineering can be traced back to the 19th century when wind forces on some important structures were investigated [6]. Wind tunnels were invented in the late 19th century and evolved in the early 20th century, mainly serving the development of aviation. Some of them, for example the Eiffel wind tunnel in Paris, also worked and are still used in the studies of wind effects on structures [7]. As a scientific discipline, Wind Engineering was pioneered by Jack Cermak, who developed the first boundary layer wind tunnel (BLWT) for simulating the wind flow in the Atmospheric Boundary Layer, ABL, in 1975 [8].

In particular, the Wind Engineering community is interested in wind effects on structures, considering that wind-related actions might significantly threaten structural integrity, habitability and serviceability, especially for buildings susceptible to wind actions. The investigation and prediction of wind effects on structures have been guided by the famous "Davenport chain" since it was published in 1961 [9]. It is for calculating the wind loading on a particular building or structure, where the effects of local wind climates, local wind exposure, structural aerodynamic characteristics and the potential for load increasing due to possible wind-induced resonant vibration are embedded [10], as shown in Fig. 1.2.



Fig. 1.2. The Davenport wind loading chain [10].

Specifically, the local wind climate is described in statistical terms related to the reference wind velocity, the wind direction, the recurrence interval and the dominating storm system of the region [5]. Establishing these statistics usually starts with gathering wind speed and wind direction data from local meteorological stations. The collection of the data needed to characterize the local wind climate, which is outside the scope of the present thesis, is a complex operation which requires to tackle numerous source of errors and collect

1.1. Background

data for numerous years in order to obtain statistically significant evaluations of rare events probabilities [11–13]. In recent years, new challenges need to be tackled, such as the consideration of rapid climate changes, which might make predictions based on historical data unreliable [14]. Such topics are still the object of intense research at the time of writing. The extreme wind velocity associated to each return period is the main quantity of interest for the evaluation of the wind loads to be used for serviceability and ultimate strength structural checks. An extreme distribution model is required to obtain the peak values from the recorded velocity series [15–17].

The influences of terrain roughness and topography are reflected by local wind exposure factors. These factors are usually integrated into the so-called wind profile that describes the mean wind velocity distribution as a function of height (within ABL), following a power law [18] or a logarithmic law [19]. Ideally, the mean wind speed decreases with increasing terrain roughness. Moreover, the influence of the orographic condition, e.g. the presence of hills and cliffs etc., must be also considered, as they might lead to remarkable local increase of the wind velocity. This adds further uncertainties to wind loads evaluations, especially when simplified procedures are adopted. In fact, the natural terrain roughness is not homogeneous. In addition, the obstacles, generating speed-up effects or channeling effects, might present simultaneously with the variation of the roughness [20]. Overall, the extremely high variability of roughness distribution and topographic conditions around the site of interest prevents the possibility to use simplified formulations based on characterizations which use just a few parameters. As a result, when accurate evaluations are needed, the use of standards and codes of practices is insufficient, and wind tunnel tests and/or detailed numerical simulations are used [21, 22].

Apart from the mean component, the fluctuating part of the instantaneous wind velocity is of critical importance for the determination of wind loads. It characterizes the turbulent nature of the flow and has significant effects on the structures immersed in the ABL. Qualitatively speaking, turbulence is a mixture of eddies (or vortices) with different length scales, moving and interacting with each other. Quantitatively, turbulent flow occurs when the Reynolds

number ($Re = UL/\nu$, where the U is the flow speed, L is the characteristic dimension of the flow and ν is the kinematic viscosity of the fluid) exceeds a critical value (2500-5000, according to the experimental investigations in tubes [23]). In a word, turbulence is a chaotic, irregular and stochastic flow state, which, taking the turbulent wind as an example, gives dynamic effects to the structures immersed in it [24].

The ABL turbulence can be described in terms of the intensity of three velocity components and their integral length scales in the Cartesian directions and/or the turbulence spectrum [23, 24]. As it is well-known, both the turbulence intensity and the turbulence integral length scale dramatically affect the structural wind loads [25, 26]. For instance, the turbulence intensity has been found to influence the mean pressure field around two-dimensional bodies, especially influencing the flow separation and reattachment points [27]. Also, the turbulence integral length scale influences the pressure distribution on the building surfaces [28]. The effects of these two characteristics are interrelated since they describe the vortexes energy from different perspectives [29]. It is widely known that the accurate reproduction of the turbulence characteristics is crucial to the wind loading prediction [30, 31]. Therefore, techniques for controlling the turbulence characteristics in experimental wind tunnel tests and numerical simulations have been extensively investigated by the community of Wind Engineering [32–34].

The next circle of the chain is the structural aerodynamic characteristics. Most man-made structures are bluff bodies. They are characterized by flow separation, reattachment and the well-known vortex shedding in their wake, formed when interacting with a free-stream flow [35]. Three major types of wind pressure (or load) regions are generated when a turbulence flow impinges on a bluff body: a high and positive pressure region on the upstream face, several negative pressure regions on the side faces which occurs when the shear layers are formed and a negative pressure region in the wake or under the fully separated shear layers [36]. The aerodynamic behaviour of structures differs depending on their geometrical shape and size. In addition, it is well-known that minor geometrical details might play an important role in defining the aerodynamic behaviour [37]. The classical example is the radius of curvature

1.1. Background

of corners, which might strongly affect the flow arrangement, especially in smooth incoming flow conditions [38]. Wind Engineering aims to quantify the aerodynamic actions of different sorts of structures. Usually, wind loads are distinguished into the mean contribution, buffeting forces, forces originated by the local unsteady aerodynamic behaviour and aeroelastic forces. The first ones are related to the mean incoming wind, the second ones are due to the presence of turbulence in the incoming flow, the third ones are due to local flow features such as separation bubbles and vortex shedding in the wake and, finally, aeroelastic forces are generated by the coupling of aerodynamic forces and the structural motion. Such contributions in practice are not as clearly distinguishable as they have been presented, being all interconnected to each others, but the classification is fundamental in order to individuate the main mechanisms which lead to the generation of wind loads [39].

The following circle in "Davenport chain" is dynamic effects, to be intended as the evaluation of the structural response, starting from the knowledge of the wind actions. On such regard, important aspects to be considered are the presence of strong resonant effects, which might be present especially when vortex shedding synchronizes with the structural motion, also leading to aeroelastic effects such as lock-in. In this context, it is necessary to distinguish between analysis aimed at dimensioning the structure with respect to its ultimate strength and those aimed at checking for its serviceability. In all cases, if excessive resonant-dominated vibrations are foreseen, it is possible to use moderating devices, typically in the form of dampers, in order to moderate them [40, 41]. However, the evaluation of dynamic responses of structures by means of simplified procedures is limited by the difficulty of considering the vortex-shedding and analytical methods are widely investigated [42, 43].

In the end, Davenport pointed out that there should be criteria to judge the acceptability of the predicted wind loads and responses based on statistical considerations, due to the inherent stochastic nature of wind. As regards ultimate strength analyses, peak forces/moments in all structural members must be evaluated. As regards serviceability, the wind-induced acceleration is a key requirement, and the perception of vibration and acceleration can influence the body comfort of the occupants [44, 45]. Other factors, such as the

useability (pedestrian safety and comfort) of the outdoor areas and immediate surroundings should be considered [10, 46].

As described above, it is no doubt that evaluating wind loads on structures can never be a straightforward task. As pointed out by Davenport, the sequence of considerations leading from the wind climate to the checking of design requirements acts like a chain, in which the weakest element defines the overall reliability of the obtained results [10].

1.2 Investigation approaches in Wind Engineering

In application and research in Wind Engineering, there are three major approaches to evaluate the wind effects on structures: field measurements [47–50], reduced-scale wind tunnel tests [51–54] and numerical simulations [55, 56].

Field measurements can obtain reliable wind characteristics and real-life wind-induced responses of structures, without introducing approximations and simplifications. Unfortunately, the tests are strongly limited by equipment, time, weather and other uncontrollable parameters [57]. In particular, while the investigation of the structural response itself is straightforward, it is often difficult to characterize the incoming wind in a sufficiently detailed way in order to link the measured structural response to the wind excitation. Obviously, such techniques can be used for monitoring and validation but cannot be used in the design stage [58, 59].

Wind tunnel tests are indispensable for wind loading assessments, currently representing the traditional gold standard in Wind Engineering. It primarily relies on the BLWT, proposed in the 20th century [60, 61]. BLWTs are generally equipped with a long test section (open-circuit or closed-circuit) and a data-acquisition system. The former is used to reproduce the ABL, which differs from the aeronautic wind tunnel equipments in the sense that the ground roughness effects are reproduced using elements like spires and carpets. The latter is used to monitor the wind loading and structural responses. Two examples of the wind tunnel equipment are presented in Fig. 1.3.

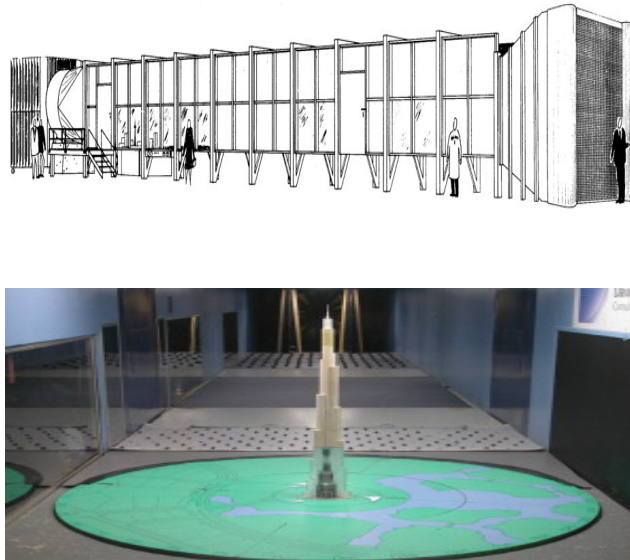


Fig. 1.3. The earliest BLWT conceived by Davenport [62] (up) and a model in a BLWT of RWDI [63] (down).

The commonly adopted data-acquisition techniques for pressure/force in wind tunnel tests can be subdivided into three types: High-Frequency Force Balance (HFFB), High-Frequency Pressure Integration (HFPI) and aeroelastic models. The HFFB measures the forces including shear forces, torque and bending moments at the base of models, estimating the dynamic structural responses based on traditional modal analysis with a linear mode shape assumption [64, 65]. So it only works well for building vibrating under fundamental modes but not for the super tall structures whose vibration under higher order mode is significant [66]. The HFPI measures pressure using pressure taps equipped on the exposed surfaces of the buildings. It is suitable for buildings with complex shapes, being not based on considerations involving the mode shapes [67]. However, integrating the point-measured pressure requires a sufficient density of pressure taps, which poses difficulties for buildings with intricate shapes. Finally, the aeroelastic model tests the dynamics including motion-related loads, even considering the structural damping omitted by the other

two methods. As a result, it can offer the most accurate measurements, but its application is quite limited due to high costs.

In addition, the flow velocity can be monitored in wind tunnels, instead of being indirectly determined by pressure distribution (measured using, e.g. Pitot tube), using anemometry such as Laser-Doppler Anemometry (LDA), hot wire and hot film anemometry and Particle Image Velocimetry (PIV). They are widely applied, solely or cooperatively in the velocity-acquisition of wind tunnel tests [68] and advanced techniques are under extensively development by the Wind Engineering community at the time of writing [69]. Specifically, the hot wire or hot film probes methods can be easily operated and are relatively cheap but would introduce perturbations in the flow field. The LDA could compensate that without intrusion but are relatively expensive. The PIV is the most well-adapted tool for aerodynamic investigations, allowing to provide information of three velocity components, although its sampling frequency and capability may be limited by the camera and sensor location.

During past decades, the computational power has dramatically grown, enabling the progress in hardware/software and the development of computational methods. Owing to this, Computational Fluid Dynamics (CFD) has become a technical tool which can be practically used [70]. Computational Wind Engineering (CWE) is the usage of CFD for solution of problems encountered in Wind Engineering [71].

Three main approaches of CFD are available. Their main characteristics are briefly introduced in the following, without aiming at a rigorous and complete exposition, for which the reader is invited to consult the dedicated relevant literature [72–75].

Direct Numerical Simulation (DNS) is the most accurate and rigorous approach. It solves the Navier-Stokes equations for all scales, from the energy-dominating eddies to the energy-dissipative Kolmogorov-scale structures. As a result, it requires extremely high computational resources and can hardly be used for engineering problems.

Large Eddy Simulation (LES) is nowadays becoming the most popular CFD

tool and is expected to become the dominant approach for wind forces evaluation. Differently from DNS, LES only directly solves the turbulence eddies with the scale larger than the grid scale of the model mesh, considering that these structures are the ones which, for sufficiently fine meshes, contain the majority of the energy in the turbulent structures. For the smaller eddies so-called Sub-Grid Scale, SGS, model is chosen. This choice mainly relies on the observation that the large scales are the most difficult to be modeled, as their characteristic strongly depend on their generation mechanism. On the contrary, small-scale turbulence, originated by the decay of large-scale ones, are known to have a simpler and more universal structure, mainly characterized by isotropy. Consequently, the choice on mesh resolution and SGS model are the critical step of set-up of LES. In fact, an acceptable compromise between the numerical accuracy and calculation costs is fundamental to the viability of a LES because, on the one hand, infinitely refining the mesh leads a LES to an unaffordable DNS, on the contrary, a LES with an insufficient mesh resolution will give inaccurate results. There are many SGS models developed for LES, for instance, the famous Smagorinsky model [76], wall-adapting local eddy viscosity (WALE) [77], to cite a few.

Reynolds-averaged Navier-Stokes (RANS) is another important CFD approach, characterized by lower fidelity compared to LES but with higher computational efficiency. RANS is meant to reproduce only the time-averaged flow field, thus disregarding any turbulent structure. In reality, the distinction between turbulent structures and non-turbulent vortical structures is mainly conventional and so, in practice, Unsteady RANS (URANS) is available and commonly adopted, leading to unsteady flow fields which are usually extremely simplified with respect to the physical ones. Many RANS/URANS models are currently available, being probably the most well-known one the $k-\epsilon$ model, while the most commonly adopted one in the field of CWE is the $k-\omega$ SST model, due to its well-known relatively good performance in bluff-body aerodynamics.

During past decades, the hybridization of different CFD models has been proposed, for example, the hybrid RANS-LES. The hybrid RANS-LES methods are found to have a better prediction than RANS and a better efficiency than

LES, although with more uncertainties in terms of mesh and Reynolds number dependency. Their development is currently ongoing significant interest to the Wind Engineering community [78].

Using CWE for solving wind-related problems is still a challenging task today, mainly due to the high computational costs required to obtain trustworthy simulations. This can be contrasted with the use of CFD for the study of the pedestrian wind environment, for which CFD is widely used [79]. The difference between such two apparently similar applications stays in the fact that accurately predicting the pressure field is generally more difficult than predicting the overall velocity field, and that the consequences of inaccurate predictions are, much more relevant for wind loading assessments than in pedestrian wind comfort ones. As a results, pedestrian wind comfort studies are usually performed using URANS approaches [80], while wind loading almost always requires the use of computationally expensive LES models. In particular, LES has been used for evaluating wind loads acting on buildings with simple shapes [81] and complex shapes [82]. It can be foreseen that, with the growth of the computational power, CWE based on the extensive use of LES has the potential to become an alternative to wind tunnel experiments for many studies, and its value as a complementary investigation tool to be used alongside traditional wind tunnel tests is already clearly established at the time of writing.

1.3 Structure of the thesis

The present thesis gives an assessment of the capability of LES as a design tool for wind loading predictions through three cases. These cases are analyzed and presented in the order of increasing complexity. In particular, the objectives of the three studies are detailed in the following:

1. The first case is used to assess the performance of LES for simulating the wind field around a regular-shaped building model. For that purpose, a ground-mounted rectangular prism with an aspect ratio of 1:3:5, standing in ABL flow, is tested. This geometry is available in the wind

tunnel experiments database constructed by the Tokyo Polytechnic University (TPU), Japan. As it is well-known, the flow around rectangular cylinders is characterized by flow detachment, reattachment and shedding in their wake. While there is little doubt that well-resolved LES can provide reliable and accurate simulations of such kind of flow, the required computational resources are still extremely high, so that it is of interest to investigate the model performance also in sub-optimal cases, in which relatively coarse meshes are adopted.

The numerical results are validated with experimental results for seven wind attack angles, including the perpendicularly attacking flow and obliquely attacking flow, to give a global understanding of the model performance. Then, to get an in-depth sight of the model errors, the case with the worst model behaviour is detailed. For this case, the spatial distribution of the pressure coefficient statistics and their discrepancies with respect to wind tunnel results are analyzed. Furthermore, the effects of some numerical parameters, such as the mesh resolution in the vicinity of the building and the SGS model, are investigated, aiming at understanding their effectiveness in modifying the obtained numerical results.

2. The second case is used to validate the performance of LES as a design tool in applications. To this purpose, the case of Torre Gioia 22, a high-rise building located in the city centre of Milan, Italy, and recently studied using wind tunnel tests by RWDI is considered. The tower has a relatively complex shape and is located in a densely urbanized area, so that surroundings had to be carefully reconstructed. Being a case characterized by real complexity, numerous aspects had to be considered and compromises between sometimes opposing necessities found. Finally, the case is aimed to provide a better insight into the critical aspects which characterize such simulations and loads of practical considerations useful for their setup.

In the study, the numerical results are carefully validated with the experimental results in terms of the distribution of the pressure statistics,

the peak pressure values and the global forces. The mesh sensitivity and the computational costs are also analyzed.

3. The third case is used to evaluate the efficiency of LES for complementing the traditional wind tunnel tests during the early design stages. For this purpose, the new large-span roof over the Bologna stadium is simulated. It is a study performed before the WTT, so it is not the intention to validate the numerical results but to inform the subsequent stages of the design. For this case, the structural response is calculated by means of dynamic analyses, arriving to the definition of the design envelopes representative of the extreme actions expected for all structural members.

The critical wind loading conditions are identified and the structural response sensitivity to damping is investigated. Such information can be extremely precious in the early stages of the design process, as it allows to take eventual countermeasures before arriving to the WTT in the final design stage, usually adopted only as confirmation of the already adopted design choices.

For all the cases, the inflow conditions, representative of the ABL are generated using a turbulence synthesizer called PRFG³. It is a spectral method, which is able to provide control on the three components of turbulence intensity and nine components of turbulence integral length scale, developed at University of Bologna [33, 83]. A brief introduction of this method is reported in Appendix A.

The Chapter 2 - 4 of this thesis are composed of articles which have been published in international peer-reviewed journals. Consequently, the text as well as figures, tables and equations are included without any modifications, although there might be repetitions or a different notation of a symbol/unit among the chapters.

2 Simulation of a ground-mounted prism in ABL flow using LES: on overview of error metrics and distribution

The accuracy of wind loading predictions using Large Eddy Simulation (LES) is usually influenced by numerous model parameters, which can influence the obtained results. The validation of numerical simulations with traditional Wind Tunnel Test (WTT) is still an important task, necessary to increase our *a priori* knowledge of possible inaccuracies and set up mitigation strategies. In this study, LES is used to simulate the wind fields around an isolated model high-rise building, under seven wind attack angles and validated with WTT results. The influence of various settings and parameters on the model performance is studied. For the angle of attack showing higher inaccuracy, different mesh refinement strategies and turbulence models are tested. Results indicate that LES can accurately predict the mean and local maxima of the pressure coefficients for both perpendicular and skew wind attack angles, as well as reproducing global forces and their envelopes with very good accuracy. Conversely, pronounced errors are found in the prediction of the pressure coefficient standard deviation and the local minima. The highest deviations between LES and WTT are found close to the leading edge in correspondence of flow separations which are observed in WTT and not in LES for skew flows. The addition of boundary layer cells and the use of different subgrid models have very limited effectiveness in modifying the obtained results for the analysed case.

2.1 Introduction

Large Eddy Simulation, LES, is known to be a powerful tool for the investigation of wind effects on structures such as high-rise buildings [70, 84–86]. However, comparison with traditional Wind Tunnel Test (WTT) sometimes show discrepancies, so that their validation and the individuation of critical aspects which might affect results is still an important research activity. Numerous studies can be found in the literature validating LES results in terms of wake flow characteristics [87, 88], global aerodynamic forces [89, 90] and pressure distribution [91–93]. The usefulness of such validations mainly consists in the individuation of critical aspects which can be sometimes moderated by appropriate modelling choices. When moderation strategies are not found or lead to excessive computational burden, their individuation anyway allows to build up knowledge, which can help in correctly interpreting results obtained by numerical models when WTT results are not available.

From the studies above and analogous works [94, 95], it can be found that the model performance of LES is usually good but, in some cases, sensitive to various model parameters. Among them, the accurate reproduction of flow characteristics in the Atmospheric Boundary Layer (ABL) is known to be crucial for the evaluation of wind effects on structures [31, 96]. Nevertheless, numerous other factors can influence the simulation [97–99], which include, as pointed out in [100], ground roughness, subgrid scale model, domain size, near-wall treatment and sensitivity to mesh and timestep.

Numerous contributions have been devoted to investigate the influence of some of the aforementioned model parameters on the model accuracy. Unfortunately, due to the variability of the adopted computational setup and analysed flows, contradictory results are sometimes founded.

In particular, [101] assessed the effects of the mesh type and boundary mesh on the time-averaged and fluctuating wind characteristics around an isolated high-rise building standing in ABL. They found that the case with hexahedral cells has the best agreement with experiments. They also found that the boundary layer mesh does not improve the numerical accuracy in any circumstance, despite the fact that the non-dimensional wall distance (y^+) is often

2.1. Introduction

considered to be a very important quantity to be controlled. [102] showed that the choice of the Sub-Grid Scale (SGS) model does impact the flow field. The wall adapting local eddy viscosity (WALE) model was found to be the most suitable among the tested models including Smagorinsky-Lilly model, Dynamic model, kinetic energy sub grid scale model and wall modelled LES. [103] examined the effect of mesh resolution and different SGS models, on the prediction of the pedestrian level wind fields around building arrays. They observed that the dynamic Smagorinsky-Lilly method gave the best model performance and recommended appropriate values for time step and sampling period.

The aim of the present paper is to assess the numerical accuracy of LES in predicting wind loads on a high-rise building and to study the influence of some important model parameters on the accuracy of the obtained results. The high-rise building model is an isolated flat-topped box with an aspect ratio of 1:3:5, standing in an ABL. It is one of the high-rise building models from the public wind tunnel database constructed by Tokyo Polytechnic University (TPU), Japan, which have been considered also in some of the already available contributions [100, 104–106].

Firstly, the numerical results are compared with WTT data in the form of several model performance metrics for 7 angles of attack ranging from 0° to 90° . Then, for the worst case, corresponding to a skew flow impinging at 45° , the spatial distribution of the pressure coefficient statistics (i.e. time-average, standard deviation and peak values) and the corresponding Prediction Error (*PE*), defined as the difference between numerical and experimental results, are analysed. For such worst case, different numerical setups are evaluated varying mesh configuration and testing three SGS models, namely, WALE, $k - \omega$ SSTSAS and Smagorinsky.

The paper is organized as follows. The descriptions of WTT and LES are provided in the next section, along with the procedure used to generate inflow conditions. Then, the numerical results are validated in Sec. 2.3. Subsequently, the sensitivity studies of the *PE* to the mesh configuration and the SGS model are provided in Sec. 2.4. Finally, conclusions are drawn in Sec. 2.5.

2.2 WTT and LES description

2.2.1 WTT description

The WTT were performed in the Boundary Layer Wind Tunnel (BLWT) of the TPU, Japan. It is an open circuit tunnel with 2.2 m width and 1.8 m height. The ABL in the experiments was generated through spires and square blocks acting as roughness elements. It corresponds to a Category IV in the Architectural Institute of Japan (AIJ) standard [107]. The wind speed at building height is around 11.11 m/s, and the stream-wise turbulence intensity ($I_{u_{WTT}}$) is approximately 15%.

The tested model is a flat-topped prismatic box with 0.5 m height (H) and 0.3 m (L) * 0.1 m (W) rectangular cross-section. The length scale reduction factor of the experiments is 1:400, leading to a building height equal to 200 m in real scale. 480 wind pressure taps are positioned on the four side faces, sampling synchronously with a frequency of 1000 Hz for a duration of 32.8 s. The origin of the coordinate system is the center of the building base. The geometry of the building is presented in Fig. 2.1 (a).

Incidence angles ranging from 0° to 100° with an increment of 5° are considered in WTT. The 0° is defined as the condition in which the flow is moving along the $+x$ direction and it is perpendicularly hitting the long building side, as indicated in Fig. 2.1 (b). The complete database and detailed description of the WTT are publicly accessible [108].

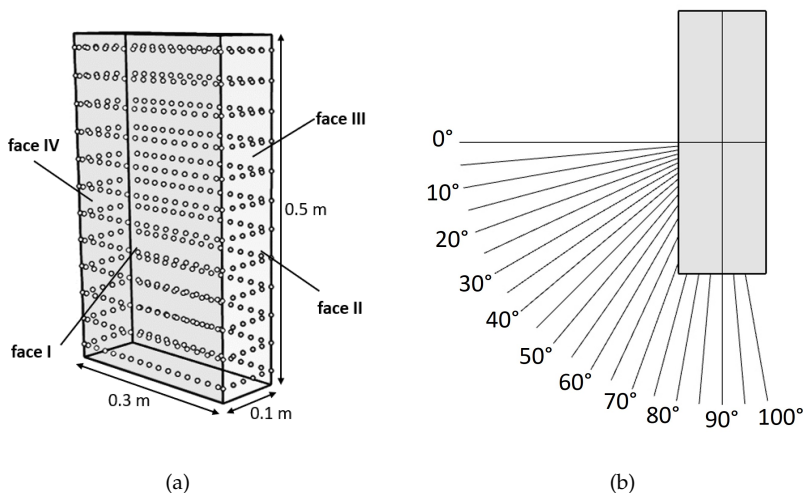


Fig. 2.1. The geometry of the building (a) and the wind incidence angles from 0° to 100° (b).

2.2.2 LES description

LES are designed to reproduce the WTT using the open source software OpenFoam v6.0. A 3D view of the computational domain is presented in Fig. 2.2 (a). The domain has the dimensions of 3 m, 2.2 m and 1.8 m in stream-wise, lateral and vertical directions, respectively. The distance between the inlet patch and the building location is 1 m, which equals the double of the building height H . The blockage ratio of the simulations is approximately 3.0% for 0° and is 1.0% for 90° , which are both lower than recommendations [109].

The turbulent flow at the inflow patch is generated using a synthetic turbulence generation technique called PRFG³. It is an extended version of the Prescribed-wavevector Random Flow Generator (PRFG) [110], aiming at giving control over three-dimensional spectral densities, in other words, explicitly targeting all integral length and time scales of turbulence. Interested readers are invited to the references [110, 111] for details regarding the method. The top and two sides of the domain are treated as symmetry conditions, mimicking the effect of wind tunnel walls. The domain bottom and the building

surfaces are treated as walls. In particular, the ground of the domain is modeled as a rough wall with a roughness height of 0.015 m (model scale) and a roughness constant of 0.5. The building surfaces are modeled as smooth walls. A rough wall, with a roughness height of 0.015 and a roughness constant of 0.5, is applied to the ground. An inlet-outlet condition is used for the outlet patch.

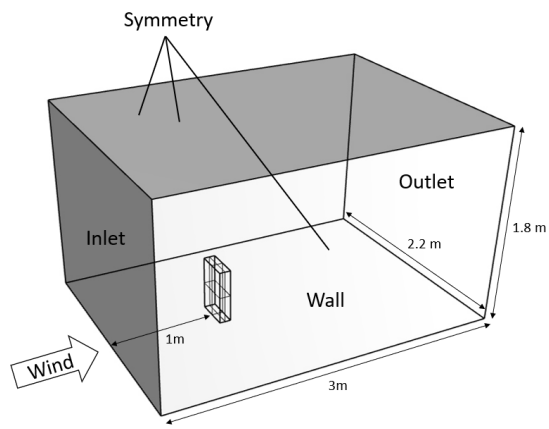
An overview of the mesh is shown in Fig. 2.2 (b). The SnappyHexMesh is used for meshing. A rotor-stator method is adopted. Specifically, the rotor is a cylinder of radius of 0.25 m (reduced scale) with an axis oriented along the z -direction passing through the building center. It is rigidly rotated when studying the wind effects at different attack angles without re-meshing the geometry. The stator is the rest of the domain, as indicated in Fig. 2.2 (b) and (c). As can be seen, a hexahedral mesh is used for the whole domain and cell expansion gradients are used, leading to the fact that the mesh size at the domain top and outlet is around two times bigger than at the domain center. The mesh size is around 0.016 m at the inflow patch and it is around 0.004 m up to a distance of 0.1 m from the building surfaces. This yields the cells number for the building H , L and W to be 125, 75 and 25, respectively, which fulfills the requirements in [98]. The total cells number is around 1.8 million.

As for the numerical schemes utilized for the simulations, the pressure velocity coupling is imposed using the PISO algorithm. The time discretization is performed using the Crank Nicolson scheme with a blending coefficient of 0.85. The face fluxes for all the quantities are calculated using the bounded Gauss linear scheme except for the velocity which is calculated using the second-order LUST scheme. The k -Equation is used as the LES subgrid scale turbulence model. The non-dimensional time step ($\Delta t * (U_r / H)$) for the calculation is 0.01, yielding the Courant number of the calculation to be around 3.0 on average and only attains 6.0 in some small size cells.

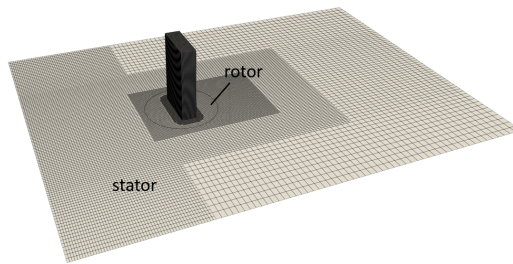
2.2.3 Inflow

As mentioned before, synthetic turbulence is applied at the inflow. In particular, PRFG³ is used for generating the ABL flow. It targets a Category IV profile

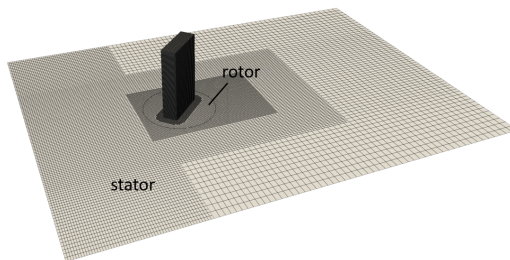
2.2. WTT and LES description



(a)



(b)



(c)

Fig. 2.2. The computational domain with boundary conditions (a) and the overviews of the mesh distribution: 0° (b) and 45° (c).

in AIJ standard code, which is in agreement with the one adopted in WTT. The mean velocity and the along-wind turbulence intensity, I_u , distribution along height are set following the power law in the code prescription, being 0.27 the exponential and 550 m the reference height of ABL. The turbulence intensities in y and z direction are set to be 0.75 and 0.5 times of the turbulence intensity in x direction, respectively. We mention that in order to obtain the target wind field characteristics at the building location, the turbulence intensity of each velocity component has been increased of about 20% at the inflow to compensate for the energy dissipation between the inflow and the building location. The reference velocity, U_r , is chosen as the time-averaged wind speed at the reference height, H_r , which is the height of the building.

In order to check the performance of the turbulence generator, an empty domain with the synthesized turbulent inflow condition is tested first. The wind profiles at the location where the building will be placed are shown in Fig. 2.3. As can be seen, the mean wind speed profiles from the AIJ code, WTT and LES agree well with each other. In the same figure the turbulence intensity profiles are reported, being I_{u_LES} , I_{v_LES} and I_{w_LES} at H_r equal to 12%, 10% and 8%, respectively. Furthermore, the simulated turbulence integral length scales at H_r , evaluated from velocity time-histories and assuming frozen turbulence, L_{ux} , L_{vx} and L_{wx} , nondimensionlized to the WTT length scale, are 0.375, 0.2 and 0.125, respectively.

2.2. WTT and LES description

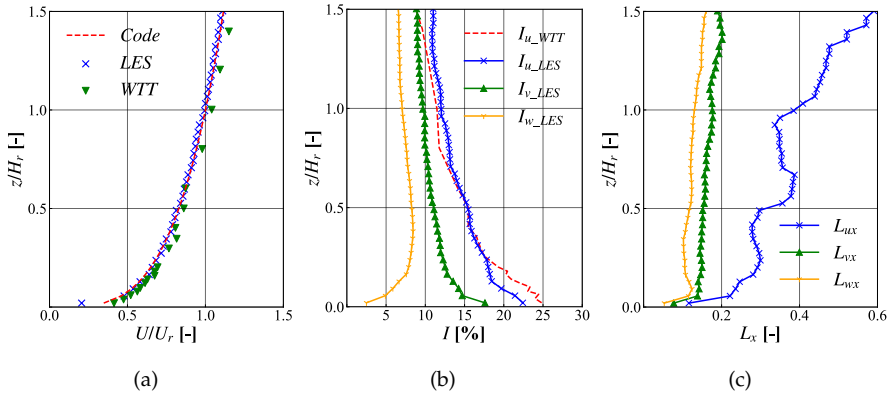


Fig. 2.3. The turbulence characteristics of the wind fields in WTT and LES: (a) mean wind speed (b) turbulence intensities and (c) integral length scales.

The power spectral density of the velocity components u , v and w at the building height are presented in Fig. 2.4 (a), (b) and (c), respectively, showing a good agreement with the von Karman (indicated as *Tar.Karman* in the figures) wind spectrum up to the cut-off frequency, equal to approximately 65 Hz. Overall, the simulated turbulent inflow shows a satisfactory agreement with WTT and with the targeted profiles.

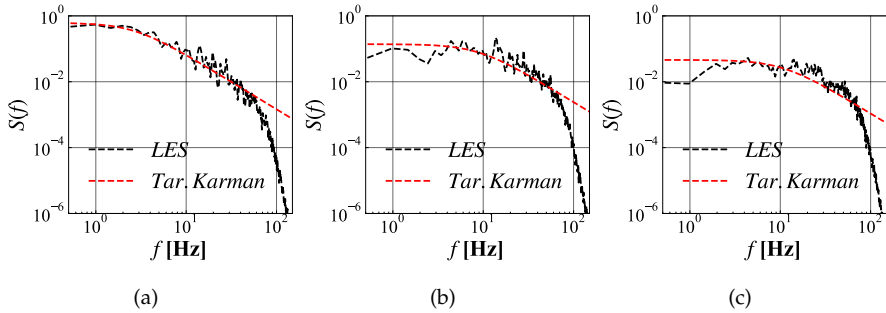


Fig. 2.4. The power spectral density of three velocity components at the building location: (a) u , (b) v and (c) w .

2.3 Results and discussion

2.3.1 Mesh

As is well known, it is ideally necessary to ensure that results obtained using numerical simulations are independent from the adopted mesh size [109]. When using LES, it is actually more appropriate to state that results of interest shall be independent or vary within acceptable ranges with the mesh size, as a complete independency is actually not expected. We start by considering the case at 0° . For such case, we use three meshes, namely, coarse mesh (CM), medium mesh (MM) and fine mesh (FM), to check the grid dependency of the numerical solution. The number of cells of the three meshes are 0.1, 1.8 and 6.6 million, respectively. In other words, the ratio between the cell size in each direction between two consecutive meshes is approximately 1.5, following the suggestion in [112]. A summary of the characteristics of the three meshes is provided in Tab. 2.1. The computational resources needed to perform each simulation are also reported.

Table 2.1: Characteristics of the three meshes used for the present investigation.

	cells number (million)	cells number for each building side			Δt (-)	computational time (CPU - hour)	
		H	L	W		y+	
CM	0.1	56	26	9	0.02	25	110.0
MM	1.8	145	73	23	0.01	215	46.0
FM	6.6	220	113	35	0.005	1212	30.0

In order to characterize the obtained results, the time-average, rms, maximum and minimum values of C_p , respectively denoted as \bar{C}_p , C'_p , \hat{C}_p and \check{C}_p , are considered. Peak values are calculated by fitting to the two-minutes extreme using a Gumbel cumulative probability distribution function and then, adopting the well-known shifting property of the Gumbel distribution [113], to extract the 10-min extremes associated with a non-exceedance probability equal to 80%, in agreement with the Cook and Mayne approach [114].

Figure 2.5 presents the scatter plots of the C_p statistics from simulations using the aforementioned three meshes. As shown in Fig. 2.5 (a) - (c), no remarkable differences in terms of \bar{C}_p , C'_p and \hat{C}_p can be observed, except from a

very slight underestimation of \bar{C}_p in CM (the difference is approximately 0.1). Regarding \check{C}_p , results obtained from CM, only arrive at -2.5. However, they attain approximately -4.0 in the simulations with MM and FM, showing no apparent variation between the two meshes. Some localized points have more severe extreme suction in MM and FM than in CM, while the results from CM are closer to WTT, which seem nonintuitive. However, as indicated in an analogous work [115], a finer grid model might underestimate the turbulence dissipation rate and give a higher turbulent kinetic energy prediction, yielding overall better performance with coarser meshes. In all, results highlight that CM is probably excessively coarse, as it substantially differs from the other two. Results appear to be quite similar with respect to all analyses quantities for MM and FM, so that MM is chosen for the next analyses.

2.3.2 Pressure coefficients statistics

After choosing the mesh size to be used, we proceed at simulating seven attack angles, equally spaced between 0° and 90° . The LES results are compared with WTT results for all the simulated wind attack angles in the form of three error metrics, namely, the mean error (ME), the standard deviation of error (SE) and the coefficient of determination (R^2) [94], as reported below

$$ME = \frac{1}{N} \sum_{i=1}^N (LES_i - WTT_i), \quad (2.1)$$

$$SE = \sigma(LES - WTT), \quad (2.2)$$

$$R^2 = \frac{(WTT - \overline{WTT}) * (LES - \overline{LES})}{\sigma_{WTT} * \sigma_{LES}}, \quad (2.3)$$

where the subscript i represents the pressure tap number and the total number of monitors, N , is equal to 480. The \overline{WTT} (or \overline{LES}) represents the time-average and σ_{WTT} (or σ_{LES}) represents the standard variation of the WTT (or

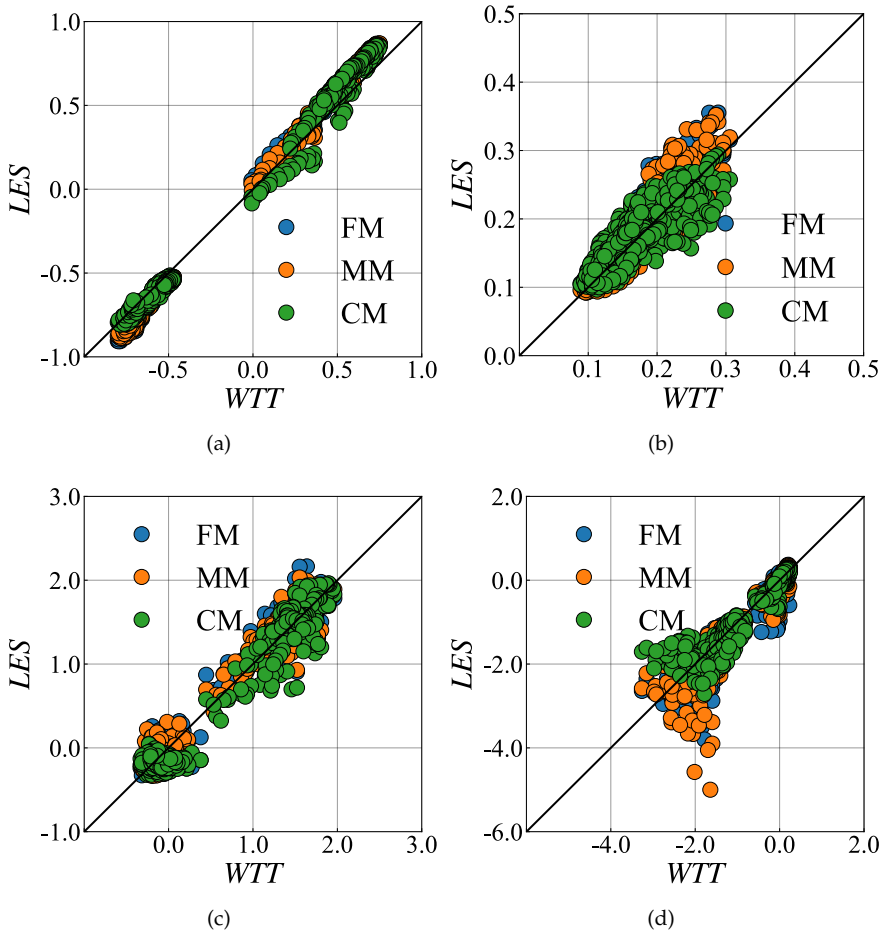


Fig. 2.5. Comparisons of LES results using different mesh resolutions with WTT: (a) \bar{C}_p , (b) C'_p , (c) \hat{C}_p and (d) \check{C}_p .

LES) dataset. The error metrics regarding different C_p statistics for all the considered cases are reported in Tab. 2.2. Notice that ME for \bar{C}_p is not reported, as it might be simply related to the choice of the reference pressure, so being irrelevant.

2.3. Results and discussion

Table 2.2: Error metrics of the \bar{C}_p , C'_p , \hat{C}_p and \check{C}_p for wind attack angles from 0° to 90° .

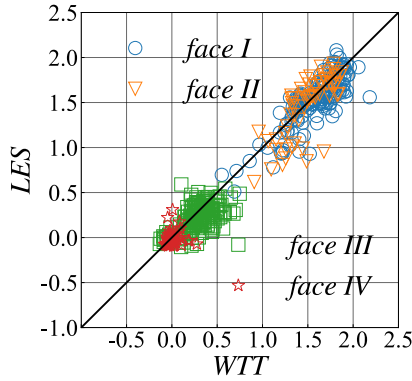
	\bar{C}_p			C'_p			\hat{C}_p			\check{C}_p		
	ME	SE	R^2	ME	SE	R^2	ME	SE	R^2	ME	SE	R^2
0°	-	0.08	0.98	0.00	0.03	0.72	0.00	0.15	0.96	-0.14	0.40	0.75
15°	-	0.05	0.99	-0.02	0.03	0.65	-0.01	0.14	0.96	0.15	0.41	0.85
30°	-	0.06	0.99	-0.02	0.03	0.86	-0.07	0.14	0.95	0.06	0.18	0.93
45°	-	0.02	0.99	-0.03	0.02	0.60	-0.04	0.12	0.96	0.16	0.28	0.68
60°	-	0.04	0.99	-0.01	0.03	0.67	0.00	0.11	0.95	0.10	0.29	0.72
75°	-	0.05	0.98	-0.03	0.03	0.76	-0.08	0.18	0.86	0.12	0.33	0.75
90°	-	0.06	0.98	-0.01	0.03	0.89	-0.06	0.15	0.88	0.11	0.42	0.76
mean	-	0.05	0.99	-0.02	0.03	0.74	-0.04	0.15	0.93	0.09	0.33	0.78

Looking at Tab. 2.2, an overall correspondence in terms of \bar{C}_p is obtained between WTT and LES, with the average R^2 around 0.99. Similarly, good agreements could also be found regarding the \hat{C}_p , whose average R^2 is 0.93.

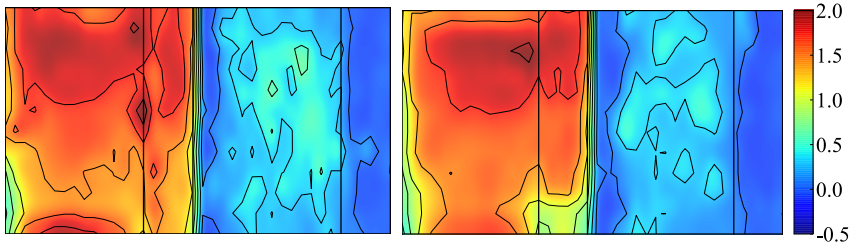
Considering all the wind attack angles, we observe that no clear trend emerges for the error metrics when the angle is varied. For instance, R^2 of C'_p for 0° is 0.72, lower than some skew angles such as 0.86 of 30° and 0.76 of 75° . However, at 90° we obtain the highest value of R^2 among all the cases, equal to 0.89. Substantially, a good matching is obtained when the flow is orthogonal to the short side, leading to a reattached flow. In other conditions results do not follow simple trends. The prediction of fully detached flow expected at 0° is accurate but it is not more accurate than other skew angles.

Figures 2.6 and 2.7 show the local peak values of C_p considering at the same time wind incident angles from 0° to 90° , i.e. the extremes from all attack angles are enveloped together, as for design purposes. In particular, we show scatter plots reporting in abscissa WTT results and in ordinates LES results. In order to allow to individuate taps belonging to different building faces, pressure taps grouped as *face I*, *face II*, *face III* and *face IV*, following the indication in Fig. 2.1 (a). The results in terms of the peak \hat{C}_p appear to be characterized by much higher accuracy with respect to suctions. The extreme negative pressures near the building edges on *face II*, *face III* and *face IV* reach values of -4.0 in WTT but only attain -3.5 in LES. Conversely, LES overestimates the negative extremes near the center bottom of *face IV* where the

\check{C}_p arrives at -5.0 in LES but reaches only -3.5 in WTT.



(a)



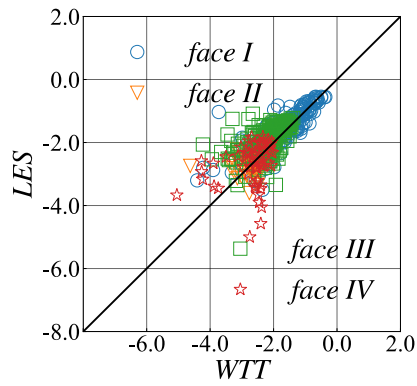
(b)

(c)

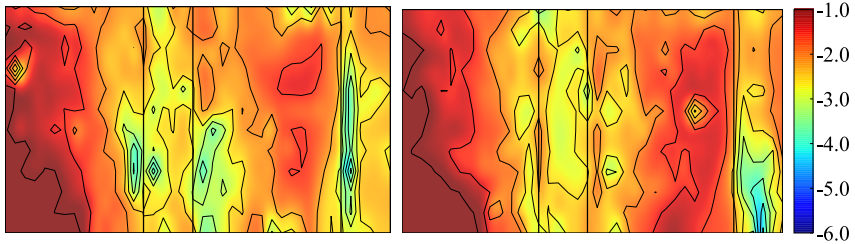
Fig. 2.6. The peak values of \hat{C}_p from all the degrees: (a) scatter plots, (b) surface distribution of WTT and (c) surface distribution of LES.

2.3.3 Global forces and moments

The global forces for all simulated wind attack angles are reported in dimensionless form C_{Fx} , C_{Fy} , C_{Mx} and C_{My} , representing the force and moment components in along-wind (x) and cross-wind (y) directions, as shown in Figs. 2.8 and 2.9. Specifically, the time series of C_p are integrated over the building surface to obtain the non-dimensional force coefficients time histories. Then, for each incidence angle, the peak values (including the maximum and minimum) of forces and moments are calculated following the same procedure



(a)



(b)

(c)

Fig. 2.7. The peak values of \check{C}_p from all the degrees: (a) scatter plots, (b) surface distribution of WTT and (c) surface distribution of LES.

used for the pressure peaks explained in Sec. 2.3.1. Again, for design purposes, the peaks from all the angles are enveloped and indicated as *LES env.* and *WTT env.* in the figures.

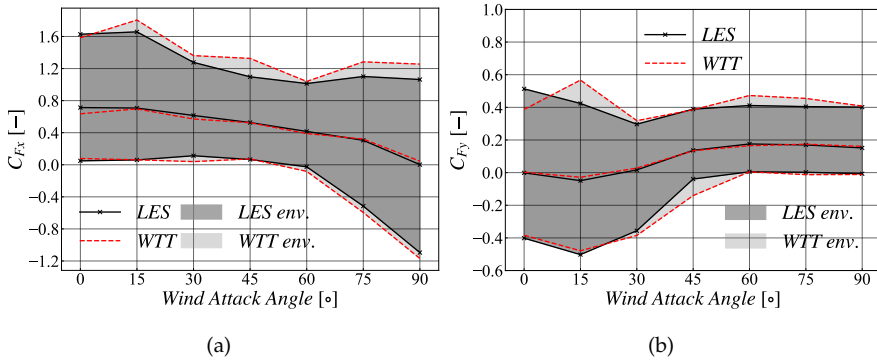


Fig. 2.8. The global forces coefficients of all the simulated wind attack angles: (a) C_{Fx} and (b) C_{Fy} .

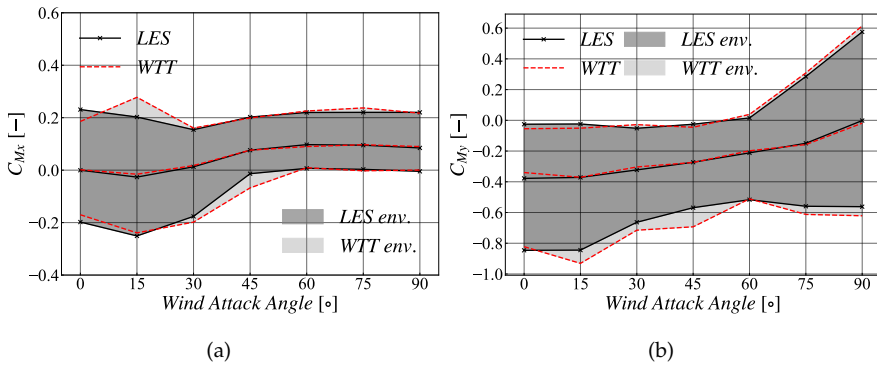


Fig. 2.9. The moments coefficients of all the simulated wind attack angles: (a) C_{Mx} and (b) C_{My} .

It can be seen that the LES reproduces the global forces and moments very well with only a slight underestimation in terms of the maximum values of positive C_{Fx} and C_{Fy} . The strongest deviation is on 15° , where the extreme values of both forces and moments in LES are about 25% lower than in WTT. Again, discrepancies can be found for 45° , for which the peak values of forces (and moments) have smaller values in LES than in WTT. Similar results are also found in [116] which declared that the wind attack angle of 15° approaches

the critical angle or glancing angle and has the minimum drag force coefficient and maximum mean lift magnitude, and the Strouhal number (St) is maximized.

2.3.4 Prediction errors for 45° case

As the 45° case appears to be the one presenting higher discrepancies between WTT and LES, we further investigate it in this section in more detail. Hereafter the Prediction Error (PE) is used as an error metric and is defined as $PE_S = LES_S - WTT_S$, where the subscript S represents the C_p statistics, i.e., \bar{C}_p , C'_p , \hat{C}_p and \check{C}_p .

Figure 2.10 presents the scatter plots of C'_p and \check{C}_p for the 45° case. The scatter plots of \bar{C}_p and \hat{C}_p are not reported here, since they are satisfactory accurate. It can be seen that C'_p on *face II* shows systemic underestimations from the numerical model. In fact, monitors with C'_p approaching 0.5 in WTT are lower than 0.3 in LES. As expected, underestimations also regarding \check{C}_p can be found on these probes, with the negative extremes in LES are 60% less pronounced than in WTT. Besides, some localized differences regarding \check{C}_p can be found on *face III*. The values of \check{C}_p of these points are around -3.0 in WTT but are lower than -2.0 in LES.

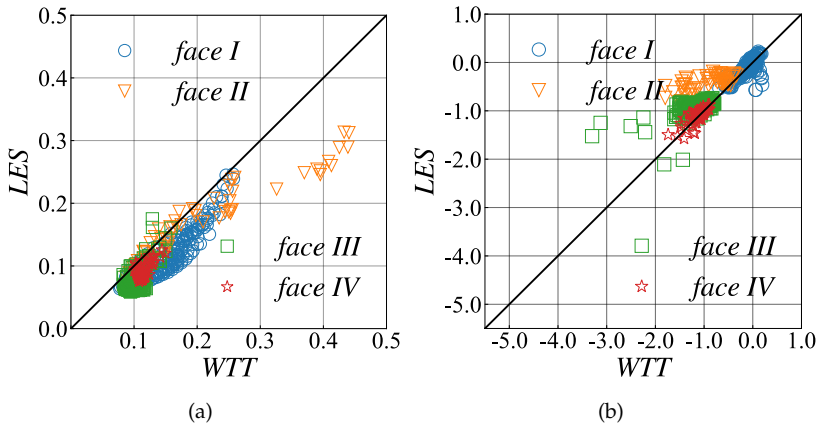


Fig. 2.10. Scatter plots of C'_p (a) and \check{C}_p (b) for 45° case.

Figure 2.11 and 2.12 present the surface distributions of C'_p and \check{C}_p as well as their prediction errors, i.e., $PE_{C'_p}$ and $PE_{\check{C}_p}$. More specifically, it can be clearly seen that the underestimations mentioned above are located near the leading edge of *face II*. Looking at Fig. 2.11 (a) and (b), the higher values of C'_p are also located on this region.

As for the independent spots near the top edge of *face III* where the highest $PE_{\check{C}_p}$ appears, one possible explanation can be found in a relative study [105]: the extreme value is recorded downstream the leading edge, from which strong vortices are expected to be shed.

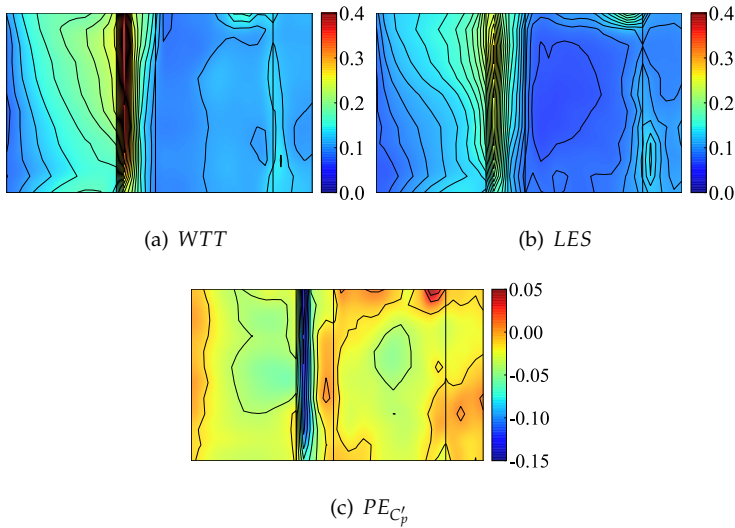


Fig. 2.11. The surface distributions of the C'_p and the $PE_{C'_p}$ for 45° case.

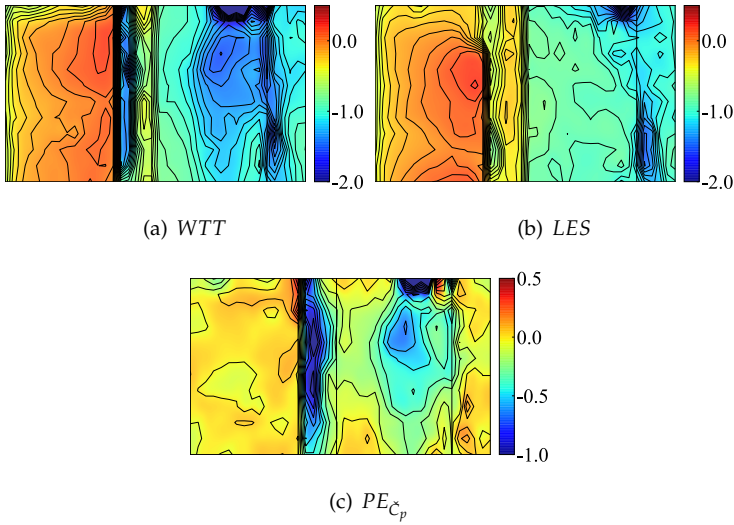


Fig. 2.12. The surface distributions of the \check{C}_p and the $PE_{\check{C}_p}$ for 45° case.

Figure 2.13 presents the frequency distributions of $PE_{C'_p}$ and $PE_{\check{C}_p}$. It can be seen that the $PE_{C'_p}$ concentrates around -0.05. It can also be found that deviations between LES and WTT in terms of extreme suction ($PE_{\check{C}_p}$) are mainly inside the range -1.0 and 0.0, which indicates a tendency of the simulation to underestimate such quantity and provides a measure of the expected underestimations.

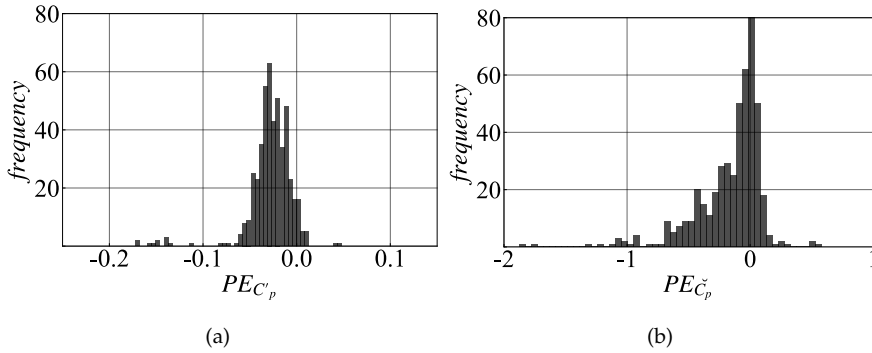


Fig. 2.13. The frequency distributions of PE_{C_p} (a) and $PE_{\check{C}_p}$ (b) for 45° case.

2.4 Sensitivity study

In this section, the influence of parameters including mesh setting and LES subgrid scale (SGS) model on numerical results for the 45° case is investigated, attempting to ameliorate the previously obtained prediction errors.

2.4.1 Mesh

We firstly consider the possibility to ameliorate results by refining the mesh. In Section 2.3, we observed that the selected meshing parameters were able to guarantee a low sensitivity of the obtained results to the cell size. Nevertheless, the study was performed at 0° , so that it cannot be automatically extended to 45° .

We here consider two mesh refinement strategies: in the first one we refine all the fluid volume around the building while in the second one we add boundary layer cells. Then, the two strategies are combined.

Consequently, three adjusted meshes based on MM are obtained. The details of the tested meshes are listed below: (I) boundary layer cells, which have 8 layers and the minimum thickness equaling 0.0004 m and scratching ratio of 1.15, are added to the building surfaces leading to the mesh named BL; (II) the mesh size is refined to 0.004 m up to a distance of 0.2 m from the

2.4. Sensitivity study

building and to 0.002 m to a distance of 0.025 m from the building, resulting in the mesh named BR; (III) the two aforementioned strategies are applied at the same time, yielding the mesh named BL_BR. The mesh zones far away from the building are kept unchanged. An overview of the newly considered meshes in the proximity of the building is provided in Fig. 2.14 and their characteristics are provided in Tab. 2.3. It is worth noting that the addition of boundary layer cells dramatically increases (double) the computational costs, though a relatively lower (half) value of y^+ can be obtained at the building surfaces.

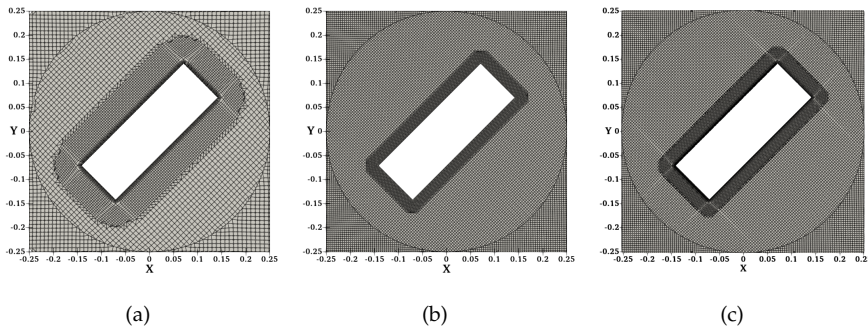


Fig. 2.14. The configurations of the mesh near the building: (a) BL, (b) BR and (c) BL_BR.

Table 2.3: Information of all the tested meshes, for wind attack angle equal to 45° .

	cells number (million)	cells number for each building side			Δt (-)	computational time (CPU - hour)	y^+
		H	L	W			
BL	2.1	166	100	33	0.005	563	10.0
BR	6.0	250	150	50	0.003	1670	24.0
BL_BR	7.0	250	150	50	0.001	3600	10.0

The error metrics of the three cases are presented in Tab. 2.4. Unexpectedly, the mesh with boundary layer cells, i.e., BL, has worse performance in terms of C_p' prediction compared to the original mesh, MM. Specifically, the R^2 of C_p' for mesh MM is 0.60 while for the mesh BL decreases to 0.54. Differently, the BR mesh shows better performance in terms of C_p' , reaching R^2 equal to 0.65.

As it can be seen, despite such variations, the overall error does not change substantially, especially if we consider the high increase in computational resources needed to make the refinements. We also show that the combination of the two refinement strategies BL_BR does not show a more accurate prediction of C'_p .

Now we see the simulated results in terms of \check{C}_p . Again, slightly better performance can be found from BR than from BL, while the results from BR and BL_BR are close to each other.

Table 2.4: Error metrics of \bar{C}_p , C'_p , \hat{C}_p and \check{C}_p for LES with different mesh distributions.

	\bar{C}_p			C'_p			\hat{C}_p			\check{C}_p		
	ME	SE	R ²	ME	SE	R ²	ME	SE	R ²	ME	SE	R ²
BL	-	0.02	0.99	-0.03	0.02	0.54	-0.06	0.11	0.96	0.16	0.27	0.71
BR	-	0.02	0.99	-0.03	0.02	0.65	-0.04	0.12	0.96	0.14	0.25	0.76
BL_BR	-	0.02	0.99	-0.03	0.02	0.63	-0.04	0.13	0.96	0.08	0.26	0.77

Figures 2.15 and 2.16 show the surface distributions of the prediction errors $PE_{C'_p}$ and $PE_{\check{C}_p}$ for the three meshes. The range of $PE_{C'_p}$ for BL is close to the original simulation, MM, still showing high error values on *face II*, which seems to indicate a detachment of the flow at the edge for WTT not predicted by LES. This can be deduced also by Fig. 2.11 (a) and (b) in which C'_p is shown. The distribution of $PE_{\check{C}_p}$ for all the analysed meshes is shown in Fig. 2.16, which does not show any major difference between the three.

2.4. Sensitivity study

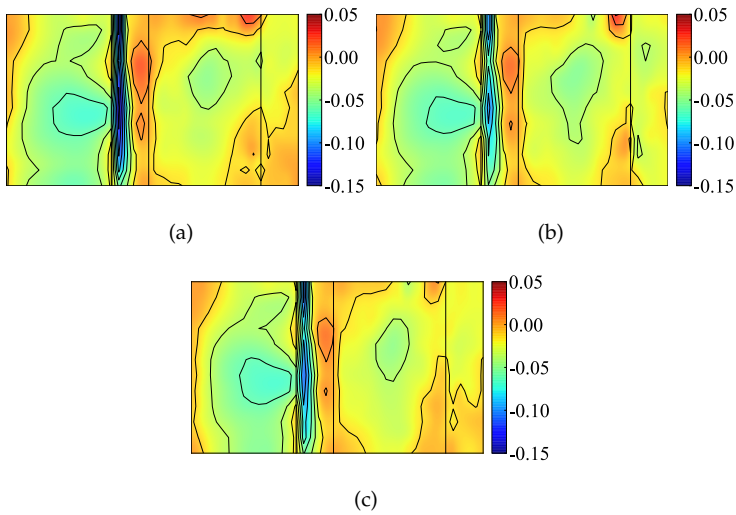


Fig. 2.15. The surface distributions of the PE_{C_p} of different mesh resolutions: (a) BL, (b) BR and (c) BL_BR.

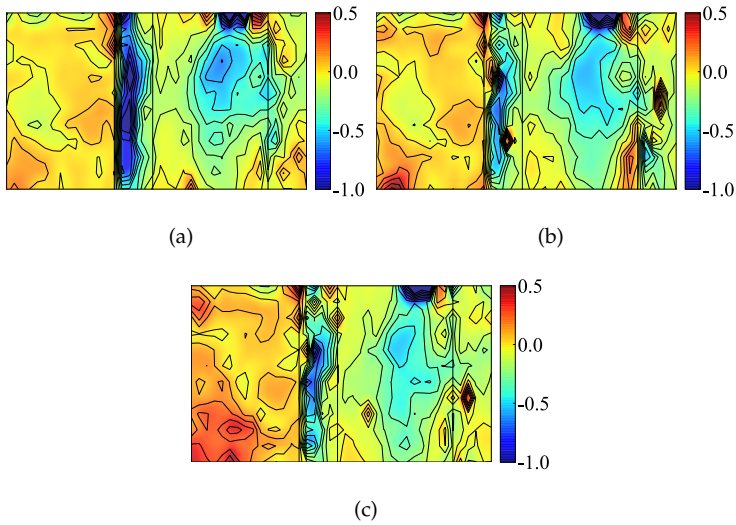


Fig. 2.16. The surface distributions of the PE_{ζ_p} of different mesh distributions: (a) BL, (b) BR and (c) BL_BR.

2.4.2 Subgrid scale model

It has been seen that refining the mesh did not yield strong improvements of the results, despite its high increase of computational costs. We thus here investigate the effect of changing the turbulence model. Table 2.5 reports error metrics of C_p statistics for simulations on mesh MM with different turbulence models (namely, WALE, $k - \omega$ SSTAS and Smagorinsky). Overall, none of them shows better model performance than the original turbulence model, i.e., k-Equation, whose ME for C'_p and \check{C}_p are -0.03 and 0.16, respectively. Only marginal improvements can be seen, for instance, regarding R^2 for \check{C}_p , with the value increasing from 0.68 in the original simulation to 0.71 in the simulation with the Smagorinsky model.

Table 2.5: Error metrics of \bar{C}_p , C'_p , \hat{C}_p and \check{C}_p for different turbulence models.

	\bar{C}_p			C'_p			\hat{C}_p			\check{C}_p		
	ME	SE	R^2	ME	SE	R^2	ME	SE	R^2	ME	SE	R^2
<i>WALE</i>	-	0.02	0.99	-0.03	0.02	0.56	-0.04	0.12	0.96	0.16	0.27	0.70
<i>k - ω SSTAS</i>	-	0.03	0.99	-0.04	0.02	0.38	-0.11	0.12	0.94	0.24	0.26	0.63
<i>Smagorinsky</i>	-	0.02	0.99	-0.03	0.02	0.58	-0.05	0.12	0.96	0.17	0.26	0.71

From the distributions of $PE_{C'_p}$ (Fig. 2.17) and $PE_{\check{C}_p}$ (Fig. 2.18), the differences between the three cases are also insignificant. In a summary, the prediction errors of C'_p and \check{C}_p for 45° are not sensitive to changes in the adopted turbulence model.

2.4. Sensitivity study

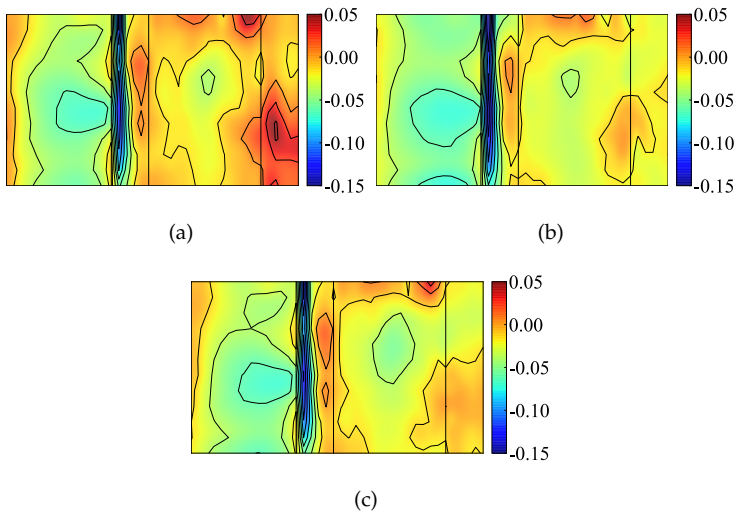


Fig. 2.17. The surface distributions of the PE_{C_p} of different turbulence models: (a) WALE , (b) $k - \omega$ SST SAS and (c) Smagorinsky.

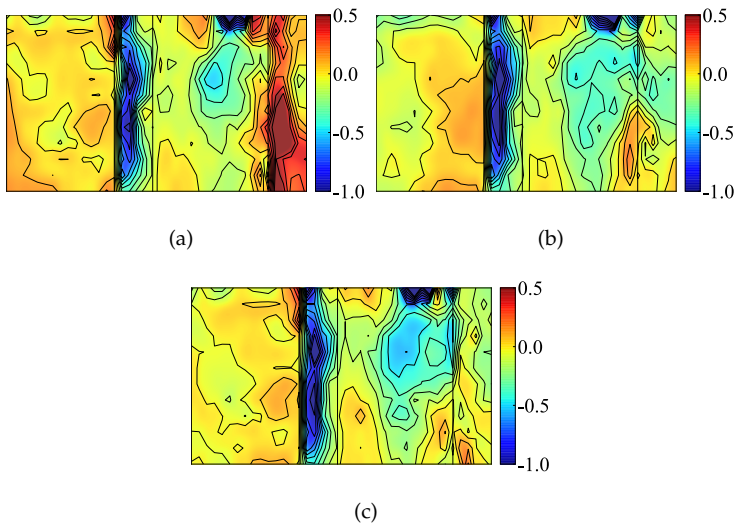


Fig. 2.18. The surface distributions of the PE_{z_p} of different turbulence models: (a) WALE, (b) $k - \omega$ SST SAS and (c) Smagorinsky.

2.5 Conclusion

Wind fields around an isolated high-rise building model with an aspect ratio of 1:3:5 are simulated using LES to evaluate the model performance and investigate the influences of several model parameters on the prediction errors. Simulations are performed for seven wind attack angles ranging from 0° to 90° with an increment of 15° . The main conclusions of the study are hereby drawn as below:

1. Globally, LES is capable of capturing the mean and maximum wind pressure on the building for both perpendicular and skew wind attack angles, with the correlation (R^2) between the experimental and predicted results being 0.99 for \bar{C}_p and 0.93 for \hat{C}_p on average. The model performance on the prediction of global forces (moments) is also extremely satisfactory, showing very good agreement with WTT results. However, the numerical accuracy in terms of C'_p and \check{C}_p is less satisfactory, especially in a few cases. The R^2 for C'_p and \check{C}_p are 0.74 and 0.78 on average, respectively;
2. For the considered cases, the worst predictions are obtained with an attack angle of 45° . The high values of $PE_{C'_p}$ and $PE_{\check{C}_p}$ for this case concentrate on the leading edge in correspondence of the flow separations. It appears that a flow separation occurs in WTT which is not predicted by the adopted numerical models;
3. The prediction errors of C'_p and \check{C}_p for 45° are not sensitive to the addition of boundary layer cells for the near-wall treatment. Some marginal improvements are obtained by refining the mesh in the surroundings of the building, but this will dramatically increase the computational time;
4. No major improvement is obtained by changing the adopted turbulence model.

Overall, it is difficult to individuate with certainty the cause of the observed discrepancies. Actually, many possible causes can be individuated. Such causes range from small deviations of the geometry with respect to WTT to

2.5. Conclusion

differences in the incoming turbulence, despite the fact that a good matching was obtained in terms of turbulence intensity, and length scales were prescribed according to usual practice. Surely, we observe that the considered case is not particularly sensitive to the adopted turbulence model and mesh size, once an appropriate mesh has been initially selected. It must be remarked, that the addition of boundary layers proved, beside not ameliorating results, had only a very limited effect on the obtained results.

3 Wind loads prediction using LES: Inflow generation, accuracy and cost assessment for the case of Torre Gioia 22

In this paper, Large Eddy Simulations, LES, are used in order to evaluate wind loads on a recently designed high-rise building located in Milan, Italy. The selected case study is taken as an example of a typical wind loading assessment, characterized by a complex geometry due to both the shape of the tower and the presence of surroundings. Firstly, the sensitivity of the results to the adopted mesh is analysed. Then, results are compared to wind tunnel measurements and the economical viability of such kind of simulations is discussed. The paper aims at providing an overview of the main factors which can contribute to the success of such analyses and evaluate their accuracy. Not specialized readers will hopefully gain a better insight into the critical aspects which characterize such simulations, while the interested readers will find numerous practical considerations useful for their setup.

3.1 Introduction

The use of Computational Wind Engineering, CWE, for the simulation of the wind flow over complex terrains and building arrangements has greatly evolved in the last thirty years, transitioning from early investigations in the research

field to widely adopted applications in the design industry [117, 118]. Nowadays, CWE is widely used as an alternative to traditional wind tunnel experiments for applications such as indoor [119] and pedestrian level wind comfort [120] as well as pollutant dispersion [121] and predictions of the flow field in urban areas [122].

With respect to such kind of applications, the evaluation of wind loads on structures by means of CWE is lagging at least a decade behind: while numerous papers have been presented in the scientific literature [104, 123, 124] demonstrating the suitability of numerical models for such evaluations, their use in practice is still limited and somehow controversial, also due to the heavy legal responsibilities which follow the wind load assessment.

The controversy is fostered by three main aspects. The first one is that wind tunnel tests are built aiming at evaluating at the same time global effects for the design of the main structural systems and cladding loads, usually greatly influenced by local flow mechanisms [31, 125]. It is well-known that the predictive capability of numerical models can be extremely different when targeting such two aspects.

The second one is that numerical models sometimes show a remarkable sensitivity to parameters which might be difficult to be chosen a priori. Such aspect is deeply related to the strong sensitivity to inflow conditions, Reynolds number and geometrical details shown by some cases also in wind tunnel tests: the circular cylinder is only the most well-known member of this infamous family [126, 127]. From this point of view, it might be correctly stated that wind tunnel tests have the inherent advantage with respect to Computational Fluid Dynamics, CFD, simulations to introduce uncontrolled perturbations which are qualitatively more similar to the conditions actually experienced by real flows than the fictitious perfection of numerical models.

The third aspect is actually the most important one and it is inherently intertwined with the two aforementioned points. While it has been repetitively shown that well-resolved scale resolving models can be potentially used for the evaluation of wind loads, for cases characterized by real complexity their

3.1. Introduction

cost is still very high, making them only partially competitive with wind tunnel tests. On such regard, it should be added that mesh independence assessments, a cornerstone of numerical simulation, have been often used in the literature in an instrumental way, aiming at producing a measurable proof of the adequacy of the adopted model rather than a methodologically rigorous assessment of the solution quality [128].

In this paper, we present the results of a collaboration between RWDI and University of Bologna for the estimation of wind loads for a newly designed tower denoted Porta Gioia 22, located in Milan, Italy. The study is aimed at assessing the viability of numerical simulations for the assessment of wind loads in cases characterized by real complexity and taking into consideration computational time/costs constraints. Key aspects of the analyses such as inflow generation and its application to the computational domain are performed with techniques developed by the authors in recent years. Such techniques are here briefly discussed aiming at describing their rationale and highlighting their relations with others methods available in the literature. The analyses are performed aiming at comparing wind tunnel results and numerical simulations in terms of quantities useful for the structural design. We highlight that other similar contributions have been already presented in the literature, usually privileging simple geometries such as the CAARC model, for the sake of reproducibility [95, 129]. In this case we take a different perspective and consider a building characterized by numerous geometrical details [130, 131] taking also into account the reconstruction of the building surroundings. Other contributions with similar characteristics can be found for instance in [124, 132, 133]. Such choice leads only to minor, although fundamental, practical differences with respect to cases characterized by simple geometries, but it leads to completely different choices in the setup of the analyses and in the management of the resources, and thus, on conclusions related to their viability and economical convenience.

The paper is organized as follows: in Sections 3.2 and 3.3 the considered case is described and wind tunnel tests used for reference are briefly detailed. The setup used for the numerical simulations is presented in Section 3.4. Results of the proposed analyses are shown and compared to experimental values in

Section 3.5, where also computational costs are analysed. Finally, conclusions are drawn in Section 3.6.

3.2 Case description

The selected case study is part of a vast urban development plan denominated Porta Nuova Gioia, undertaken to modernize an area located in the immediate surroundings of the city centre of Milan. Within the numerous newly constructed buildings, we selected the tower referred to as Torre Gioia 22, designed by César Pelli and under construction at the time of writing.

The tower stands at a height of 120 m, made up of 30 storeys and sits on a three storeys podium. The building is characterized by sharp edges and smooth glass facades, which in some areas are adorned by horizontal decorative elements running along the building corners. The top of the tower is characterized by a crown protected by a 10 m high wall, built on the roof. The building is located in a densely urbanized area, with the presence of other high rise buildings which are already present or planned.

3.3 Wind tunnel tests

Wind tunnel tests have been performed by RWDI in the boundary layer wind tunnel located in Milton Keynes (UK). The wind tunnel section is 2.4 m wide and 2.1 m high and presents an open chamber testing configuration. The model has been 3D printed at a scale equal to 1:300, so that the scaled building height is 0.4 m. An overview of the wind tunnel setup is shown in Fig. 3.1 (a). The surroundings of the tower have been modelled in detail within a radius of 360 m (full scale) from the tower, while the main buildings have been reproduced up to a distance of approximately 600 m.

Actually, two configurations of the surroundings have been tested: the first one, denoted as C1, is relative to the current condition, while the second one, denoted as C2, takes into account the presence of two currently non-existing

3.4. Numerical model

buildings already planned in the area. In the following, only C1 will be considered and reproduced by means of numerical simulations.

The approaching flow has been designed in order to reproduce an Eurocode Category III terrain. The reference height H_r is taken as the building height, H , and the reference velocity there measured in empty wind tunnel conditions is equal to $U_r = 35.8$ m/s.

The wind tunnel model is equipped with 504 pressure taps acquired synchronously at 512 Hz (see Fig. 3.1 (b)). For each configuration (i.e. C1 and C2), the incidence angle is varied with increments of 10° and pressures are recorded for 35 s. Before postprocessing, a low-pass filter with cut-off at 128 Hz has been applied.

Assuming a design wind speed equal to 30 m/s at the tower height, the acquired time-series correspond to approximately 210 *min* in real scale, so leading to 21 10-*min* samples.

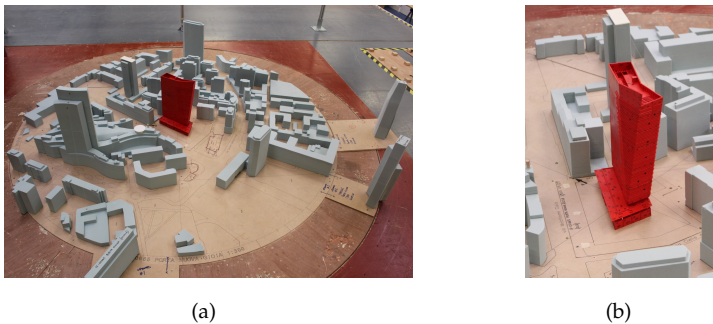


Fig. 3.1. Overview of the setup used for wind tunnel tests: (a) surroundings and (b) detail of the tower.

3.4 Numerical model

In the following, the numerical model used to perform the analyses is described. The components and modelling choices which contribute the most to the effectiveness of the simulation and/or to the quality of the obtained

results are discussed in detail. Indeed, as it will be later further discussed, some choices operated in the model setup are known to be sub-optimal and are dictated by the need to ensure the robustness of the simulations and their actual viability (in terms of stability and computational requirements) in complex cases. Simulations have been performed with OpenFoam v6 using the infrastructures of CINECA (Consorzio Interuniversitario dell'Italia Nord Est per il Calcolo Automatico), Italy.

3.4.1 Computational domain

An overview of the computational model, realized at the same scale used for wind tunnel tests, is provided in Fig. 3.2. The computational domain measures 5.0 m, 3.5 m, and 2.1 m in length, width and height, respectively. The distance from the inlet patch to the tower is 2 m.

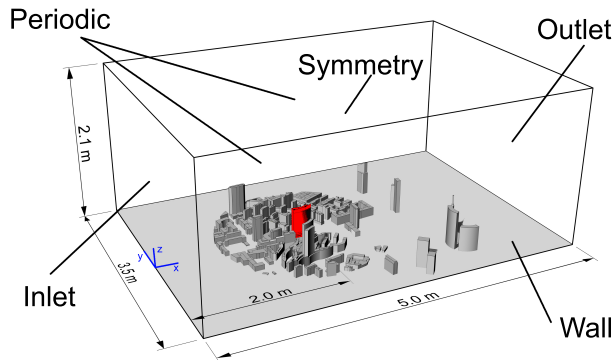


Fig. 3.2. Overview of the computational domain and the adopted boundary conditions.

Actually, in order to facilitate the meshing operations, in analogy with wind tunnel procedures, a rotor-stator approach is adopted. In particular, the computational domain is subdivided into two zones: a cylinder of radius 1.3 m with axis oriented along the z-direction passing through the tower centre (denoted as rotor in the following) and all the rest of the domain (denoted as

3.4. Numerical model

stator in the following). The two parts are connected by a non-conformal interface. A view of the rotor geometry is provided in Fig. 3.3 (a) while a detailed view of the tower is provided in Fig. 3.3 (b). The geometry of the tower has been rebuilt starting from that exported from the architectural model but defeaturing has been limited to extremely small details and mainly used to eliminate unnecessary edges between surfaces partitions, which strongly jeopardize the results of the meshing operations.

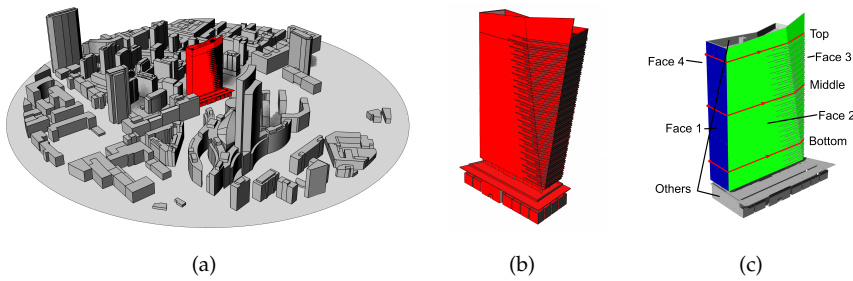


Fig. 3.3. Detailed views of the studied geometry: (a) rotor, (b) tower and (c) paths and faces adopted to present results.

When studying the wind effect at different angles of attack the rotor part is rigidly rotated while the stator part is re-meshed, because it includes some of the buildings. Considering that the meshing operations are particularly delicate and time-consuming exclusively for the rotor, the approach maintains its convenience despite the fact that the stator must be re-meshed for some angles. On such regard, it should be noticed that enlarging the rotor to avoid such problem is not advisable, as it leads to a large number of cells. This is due to the fact that the rotor must be meshed in a uniform manner, without taking advantage of the wind directionality. Finally, it should be noticed that meshing has been here performed using SnappyHexMesh, the standard meshing tool included in OpenFoam which uses a top-down approach. When using such tool it should be bear in mind that the quality of the obtained mesh is sensibly affected by the orientation of the geometry with respect to the starting mesh. It is thus advisable to mesh the rotor part aligning the building

geometry with the reference system whenever possible, especially when relatively coarse meshes are adopted.

3.4.2 Mesh

An overview of the mesh is provided in Fig. 3.4 (a) while a detail view of the tower is provided in Fig. 3.4 (b). The volume inside the rotor is meshed with a size approximately equal to $0.04H$ (5 m in full scale). The buildings composing the surroundings are meshed with a typical size equal to $0.02H$ (2.5 m in full scale) and this size is adopted up to a distance from their surface equal to $0.125H$. The surrounding buildings edges are meshed with a typical size equal to $0.01H$ (1.25 m in full scale), the same used for the tower surfaces and for the volume close to the tower up to a distance equal to $0.25H$. The tower edges, the decorative details projecting from the facades and the crown of the tower are meshed with a typical size equal to $0.005H$ (0.62 m in full scale). An expansion ratio is adopted in the vertical mesh spacing in order to obtain a coarser mesh moving away from the ground. The adopted expansion ratio is such that cells at the top of the domain are three times larger than those at the ground.

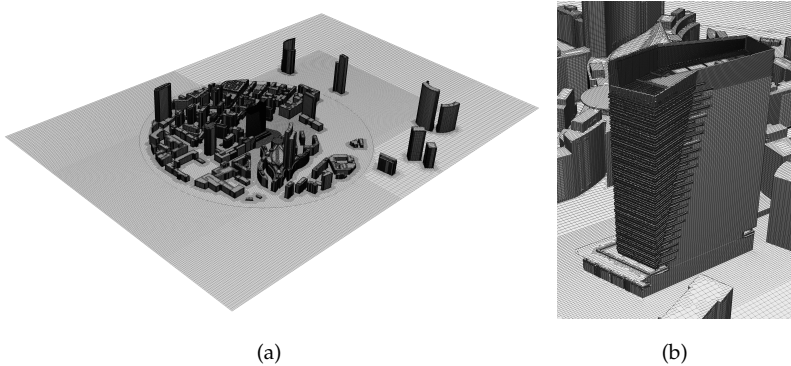


Fig. 3.4. The adopted mesh: (a) overall and (b) detail of the tower.

As it can be seen from Fig. 3.4 (b) some details of the tower cannot be meshed with a good resolution using such mesh sizes. Although an overall good result

is obtained, some of the edges could not be meshed accurately. This is particularly true for small details and thin walls located on the crown. The effects of such geometrical inaccuracies can be dramatic in smooth flow conditions but might be moderate in strongly turbulent flows and must be evaluated based on the obtained results.

The stator is meshed with the same sizing used for the rotor in the zone extending from the ground up to a height equal to $2.5H$ in the zone upstream the rotor. The same sizing is also used in the zone downstream the rotor, up to a distance equal to $5H$ from the tower. The other parts are meshed with the coarser adopted mesh level, characterized by size in the xy -plane equal to $0.08H$. A refinement has been adopted also at the rotor-stator interface to reduce the errors introduced by the non-conformal interface. Overall, the maximum non-orthogonality is equal to 70° and it is concentrated in an extremely limited number of cells. Analogously the maximum skewness is equal to 5.

The mesh obtained by adopting such sizings counts in total 9.5 M cells. We notice that we did not introduce boundary layers to perform the simulations. The normalized wall distance y^+ around the tower surface is 10 on average and the maximum value is around 100. Indeed, their introduction would strongly increase the cell count and, willing to keep fix the total number of cells, would require to coarsen the mesh in the building surroundings. On such regard, it is noticed that in the literature there is a consolidated tendency to consider y^+ a fundamental parameters to judge mesh quality. In fact, this is well-justified for streamlined bodies, especially when immersed in smooth flows (and in fact its importance is well-justified for aeronautical applications). However, it is indeed unclear why such parameter should be considered of paramount importance for bluff-bodies with sharp corners immersed in turbulent flows. The overall result is that, in order to obtain a low y^+ , most of the time the mesh is rapidly coarsened in the zones occupied by detached shear layers, which are actually among the most important flow features for bluff body aerodynamics [134]. We also notice that the presence of perfectly sharp edges have been found to be problematic from the numerical point of view leading to paradoxical results [127], which might be worsened by mesh refinement at edges and corners.

In a summary, the 9.5 M cells are subdivided so that approximately 7 M are in the rotor and approximately 2 M are in the immediate surroundings of the tower.

3.4.3 Models and numerical schemes

The standard $k - \epsilon$ equation LES model [135] is adopted in order to model sub-grid stresses together with Van Driest damping functions at wall-boundaries. Bounded linear schemes are adopted to evaluate fluxes at the cell faces for all quantities apart from velocities, for which the LUST scheme is adopted [136]. Gradients and laplacians are calculated using partially corrected schemes, in which the non-orthogonal part is forced to be smaller than the orthogonal part. Such choices, as it is well-known, sacrifices accuracy favoring numerical stability. PISO is adopted for pressure-velocity coupling. The pressure field is solved using the GAMG solver while a symmetric Gauss-Seidel smoother is used for the velocity field. Tolerances are set to 10^{-5} for all quantities apart from the final pressure for which 10^{-6} is adopted.

The Crank-Nicolson scheme with 10% backward Euler scheme is used for time advancement with a non-dimensional time step $\Delta t \cdot U_r / H = 2.2 \cdot 10^{-3}$ (where U_r is 11.3 m/s and H is the building height), leading to a maximum Courant number equal to 4 only in some particularly small cells and well-below 1 in the immediate building surroundings.

3.4.4 Boundary conditions

An overview of the boundary conditions, BCs, adopted for the current case is provided in Fig. 3.2. In particular, wall conditions are adopted for the tower surfaces, the surroundings and the ground. Periodic conditions are adopted for the sides (a larger domain with respect to the wind tunnel section is used, also considering the open chamber configuration) and symmetry conditions are used for the top. The rotor and the stator are connected using a non-conformal mesh interface and a mixed inlet-outlet condition is adopted at the outflow.

As it can be noticed, the fetches located in front of the tower in the wind tunnel tests have not been reproduced. It is thus mandatory to adopt a turbulent inflow in order to reproduce the incoming Atmospheric Boundary Layer, ABL, profile. In this case, the inflow condition has been specified in agreement with wind tunnel tests as regards the time-averaged wind speed and turbulence intensity for the along wind velocity components. Other quantities have been estimated based on empirical relations found in [137–139]. The unsteady inflow condition has been obtained through the generation of synthetic turbulence according to [83] and as it is further detailed below.

3.4.5 Synthetic turbulence

It is well-known from wind tunnel tests that a correct reproduction of the incoming unsteady velocity field expected on site is of fundamental importance for the evaluation of wind loads [1, 113]. In the present study the surroundings of the tower are explicitly modelled but, also in these circumstances, the incoming ABL should be accurately reproduced, because the explicitly modelled surroundings are relatively small if compared to the distance needed to allow the development of the ABL. Additionally, the large turbulence scales are the ones which contribute the most to the definition of the wind loads, but are also the ones which require longer fetches to be produced. In wind tunnels, the distance needed for their development is usually shortened by adopting spires [95]. Additionally, in CWE computations the introduction of inflow turbulence has the role to destabilize shear layers produced by the surroundings, which are usually only roughly meshed and, thus, are excessively stable with respect to the real ones.

In the last years, the generation of synthetic turbulence to be used as inflow condition for scale resolving simulations and at the interface between hybrid models has been the object of numerous researches [140, 141]. Briefly, available methods can be grouped into the following groups:

- (a) Simulation Assisted inflow generation methods (*SA*, in the following);
- (b) Synthetic Generation without or with partial approximation of the governing equations (*SGwo*);

- (c) Synthetic Generation with approximation of the governing equations (SG).

In the present simulations the incoming flow is generated relying on the PRFG³ method which is of the SG type for homogeneous flows while it becomes of SGwo type for strongly non-homogeneous flows (as most of the available SG methods). We invite the reader to refer to [33] for details and to [83] for its use in the context of ABL generation. Additional details regarding the generation of inflow conditions and an overview of the available methods is provided in Appendix A.1.

Briefly, PRFG³ relies on a complete four-dimensional spectral decomposition of the velocity field in order to ensure the matching of the three target turbulence intensities (one for each velocity component) and a good approximation of the nine targeted integral length scales. The method takes into account the realizability conditions of a divergence-free velocity field and the convection operated by the time-averaged velocity.

Once the synthetic field has been generated, it must be applied to the numerical simulation. Such operation is not trivial as pressure fluctuations often arise. Further details on the application of unsteady inflow conditions can be found in Appendix A.2. In the present work velocity fluctuations are applied at the inflow patch using the Variationally Based Inflow Correction, VBIC, method [34].

Using the aforementioned procedure, the inlet turbulent field is generated targeting an Eurocode Category III profile, indicated as Tar. in Fig. 3.6. The mean velocity and along-wind turbulence intensity follow the Eurocode prescriptions, while I_v and I_w are $0.75 \cdot I_u$ and $0.5 \cdot I_u$, respectively. Consequently, the reference velocity, U_r , is 11.3 m/s at H_r , where the turbulence intensities in the x , y and z directions are approximately 20%, 14% and 10%, and the integral length scales for u , v and w in the along-wind direction are 150 m, 54 m and 30 m in real scale, respectively.

3.5 Results

In the following, results obtained using the previously described computational model are reported. Firstly, the impinging wind profiles are discussed and compared with wind tunnel data in Sec. 3.5.1. Then, in Sec. 3.5.2 the sensitivity of the results with respect to the adopted computational mesh is analyzed. Results obtained by varying the wind angle of attack are reported in Sec. 3.5.3. Assessments regarding design values such as global forces and peak pressures are shown in Sec. 3.5.4 and Sec. 3.5.5. Finally, computational costs are discussed in Sec. 3.5.6. It is remarked that time histories obtained with numerical simulations have been treated with a low-pass filter according to wind tunnel results.

3.5.1 Inflow

A qualitative overview of the obtained velocity field is provided in Fig. 3.5. The vortical structures generated at the inflow can be clearly distinguished in Fig. 3.5 (a). The variation of the eddy size, which increases moving away from the ground, can be also clearly noticed. In Fig. 3.5 (b) the vortical structures produced in the proximity of the tower are detailed.

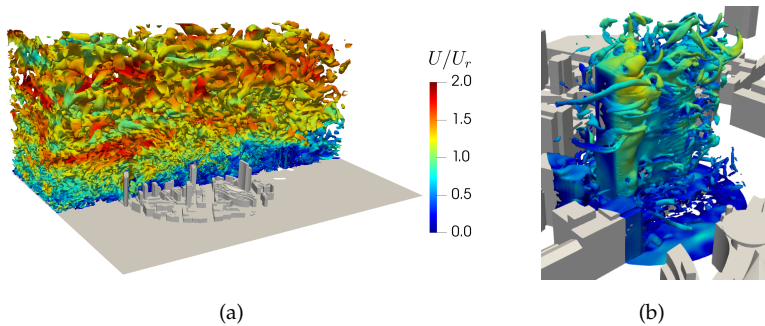


Fig. 3.5. Overview of the velocity field: (a) overview of Q-isosurfaces ($Q(H_r/U_r)^2=0.26$) and (b) detail of vorticity ω -isosurfaces ($(\omega(H_r/U_r)=30)$). Both are colored by instantaneous velocity magnitude. (For interpretation of the references to colour in this figure legend, the reader is referred to the web version of this article.)

For checking the results produced by the inflow generation procedure, an empty computational domain without any obstacle is firstly simulated. A comparison between the velocity and turbulence intensity profiles measured in the wind tunnel, the ones targeted by the synthetic turbulence generation procedure and those actually obtained in the simulation is reported in Fig. 3.6 (a) and (b). In order to characterize the along wind evolution of the velocity field, 12 profiles arranged on a grid located between the inflow patch and the location where the building will be placed (the origin of the reference system) are considered (uniformly spanning the intervals $x \in [-500, 0] m$ and $y \in [-300, 330] m$, full-scale). Then results are represented considering the envelope of such profiles and their mean value. Analogously, the profiles of the along-wind integral length scales for all velocity components is also reported in Fig. 3.6 (c), but in this case comparison is provided with the target value used for L_{ux} , calculated in agreement with [139]. Overall a well-satisfactory agreement between the three can be observed.

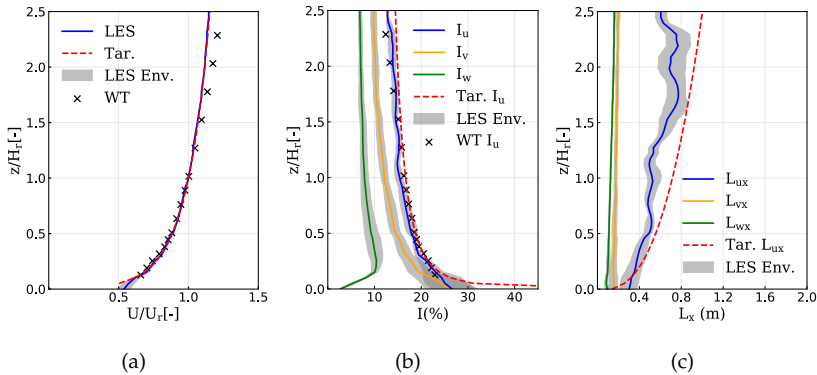


Fig. 3.6. Velocity profile: (a) time-averaged velocity, (b) turbulence intensities, (c) along-wind integral length scales.

The spectra of the three velocity components measured at a distance of 0.5 m from the inflow patch and at the building location at H_r are shown in Fig. 3.7. As it can be observed a good agreement with the target values used in the synthetic turbulence generation procedure has been achieved.

3.5. Results

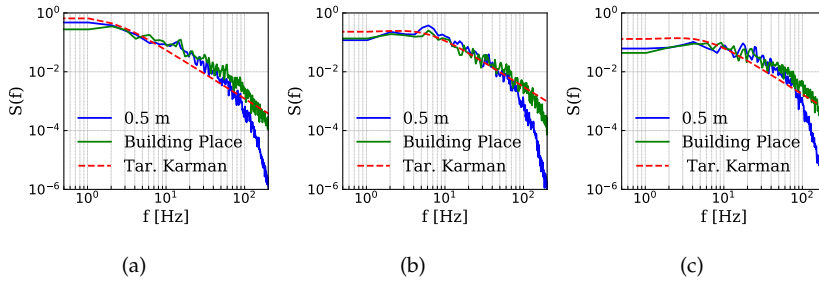


Fig. 3.7. Spectra of the velocity components measured at a distance of 0.5 m from the inflow patch and the building location at the height of H_r : (a) along-wind component, (b) cross-wind component and (c) vertical component.

3.5.2 Mesh sensitivity

In this section, the sensitivity of the results to the mesh sizing is analyzed. As anticipated, in the authors' opinion mesh independence is a vague concept for scale resolving simulations, which must be detailed according to the intended use. We thus proceed, as many others, using it instrumentally in order to assess the effect of the grid on the obtained results. From this point of view it appears more appropriate to speak about mesh sensitivity rather than mesh independence.

In particular, three meshes have been considered. The first one is that described in Sec. 3.4.2 and, in the following, it is denoted as *Mesh M*. As previously reported, it is characterized by approximately 9.5 M cells and mesh sizing equal to $0.01H$ close to the building surfaces and inside the volume up to a distance equal to $0.125H$ from the tower surfaces. Some parts of the tower in which smaller geometrical details are present are meshed with a sizing equal to $0.005H$.

Then, two additional meshes are considered. In particular, a coarse grid, denominated *Mesh C* is also adopted. The mesh is composed of approximately 3.0 M cells. It has been obtained by a global coarsening of the mesh (also in the rotor part) and by considering a typical mesh size close to the tower equal to $0.015H$. When such mesh is adopted, the tower edges and geometry can be

only roughly approximated, especially when a top down approach is used for meshing.

The last considered mesh is denominated *Mesh F* and represents a finer version of *Mesh M*. In particular, the surroundings are meshed using the same settings used for *Mesh M* but all the tower surfaces are meshed with size $0.005H$ and such dimension is used also inside the fluid domain up to a distance equal to $0.25H$. The mesh counts approximately 20 M cells.

Fig. 3.8 reports a scatter plot of the results obtained by using the three aforementioned meshes against experimental measurements at null angle of attack for all the monitored pressure taps. In particular, Fig. 3.8 (a) reports the time-averaged pressure coefficient, \bar{C}_p , while Fig. 3.8 (b) reports the pressure coefficient standard deviation C'_p . It can be seen that all three meshes lead to good predictions of the time-averaged values, so that the scatter plot is mainly located in the proximity of the bisector. A few outliers are present for which all the three meshes lead to the same predictions, suggesting that such values might be influenced by slight discrepancies between the physical and the numerical model. As expected, the main effect of refining the mesh is observed for low pressure zones, located in the proximity of the edges, for which *Mesh F* leads to slightly better results (due to the fact that a fine sizing is used for all the building surfaces). Looking now at C'_p , as expected, a larger scatter is observed, the coarse mesh leads to both under and over-estimations, so that it is difficult to reach final conclusions regarding the adequacy of the three investigated meshes.

We now investigate the dependency of extreme pressure values on the adopted mesh size. In particular, as anticipated, wind tunnel time-histories are representative of 21 samples of duration equal to 10 *min* in real scale. We thus proceed by fitting a Gumbel distribution using the method of moments to such extreme values, so allowing to define the corresponding 90% probability confidence interval. We then plot the extreme values measured in the numerical simulations and compare them with the aforementioned confidence interval. Fig. 3.9 reports for 10-*min* maxima (and minima) the confidence interval obtained using wind tunnel tests for each probe, as well as the 10-*min* extreme

3.5. Results

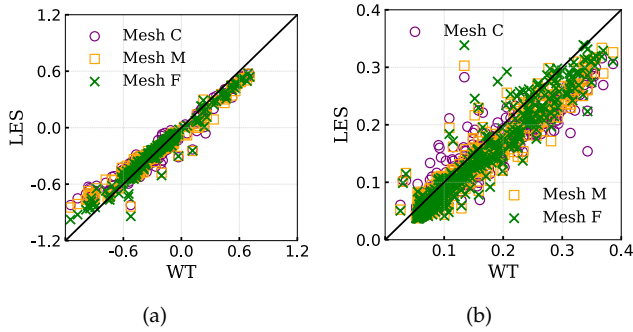


Fig. 3.8. Scatter plot of C_p statistics at 0° angle of attack for the three considered meshes: (a) \bar{C}_p and (b) C'_p .

(a single value) measured in the numerical simulations using *Mesh C*, *Mesh M* and *Mesh F*, respectively. When plotting such results, for the sake of clarity of the representation, the probes have been reordered in ascending (descending for minima) value of the mean 10-*min* extremes extracted from wind tunnel tests.

It can be seen that results obtained in the numerical simulations are in reasonable agreement with experimental values but differences emerge at the most critical probes, characterized by highest suctions. Here *Mesh C* appears to systematically underestimate peak suctions, which do not exceed the value of approximately -1.5, to be compared to the -2.5 measured for *Mesh F*. The situation is summarized in Table 3.1. It can be seen that for *Mesh C* values extracted from the simulations are inside the 90% confidence interval 48.1% and 61.3% of the times for maxima and minima, respectively. Such values are in the range 70%-80% when *Mesh M* and *Mesh F* are adopted, without a monotonic increase of the score with the mesh refinement. Notice that a perfect match would be obtained when the values measured in the numerical simulations are within the confidence interval 90% of the time (also the fact that pressure extreme values do not perfectly respect the Gumbel distribution contributes to lower the obtained score).

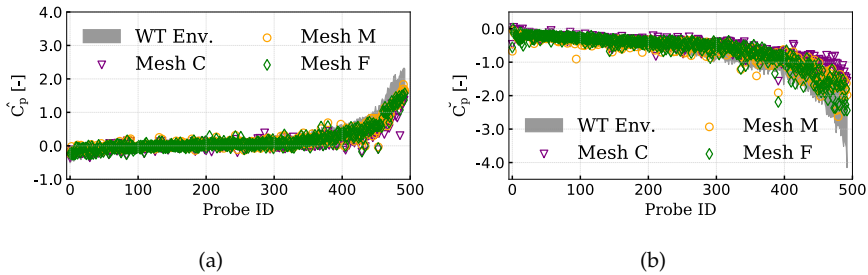


Fig. 3.9. Comparison of peak prediction among three mesh sizes: (a) maxima and (b) minima.

Table 3.1: Sensitivity of the results with the adopted mesh size: extreme values from numerical simulations falling within the 90% probability interval obtained from wind tunnel tests.

	Mesh C	Mesh M	Mesh F
Maxima [%]	48.1	74.8	73.0
Minima [%]	61.3	77.3	71.6

To further investigate the distribution of the 10-*min* extremes, the cumulative density function of the obtained values is reported in Fig. 3.10 and 3.11 (accumulation over all the monitored pressure taps). In particular, for wind tunnel the cumulative density function is calculated base on the extremes which has 50% probability of exceedance while, for numerical simulations, it is calculated based on the single available realization. As expected, for *Mesh C* discrepancies are observed over an extended range of pressure values: for suction a much more rapid decay of the distribution on the negative side with respect to wind tunnel is observed. For *Mesh M* a much better agreement is observed and differences are concentrated in the high suction zones. *Mesh F* leads to a very good agreement also for strong suction. It should be anyway noticed in Fig. 3.9 that, for very strong suction, simulations tend to provide values systematically falling in the higher part of the confidence interval calculated basing on wind tunnel results, in practice leading to results not on the safe side.

3.5. Results

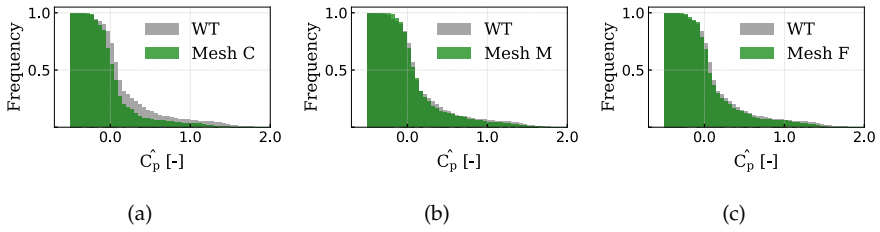


Fig. 3.10. The distribution of \hat{C}_p for different meshes: (a) *Mesh C*, (b) *Mesh M* and (c) *Mesh F*.

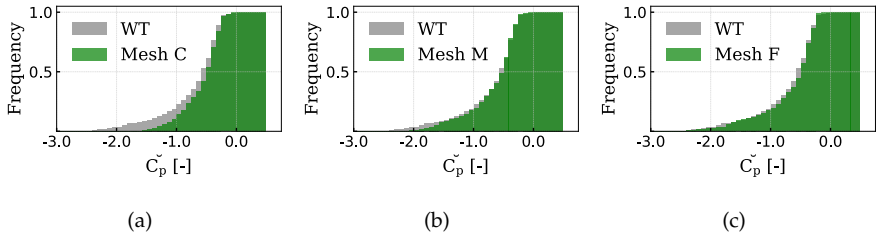


Fig. 3.11. The distribution of \check{C}_p of different meshes: (a) *Mesh C*, (b) *Mesh M* and (c) *Mesh F*.

In conclusion, it appears that *Mesh C* provides sensibly different results with respect to the wind tunnel for many quantities of interest. Some differences are also recorded for *Mesh M* and *Mesh F* for peak values, especially for 10-min extreme suction, but results do not appear to clearly ameliorate with refinements of the zone in the proximity of the tower. In the following only *Mesh M* is considered in order to perform simulations at other angles of attack.

3.5.3 Polar

The instantaneous flow field in the proximity of the tower at 0° , 120° and 240° is qualitatively depicted in Fig. 3.12.

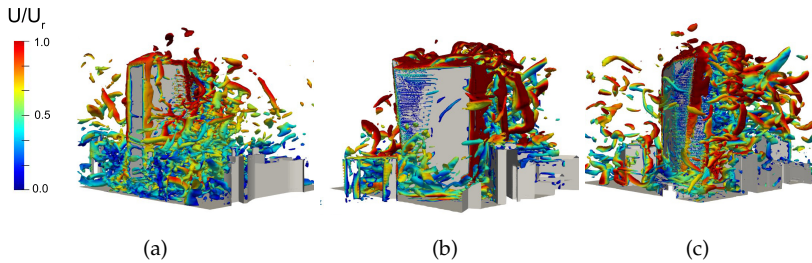


Fig. 3.12. Instantaneous flow field at different attack angles: (a) 0° , (b) 120° and (c) 240° .

Fig. 3.13 reports the distribution of C_p along three paths which go around the building at three heights (see Fig. 3.3(c)) at null attack angle. In particular, the time-averaged value and the standard deviation are considered. The coordinate along the path is indicated as s .

Overall, a good agreement between experimental results and simulations is observed. As expected, at the edges between inclined faces, a sharp change in the pressure field is observed, with the formation of jumps and cusps at the passage between differently oriented faces. Such jumps and the prominence of the cusps, as expected, is slightly underestimated in the simulations.

3.5. Results

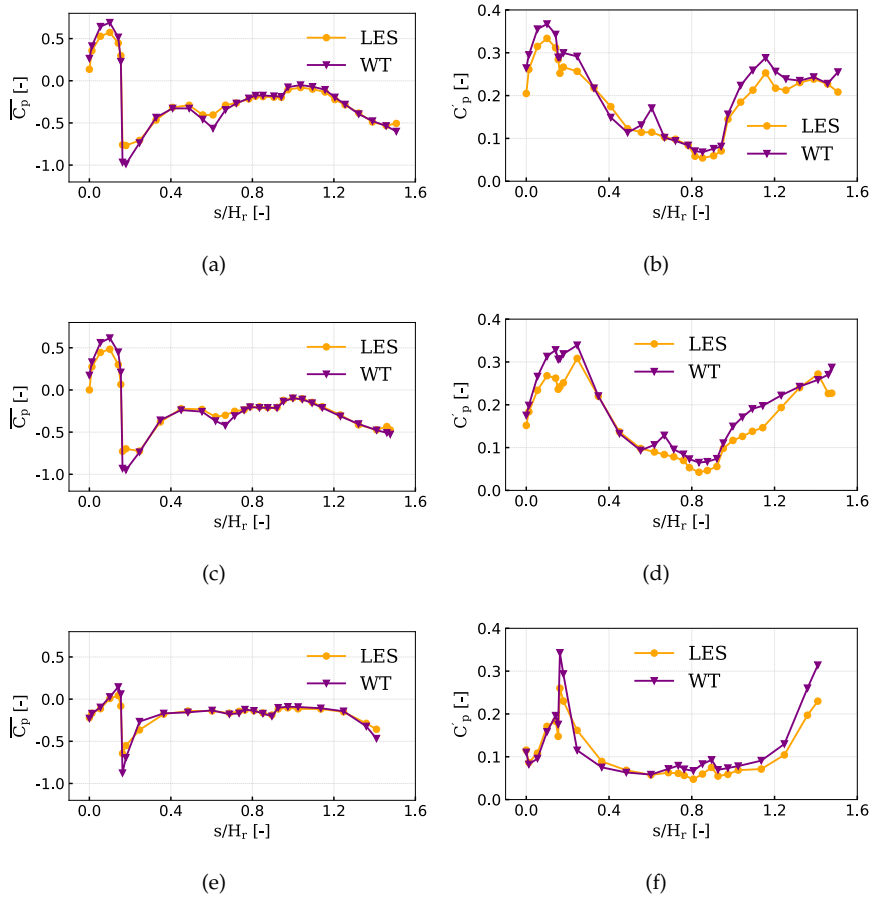


Fig. 3.13. Pressure coefficient statistics at 0° angle of attack: (a) \bar{C}_p and (b) C'_p for Top path, (c) \bar{C}_p and (d) C'_p for Medium path, (e) \bar{C}_p and (f) C'_p for Bottom path.

Fig. 3.14 shows the distribution of the C_p time-average and standard deviation for the angle of attack 240° , which correspond to a wind perpendicular to the long building side. Results qualitatively confirm those obtained for 0° , although in this case a systematic underestimation of the time-average and standard deviation of pressure is observed. Given the complexity of the model it is difficult, and probably not useful, to detail the cause of the discrepancies.

Nevertheless, as those are observed on the face of the building directly hit by the incoming wind, it might be conjectured that they are related to differences in the impinging turbulent structures produced by the surrounding buildings.

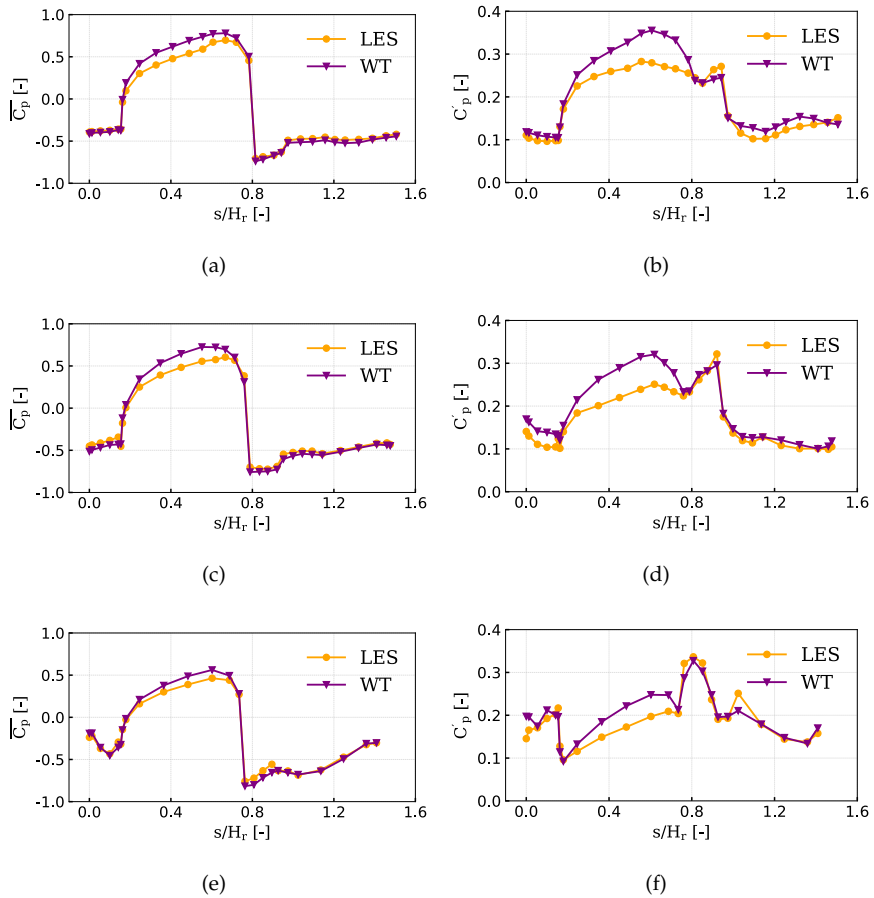


Fig. 3.14. Pressure coefficient statistics at 240° angle of attack: (a) \bar{C}_p and (b) C'_p for Top path, (c) \bar{C}_p and (d) C'_p for Medium path, (e) \bar{C}_p and (f) C'_p for Bottom path.

In order to provide a global overview of the obtained results, scatter plots which related experimental measurements and simulation results are proposed

3.5. Results

in Fig. 3.15 and 3.16. Here six angles of attack, equally distributed along all possible directions, are considered. Results are presented using different markers to allow to identify the face (see Fig. 3.3(c)) to which pressure taps belong. The coefficient of determination, R^2 , of experimental and numerical data is reported in Table 3.2.

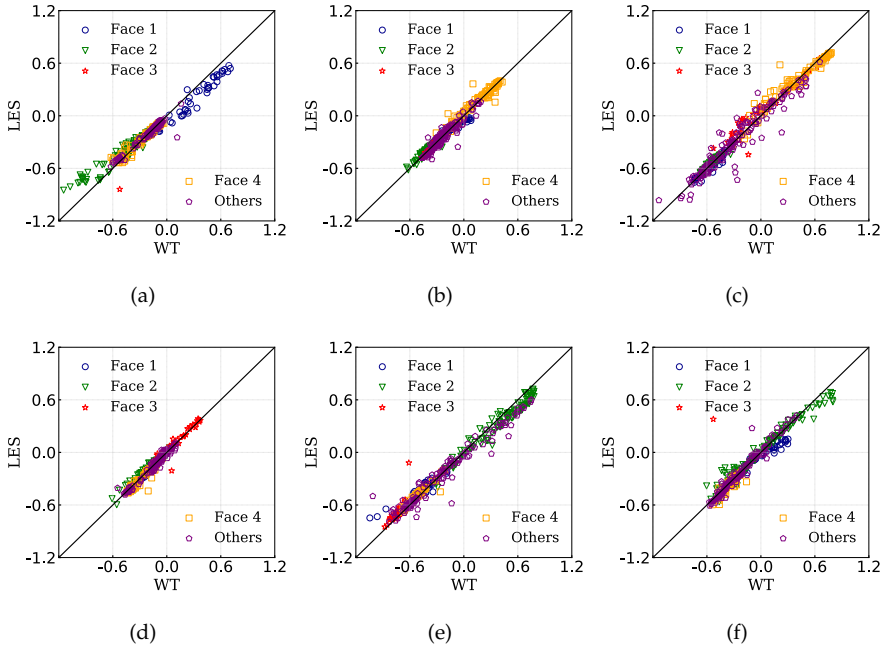


Fig. 3.15. Scatter plots of \bar{C}_p : (a) 0° , (b) 60° , (c) 120° , (d) 180° , (e) 240° and (f) 300° .

Analogously, for the pressure coefficient standard deviation, results are presented in Fig. 3.16. Also in this case, R^2 is reported in Table 3.2.

Table 3.2: Coefficient of determination, R^2 , of each wind angle of attack.

	0°	60°	120°	180°	240°	300°	Mean
\bar{C}_p	0.95	0.93	0.90	0.92	0.96	0.91	0.93
C'_p	0.92	0.89	0.70	0.92	0.78	0.87	0.85

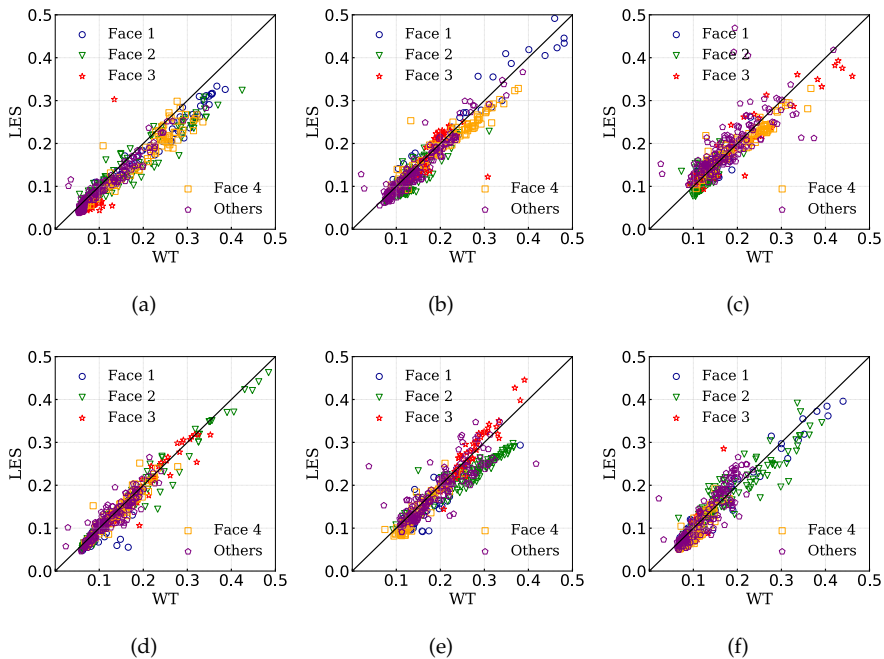


Fig. 3.16. Scatter plots of C_p' : (a) 0° , (b) 60° , (c) 120° , (d) 180° , (e) 240° and (f) 300°

3.5.4 Global forces

Up to now we provided an overview of the first and second order pressure statistics distribution. Here we provide an assessment regarding the accuracy of global forces, expressed in terms of aerodynamic coefficients based on the tower height. In particular, forces have been calculated by integrating the pressure field, so leading the forces time-histories. Then, for each angle of attack, the mean value and peak design values have been extracted assuming a Gumbel distribution for the extremes. Quantiles associated to 90% probability have been extracted for wind tunnel data while the extremes for numerical simulations are extracted directly from the time history. Results are shown for each force (moment) in Fig. 3.17 showing very good results in terms of time averaged values and a very good reproduction of the envelope shape for

3.5. Results

almost all angles of attack. We notice a relatively large discrepancy for the simulation at 300° which further inspection revealed to be caused by a single event recorded within the simulation.

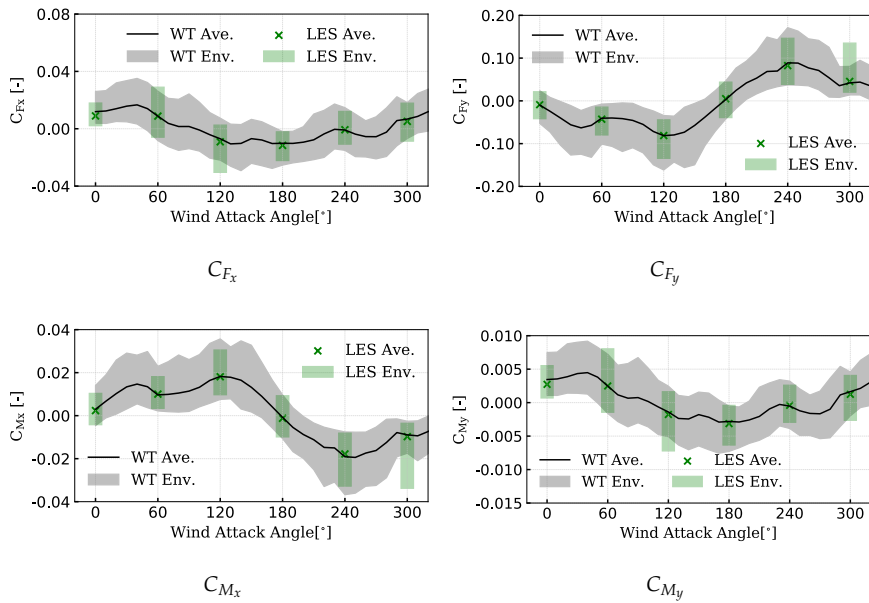


Fig. 3.17. Comparison between experimental and simulated global forces and moments.

3.5.5 Peak pressures

Similarly to what has been done in Sec. 3.5.2, we now proceed to analyse the extreme values from all considered angles of attack. Results are summarized in Fig. 3.18 as regards maxima and in Fig. 3.19 as regards minima. Also in such plots the numbering of the pressure taps have been changed for the sake of clearness, ordering them in ascending order with respect to the wind tunnel mean extreme value (maximum and minimum respectively).

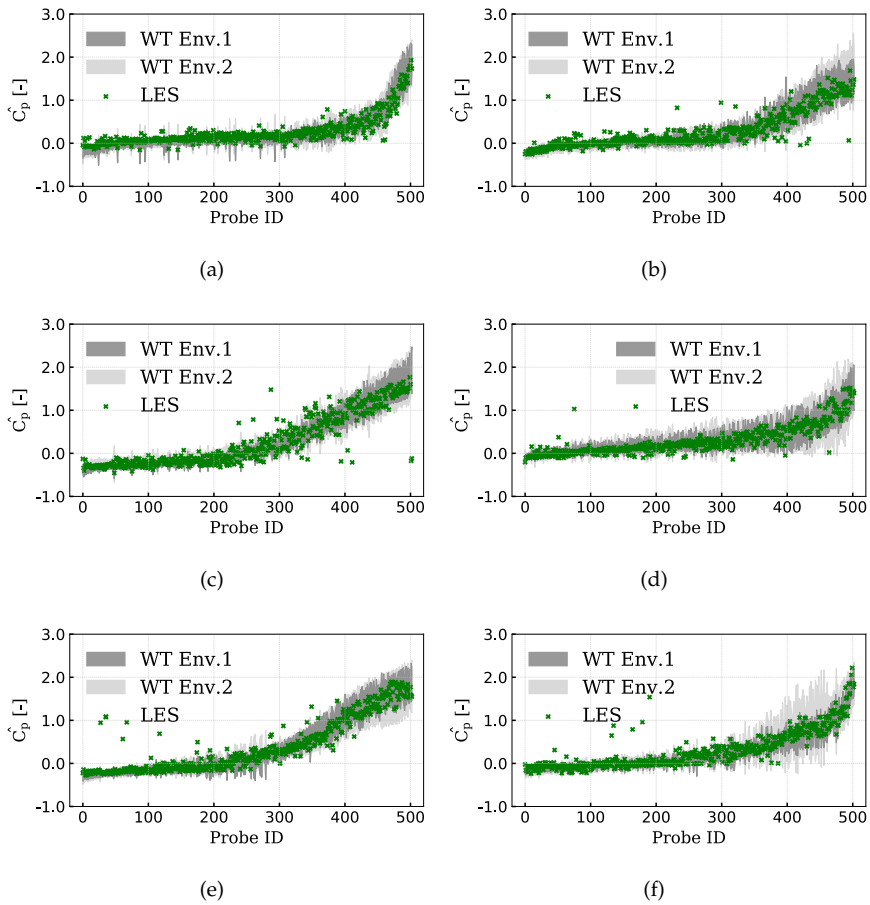


Fig. 3.18. Maximum predicted C_p : (a) 0° , (b) 60° , (c) 120° , (d) 180° , (e) 240° and (f) 300°

3.5. Results

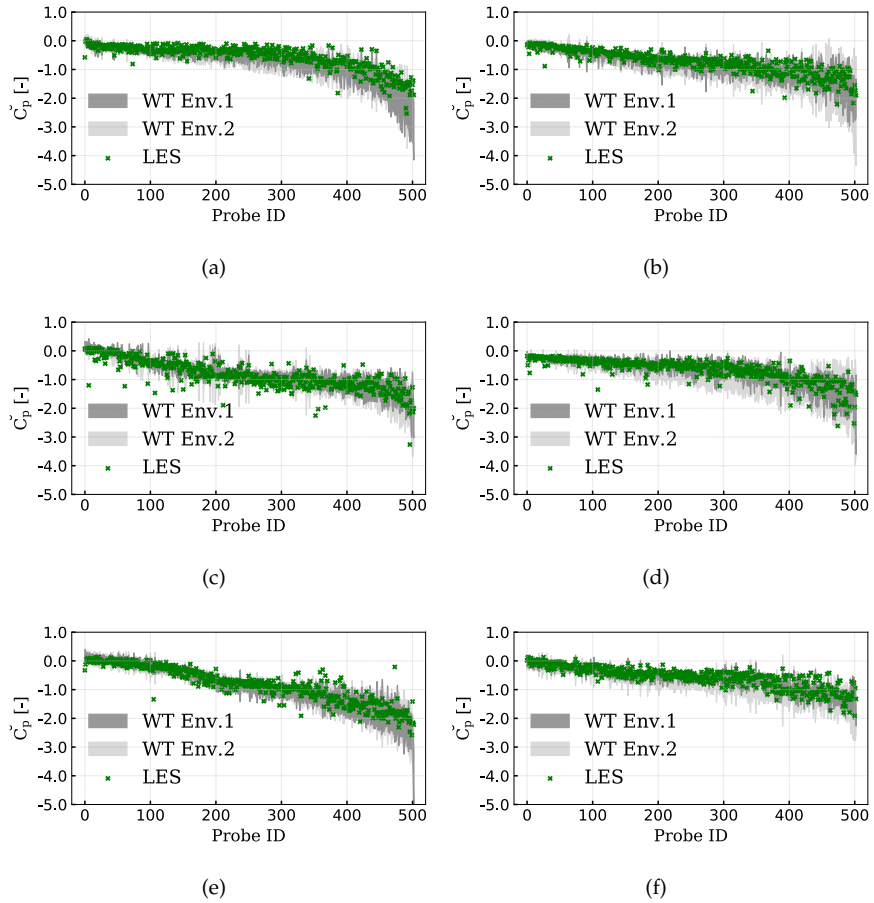


Fig. 3.19. Minimum predicted C_p :(a) 0° , (b) 60° , (c) 120° , (d) 180° , (e) 240° and (f) 300°

In this case, data are compared with two envelopes extracted from wind tunnel data. In particular, *Envelope 1* is extracted from the 10-min extremes measured in wind tunnel tests (Gumbel distribution, 90% probability). As regards *Envelope 2*, it is obtained by calculating 90% probability 10-min extremes for the considered angles and incrementing it of $\pm 10^\circ$. This is done in order to qualitatively evaluate if a small change in the angle of attack can be considered responsible for the observed discrepancies.

Table 3.3 reports the percentage of extremes falling within the previously calculated confidence interval for all the considered cases. As it can be seen, results previously presented are confirmed. The numerical simulations fall inside the calculated *Envelope 1* type confidence interval an average of 80% of the times. When *Envelope 2* is considered, the scores is in the order of 90%. Despite those error metrics, it should be anyway noticed that numerical results tend to accumulate in the lower zones of the calculated confidence intervals. This is particularly evident for Fig. 3.19 (a) and (e), for which, at high suction, the peak values measured in the simulations tend to cumulate at milder suction values. On such regard, further research is needed as the evaluation of peak loads by means of numerical simulation, despite its importance, has not been deeply investigated in the literature.

Table 3.3: The percentage of extremes falling in the WT confidence interval.

Peak types		0°	60°	120°	180°	240°	300°	Mean
Maximum	Inside Env.1 ratio (%)	74.8	84.9	68.0	87.3	80.7	69.8	77.6
	Inside Env.2 ratio (%)	87.5	91.8	84.7	95.0	93.0	90.3	90.4
Minimum	Inside Env.1 ratio (%)	77.3	88.3	75.1	87.1	80.9	75.7	80.7
	Inside Env.2 ratio (%)	88.5	94.4	86.5	94.6	91.3	86.7	90.3

3.5.6 Computational costs

In this section the computational costs involved in running the proposed simulations are detailed and the budget for a complete study is discussed.

The proposed simulations have been run at CINECA, on the GALILEO supercomputer, which is equipped with 1022 nodes each composed of 2x18-core Intel Xeon E5-2697 v4 (Broadwell) at 2.30 GHz. Running each simulation with a number of cores comprised between 100 and 200, each simulation required approximately 5000 *Core-h* to complete for the *Mesh M 10 min* in real scale, which should be considered a minimum requirement in agreement, for instance, with CNR [142].

Although in the present study, for the sake of convenience, simulations have

3.5. Results

been performed every 60° , a stepping comprised between 10° and 30° is usually required [142]. Assuming for instance to sample the attack angle every 30° , this requires 12 simulations to complete the attack angles.

It is thus easily possible to see that a complete study performed as described in this paper requires approximately $6.0E4$ *Core-h* if every angle of attack is sampled for 10 *min*, while it would require $3.6E5$ *Core-h* for a 1 *h* sample in full-scale, from which a more careful evaluation of the extreme values can be obtained.

According to Recale [143], Wallker [144], we here assume a cost of the *Core-h* equal to 0.1 euro (this might be considered an average value with typical oscillations of about 20%). This leads to a total cost comprised between 3k and 50k euro, which is indeed the range of price of wind tunnel tests.

It is nevertheless noticed that the cost structure of wind tunnel tests and numerical simulations is completely different: the first ones are characterized by fixed costs due to the wind tunnel infrastructure and the model production and installation, being the actual tests relatively quick and inexpensive. On the other side, CFD is characterized by relatively low fixed costs for the simulations setup, while variable costs increase linearly with the simulation time and the number of studied configurations.

It thus appears that in a complex case as the selected one, numerical simulations are competitive with wind tunnel evaluations only if economy is made on the number of considered attack angles and/or, length of the time-histories and configurations (we remind that in wind tunnel tests actually two configurations have been tested with a 10° stepping). On the other side, when it is possible to study a reduced number of incidence angles (e.g. due to symmetry) or due to the expected structural behaviour, CFD already appears as an optimal choice, although carefulness has to be used in evaluating local peak pressures.

3.6 Conclusions

In the present paper, the recently designed Torre Gioia 22 has been selected as case study for the evaluation of the wind loads based on CFD simulations. The analyses showed a good capability of numerical simulations to reproduce wind tunnel tests, being the most important source of discrepancy the difficulty encountered in numerical simulations in the reproduction of extreme suction. Local refinements in the immediate proximity of the building surfaces were able to alleviate the problem but not to eliminate such effects, which probably require a finer mesh sizing in a wider zone close to the building, so remarkably increasing the computational costs.

In particular, we remark that mesh sizing and numerical schemes which, in the authors' experience, provide a reasonable compromise between accuracy, computational cost and numerical stability have been reported. Such settings are indeed problem dependent and well-adapted to sharp-edged bluff bodies immersed in mildly and highly turbulent flows. In particular we here recall:

1. the mesh size here adopted in the proximity of the studied structure has size comprised between $0.01H_r$ and $0.005H_r$, being H_r the object characteristic scale. In the authors' experience, the addition of boundary layer cells is often found to be very costly (especially due to the consequent requirements in terms of stable time step) and often unnecessary;
2. the use of partially-corrected schemes can be used in order to increase the computations stability. Although suboptimal such choice is often unavoidable and leads to acceptable results;
3. as it is well-known, the synthetic inflow can be generated by various available methods. The authors briefly reported the factors which, in their experience, mainly contribute to their success and led to the development of the PRFG³ here adopted;
4. the fact that synthetic inflows inevitably lead to the insurgence of spurious pressure fluctuations (at least due to incompatibility with other boundary conditions) at the inflow has been discussed and the VBIC procedure used to alleviate such effect.

3.6. Conclusions

Finally, the computational cost of such simulations is analysed. It appears that at the current stage, the cost of running accurate numerical simulations is still comparable, if not higher, than wind tunnel tests. This is particularly true in the case of complex surroundings or multiple design scenarios. However, the use of numerical simulations appears to be already well-suited for cases in which it is possible to define *a priori* a limited number of conditions to be tested.

As a result, while it is not difficult to foresee a future in which numerical simulations will overtake wind tunnel tests, the two techniques currently appear optimal in different conditions. Further research is still needed in order to allow a more rational use of numerical simulations: between them the use of multi-fidelity approaches and *a priori* identification of critical conditions appear to be the most promising ones.

4 Early stages wind load assessment using Computational Fluid Dynamics: The new Bologna Stadium roof

The use of Computational Fluid Dynamics (CFD) is rapidly expanding, allowing to complement traditional wind tunnel tests even in the case of extremely complex geometries at reasonable computational costs. In this contribution, we report the experience gained in the preliminary study of the new roof over the Bologna Stadium. The study, performed prior to wind tunnel tests, is meant to provide the designer a first evaluation of wind loads in early design stages, with classical wind tunnel tests planned at the final design stage. The most critical loading conditions are identified and the structural response evaluated. Finally, the structural response sensitivity to damping, which is difficult to be accurately evaluated *a priori*, is assessed. The study shows how early CFD simulations can effectively complement traditional wind tunnel tests in the project development.

4.1 Introduction

As it is well-known wind-induced dynamic loading plays a crucial role in the design of large-span structures such as stadia [145, 146]. However, in modern architecture, the shape of the roof is characterized by high variability and

providing general guidelines for the evaluation of wind loads acting on sub-horizontal surfaces is far from being an easy task. As a result, only a few standardized geometries are considered in codes and standards (see for instance [137, 147]), and extrapolating the case of interest starting from these known cases usually comes with great uncertainties.

For this reason, long-span roofs are usually tested by means of Wind Tunnel Test, WTT, from which the time-varying pressure field acting on the roof is measured at several hundreds of points [148, 149]. Usually, based on the WTT output, the structural dynamic response is numerically calculated [150–152]. With the structural responses for all wind attack angles, the extreme values of the response are calculated for each structural element, leading to the definition of the so called design envelope. Finally, Equivalent Static Wind Loads, ESWLs, might be calculated for design purposes [153, 154].

Although WTTs are well-established and widely adopted, their preparation is cumbersome and requires expensive infrastructures, so that great advantages might be obtained by using numerical simulations. In this context, the use of CFD is rapidly spreading, leading to the so called Computational Wind Engineering, CWE.

Nowadays CWE is routinely adopted in many applications such as pedestrian level wind comfort and pollutant dispersion [117], but its use in field of wind loads evaluations is still debated, at least from the point of view of codification. In particular, at the time of writing, the approach used by standards to regulate the use of CWE is extremely variable. The Japanese guidelines [155] provide a remarkable amount of details regarding the use of CWE, also proposing validation cases. On the contrary, Eurocode [137] and ASCE [156] substantially ignore CWE, but updates are expected to appear soon. Finally, the Italian guidelines [147] consider CWE in a dedicated informative annex. Despite such differences, which mainly arise due to some skepticism in using CWE for the final design, there is little doubt that CWE analyses can be extremely useful in the preliminary design stage, providing an intermediate step between the use of standard cases found on codes of practice and detailed WTTs.

4.1. Introduction

Nevertheless, even in such context, the use of CWE for complex cases such as the analysis of a stadium roof is still uncommon. This is, at least partially, due to the fact that the use of computationally demanding scale resolving models is necessary for the assessment of structural vibrations [31, 157] and, thus, substantially mandatory even at the preliminary design stage for light structures.

In this paper, we present the preliminary study performed on the new roof of the Bologna Stadium, aimed at providing the designer a first evaluation of the structural response in the early stage of the design process, prior to the final design stage for which WTTs are planned. The study makes use of Large Eddy Simulation, LES, as well as various techniques developed by the authors in recent years, which provide a smooth and comprehensive procedure for wind loading assessment. The combined use of such techniques prove essential in order to allow for an efficient and robust methodology without excessive overheads for the structural engineer, which is of great importance for preliminary analyses.

In particular, the structural response is calculated relying on the structural modes, but quasi-static corrections [158] are adopted in order to compensate for the truncation of the modal base. Such corrections are calculated relying on Proper Skin Modes, PSMs, which can be seen as a modal version of the standard approach based on influence coefficients, evaluated applying unitary forces [159].

As it will be seen, even for preliminary analyses, relatively high fidelity simulations are adopted and the structural response is calculated up to evaluating design values for each structural member. This allows to make an early assessment, for instance, of locations showing particularly high peak pressures which can be used to guide the disposition of pressure taps in subsequent WTT, to individuate the most critical wind directions and study the effect of structural damping. In particular, such last aspect might be used in order to evaluate the opportunity to perform dedicated studies aimed at providing a more precise evaluation of such parameter and/or to guide the design of mitigation systems.

Finally, we also comment on the extraction of ESWLs which can be easily used for design purpose. In particular, ESWLs are here extracted by means of a slightly modified procedure with respect to that already presented by the authors [160] and they are used in order to provide to the designer static loads which can be used to refine predictions based on codes of practice.

We would like to stress that it is not the aim of this paper to provide an evaluation of LES models accuracy for large-roof structures, which would be impossible for the investigated case, as WTT have not been planned at the time of writing. What we aim to do here is to provide a description and assess the potential of numerical simulations as a complementary tool with respect to WTT, showing its practical application in a complex case.

The paper is organized as follows: in Section 4.2 the numerical settings of the LES analyses are outlined. The qualitative descriptions of the obtained flow fields are reported in Section 4.3. Subsequently, the calculation of the structural response and the extraction of ESWLs is discussed in Section 4.4. Finally, conclusions are drawn in Section 4.5.

4.2 Numerical model

In this section, the setup adopted for the CFD analyses is discussed. The geometry of the roof and the surroundings are described in Section 4.2.1, the adopted mesh and the numerical schemes are outlined in Section 4.2.2. Finally, in Section 4.2.3 the generation of turbulent inflow conditions is addressed.

4.2.1 Description of the stadium

The stadium, Stadio Renato Dall'Ara, was built approximately a century ago and later deeply renovated for the 1990 FIFA World Cup. It currently has a capacity of more than 38000 people, as the home of the Bologna football club. The proposed project is to renovate the stadium and add a semi-closed large-span roof, designed by MJW structures [161]. The outline of the structure is depicted in Fig. 4.1 and its dimensions are planned to be 227 m in length and 160 m in width. The roof is located at a height of approximately 35 m and

4.2. Numerical model

it is composed by an outer open-ring-like structure covered by opaque membranes and an inner translucent ring-like structure. The two are separated by a gap which allows the air flow and are supported by primary reticular structures (Fig. 4.1 (b)) and secondary curved beams (Fig. 4.1 (c)) surmounting them. The stadium roof is composed of approximately 4000 beams/trusses elements and it is subdivided into four sectors, shown in Fig. 4.1 (c). To be noticed is also the presence of a structure of height 42 m denoted Torre di Maradona, located at the middle of one of the long stadium sides.

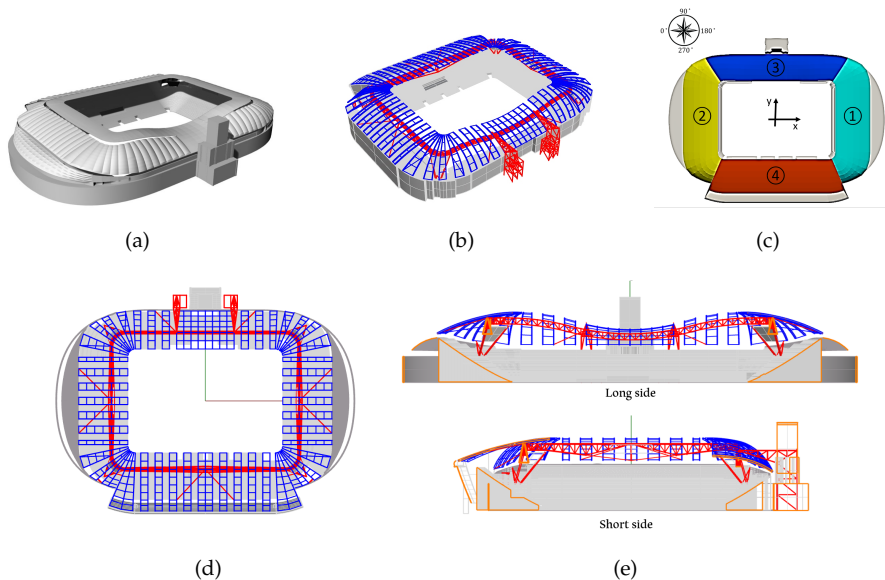


Fig. 4.1. The Bologna Stadium: (a) the view of the roof, (b) the primary (red) and secondary (blue) structures, (c) the roof subdivision into sectors, (d) plane view of the structural system and (e) vertical sections. (For interpretation of the references to colour in this figure legend, the reader is referred to the web version of this article.)

4.2.2 Numerical model for the wind flow simulation

We proceed at simulating the structure by means of Large Eddy Simulation, LES, in full-scale, but the Reynolds number has been decreased by increasing

the air viscosity of a factor 300 in order to increase the stability of the computations, i.e. by decreasing the cell Reynolds number [162]. This amounts to the fact that the simulated Reynolds number is comparable to that of a 1:300 scaled model, which is a quite standard scale for WTT. While numerical simulations are theoretically able to simulate full-scale conditions, this can hardly be obtained in practice if not for very simple cases or at high computational costs, which in this context appears unjustified due to the aforementioned consolidated WTT practice. The Reynolds number based on the roof height is approximately 2.94×10^5 . The computational domain measures 1750 m, 1300 m and 340 m in length (streamwise direction), width and height, respectively, as shown in Fig. 4.2. The distance from the inlet to the stadium is 750 m. The origin of the reference system is located on the ground at the center of the stadium. Neighboring buildings within a distance of 450 m are explicitly simulated (see Fig. 4.3). The first problem to be solved is that the stadium lies at the foot of the Apennines, so that the terrain varies remarkably in height within the area for which surroundings are explicitly reproduced. We decide to proceed with a rotor-stator approach as in standard WTT to avoid the need to re-mesh for each angle of attack (as all attack angles are obtained simply by rotating the rotor part). It is thus necessary, again in agreement with common WTT practice [142], to build a model in which the geometry of the hilly terrain is trimmed and smoothly connected to a flat surface representing the level imposed by the stator. The blockage ratio of the model is lower than 1%. All structural elements composing the roof have been removed (both main reticular beams, cables and secondary beams), so leaving only the main surfaces.

4.2. Numerical model

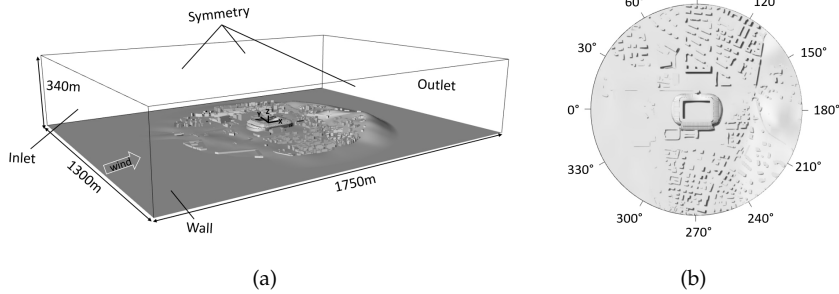


Fig. 4.2. The computational domain and the boundary conditions (a) and indication of wind attack angles (b).

The mesh size in the zone spanning from the inlet to the rotor has a maximum size of 6 m, in order to allow for the transport of the turbulence generated at the inflow up to the stadium without excessive dissipation. In the proximity of the stadium the mesh size is decreased up to approximately 1.5 m while in the proximity of the roof edges it is kept at approximately 0.75 m. The mesh is then coarsened downstream the rotor reaching a maximum size of 12 m. The total cell count is approximately 8.5 M.

The ground, the surroundings and the stadium surfaces are modeled as walls. The stadium roof is modelled considering the minimum thickness (0.2 m) which allowed to obtain a good result in terms of meshing. Roughness has been added using rough wall-functions in the zones outside the rotor (where surroundings are not explicitly modelled) in order to match a Category III Eurocode terrain [137], while Van Driest damping is used for the stadium and the surroundings. Symmetry conditions are used on the top, front and the back surfaces of the domain, which are commonly used to model wind tunnel walls. The rotor and the stator are coupled by means of non-conforming interfaces, i.e. at the interface the mesh used for the rotor does not need to be the same as that used for the stator. The inlet boundary condition is generated using the synthetic turbulence generator, PRFG³, discussed later in Sec. 4.2.3. A k-equation subgrid model is adopted [135].

Gradients and Laplacians are calculated using the Gauss linear scheme while advective terms are approximated using the bounded linear scheme for k and the LUST scheme for the velocity field [136]. Pressure-velocity coupling is obtained with the well-known PISO algorithm [163] and time advancement is obtained using a Crank-Nicolson scheme blended with 10% backward Euler scheme. The pressure field is solved using the GAMG solver, while the velocity field is solved using the Gauss-Seidel smoother. Simulations are performed using OpenFoam 6.

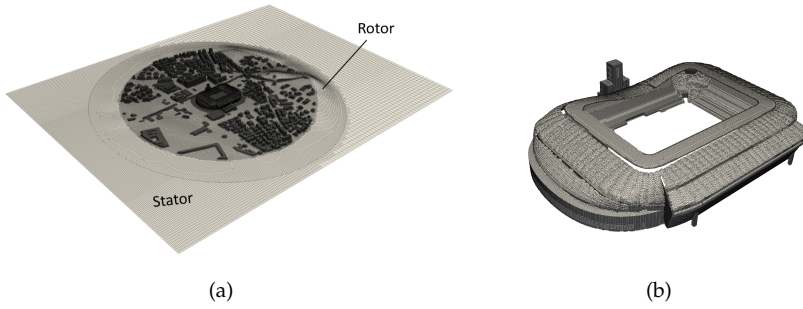


Fig. 4.3. The mesh distribution (a) and the details of the meshed stadium (b).

To evaluate the wind effects on the stadium roof and predict the extreme wind loads, the simulation time should last for at least 700 s (600 s, i.e., 10 min, for simulation and 100 s for model initialization). Notice that this is truly a minimum requirement as the extraction of extreme values would require multiple samples of 10 min each. However, this would strongly increase computational costs so that, for preliminary analyses, we here proceed considering only 1 sample of 10 min for each angle of attack and consider a total of 12 wind attack angles, uniformly spaced every 30° , as indicated in Fig. 4.2 (b). The time step is 0.012 s, which leads to stable computations and to average Courant numbers around the stadium well-below 1 with extremes around 5 only in few small-size cells. To ensure the computational stability, the inflow velocity is ramped up from null value to the final value in 10 s. Each angle of attack is run on 192 CPUs and requires approximately 2800 CPUh.

4.2. Numerical model

The roof of the stadium is equipped with 3820 pressure taps, organized in 1910 pairs, i.e., on both upper and lower surfaces, to allow the measurement of net pressure, as indicated in Fig. 4.4 (a).

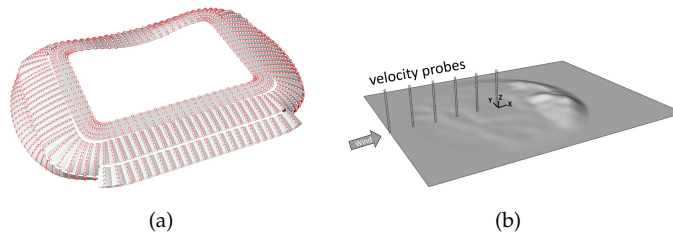


Fig. 4.4. The distribution of the pressure probes on the stadium roof (a) and the velocity probes in the empty domain (b).

4.2.3 Synthetic turbulence inflow generation

According to the local wind climate, site roughness and code prescriptions, the inflow turbulence is generated based on the Category III Eurocode (EC) profile [137], assuming a base velocity of 25 m/s from all directions [142]. The reference height, H_r , is 40 m, so that the reference velocity there measured, U_r , is 27 m/s.

Firstly, a wind field in an empty domain is simulated to evaluate the wind profiles at the stadium location. Simulations have been run on both a completely empty domain and a domain in which the topography of the surroundings (without buildings) are considered, with the hilly part downstream the stadium to minimize its effect (Fig. 4.4 (b)). This is done in order to make sure that the irregularity of the mesh close to the ground caused by the presence of the orographic elements does not cause excessive modifications of the profiles with respect to the completely empty case (which has a regular mesh close to the ground). The comparison between the two solutions, not here reported for the sake of brevity, did not highlight discrepancies between the two.

The turbulent inflow is generated through a turbulence synthesizer recently proposed by the authors, PRFG³ and applied to the inflow patch using the

VBIC technique, able to moderate pressure fluctuations induced by synthetic inflows. Readers are invited to refer to [33, 34, 111] for details. The comparison between the target and the simulated wind profiles are shown in Fig. 4.5. As can be observed, a good agreement can be obtained through the implemented turbulence synthetic generation procedure. The turbulence intensity of all three velocity components, u , v and w , at H_r is around 20%, 19% and 10%. Integral length scales reported in 4.5 (c) have been calculated using Taylor hypothesis of frozen turbulence from time-histories and are found in agreement with usual prescriptions. Notice that this is a parameter for which target values are known only very approximately, as large scatters are present in available site measurements.

As for the spectra at H_r , the results are presented in Fig. 4.6. The simulated results agree well with the targeted spectrum in the low-frequency region and show the classical cut-off frequency at approximately 0.6 Hz. In order to obtain such results, the turbulence intensity of all velocity components has been increased at the inflow of about 20% to compensate for the dissipation registered between the inflow and the stadium location. Avoiding such problem by refining the mesh, although surely preferable, would increase the computational cost substantially and, thus, such approach was not here followed. It shall be noticed that, aiming at calculating the structural response, the cut-off frequency shall be chosen in order to be higher than the structural vibration modes of interest, which in this case are in the order of 1 Hz (see Sec. 4.4.1). Although not optimal, the present result is retained considering that the model in which the surroundings and the stadium are placed is characterized by mesh size 2 to 4 times finer than empty domain conditions, leading to a cut-off frequency of 1.2 to 2.4 Hz. Indeed, small scale structures will be produced by the explicitly simulated obstacles to a large extent, so that for preliminary simulations the obtained results appear to be acceptable.

4.3. Characterization of the flow field

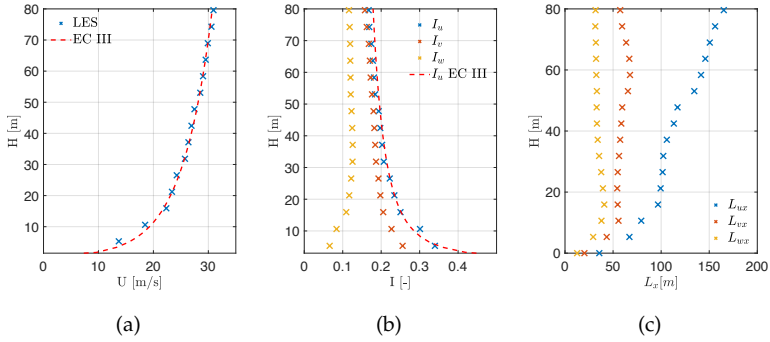


Fig. 4.5. Velocity profiles obtained from the empty domain test: (a) mean velocity profiles, (b) turbulence intensity profiles and (c) turbulence length scale profiles.

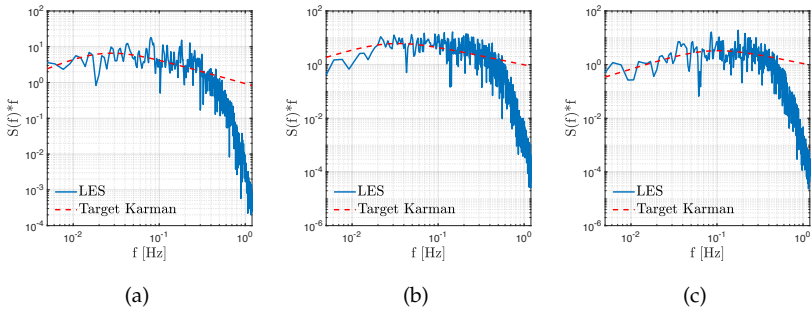


Fig. 4.6. Spectra of the velocity components measured at H_r : along-wind component (a), cross-wind component (b) and vertical component (c).

4.3 Characterization of the flow field

In this section, the simulated flow fields and the pressure distribution acting on the stadium roof are described. Firstly, in Section 4.3.1, the instantaneous flow fields obtained from the LES are presented. Then, the recorded pressure field is characterized in Section 4.3.2 and Section 4.3.3. Finally, global forces and moments are analyzed considering all wind attack angles.

4.3.1 Instantaneous flow field

Fig. 4.7 reports the instantaneous flow fields represented by Q-criterion iso-surfaces colored by U/U_r over the computational domain and the stadium, being U the instantaneous velocity magnitude. The turbulent structures produced by the stadium itself and the surrounding structures can be clearly seen, with the presence of large size vortices impinging on the roof oppositely to the side/corner they detach from.

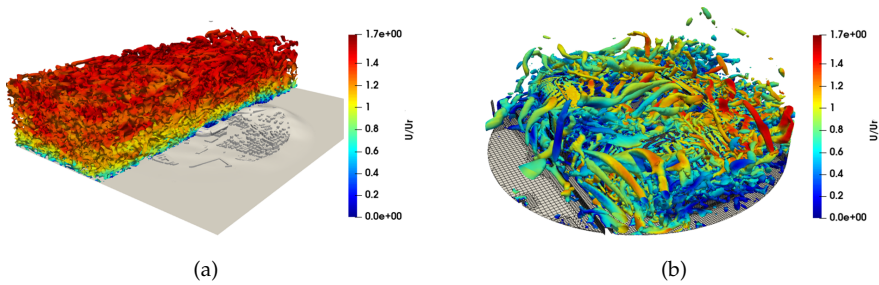


Fig. 4.7. Overview of the flow field by means of instantaneous Q-criterion iso-surfaces colored by U/U_r : (a) overall domain ($Q = 0$) and (b) around the stadium at 120° ($Q = 2$).

Fig. 4.8 shows two scenarios, with wind coming from the flat terrain part (30°) and the hilly terrain part (210°), respectively. In particular, the figure reports the value of the turbulent kinetic energy (not to be confused with the subgrid turbulent kinetic energy).

It can be seen that, as expected, while having a shielding effect on the stadium, the wind coming from the hill is expected to have stronger gusts compared to that coming from the flat terrain, so potentially leading to a larger dynamic response of the roof.

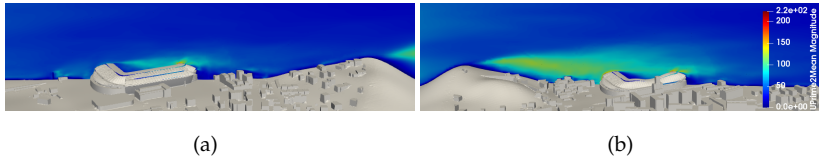


Fig. 4.8. Flow visualization of the wind coming from different terrains, colored by $(|U'|/\bar{U})^2$: (a) 30° and (b) 210° .

4.3.2 Proper Orthogonal Decomposition

In order to characterize the pressure field acting on the stadium roof from different angles of attack, we here consider the well-known Proper Orthogonal Decomposition (POD). Readers interested in a methodological review of POD in wind pressure analysis can refer to [164]. In this context, we use POD decomposition mainly for two reasons. The first one is that it allows to obtain a synthetic characterization of the fluctuating pressure fields and make qualitative judgements relatively to the induced structural response. In fact, energy concentration in a few POD modes and their similarity to the structural modes shall be regarded as a situation prone to lead to large structural responses. Secondly, and even more importantly, numerical instabilities in the CFD models might lead to unexpected concentrated pressure fluctuations, easily identifiable observing the POD decomposition. In the best cases such instabilities lead to large fluctuations of the Courant number and, finally, to global instability of the simulation. Nevertheless, in some cases, they are more insidious and thus, a preliminary POD decomposition of the obtained results is always advisable.

Fig. 4.9 shows the first POD mode of the pressure field when wind attack angles are 0° , 30° , 60° , 90° , 120° and 150° . As expected, for all considered wind attack angles, the highest pressure variations occur at the inner edge downstream the incoming wind direction. It can be seen that pressure fluctuations are concentrated on narrow stripes close to the edge for 90° angle of attack, so that it can be expected that such angles might be more relevant for the definition of local peak pressures than for the response of the primary structure.

Contrarily, skew angles such as 60° lead to high levels of pressure fluctuations over all the longest span of the roof, so anticipating that they might be the more relevant incidence angle for the global structural response evaluation.

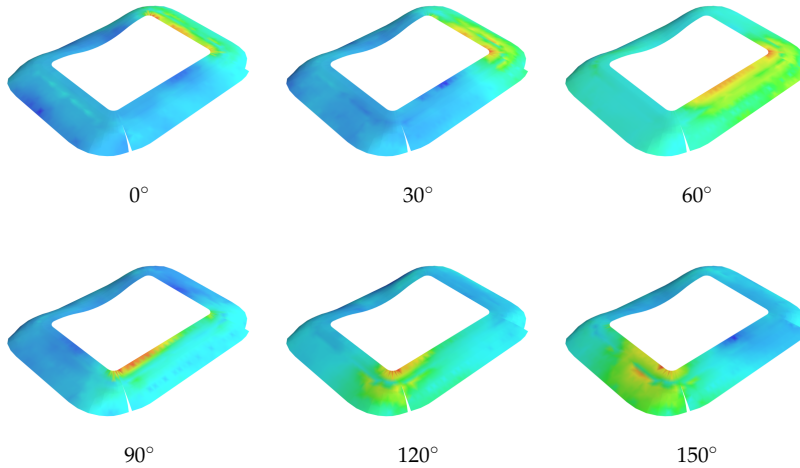


Fig. 4.9. Proper Orthogonal Decomposition, an overview of the first mode for angles up to 150° (colorbar not reported as the POD modes are not defined in amplitude.) (For Interpretation of the references to color in this figure legend, the reader is referred to the web version of this article.)

For each case, the percentage of the total variance produced by the first POD mode is reported in Fig. 4.10 (a), while the number of POD modes necessary to cumulatively represent 25% and 75% of the total variance are shown in Fig. 4.10 (b) and (c).

Looking at Fig. 4.10 (a), we notice that the angles of attack showing the highest variance explained by only the first POD mode are those with the wind approaching from a short side (i.e., 0° and 180°). Conversely, those for which the explained variance is lower, correspond to the wind approaching orthogonal to the long side of the stadium. Looking now at Fig. 4.10 (b), in order to reach 25% of the total variance it is necessary to consider only 3 POD modes when the wind is approaching from a short side, while it takes up to 5 POD modes

4.3. Characterization of the flow field

when the wind approaches from the long sides. Finally, considering Fig. 4.10 (c), we see that 40 to 50 POD modes are necessary to explain 75% of the total variance. Overall, data indicate that when the wind approaches orthogonal to the short sides, the aerodynamic excitation concentrates in a low number of modes and mainly affects the corresponding downstream sector. However, the excitation of the shorter sides is less demanding from the structural point of view with respect to the long ones, so that the balance between such two aspects must be further analysed by calculating the structural response, as later reported.

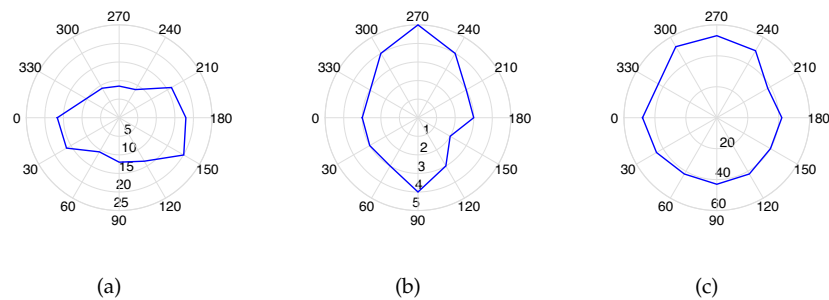


Fig. 4.10. Proper Orthogonal Decomposition of the pressure field: (a) energy of the first mode (percentage), (b) number of modes required to obtain 25% of total energy and (c) number of modes required to obtain 75% of total energy.

4.3.3 Peak pressure distribution

The peak pressure (i.e., minimum and maximum) distributions are presented in Fig. 4.11. Notice that we here always speak about the net pressure, difference between the top and bottom surfaces composing the roof. The extreme values are extracted for each monitor pair assuming a Gumbel distribution for the 10 min peaks and calculating quantiles with non-exceedance probability equal to 80%, following the well-known Cook and Mayne approach [114]. It shall be noted that, as the duration of the simulated time series is 10 min, it is necessary to extract quantiles related to 2 min extremes and, then, shift them according to the well-known shifting property of the Gumbel distribution in

order to recover the 10 min peaks quantiles [113]. In essence, the approach assumes that the Gumbel distribution can fit the data with reasonable accuracy and that 2 min extremes are independent variables. Notice that alternative solutions able to extract peak values from short time-histories have been recently proposed for instance in [165].

As expected, strong suctions and overpressures are predicted along the whole inner ring. The analyses suggest the presence of relatively high local pressures also in the proximity of the gap between the opaque and the translucent portions of the roof, which might be better investigated in WTT.

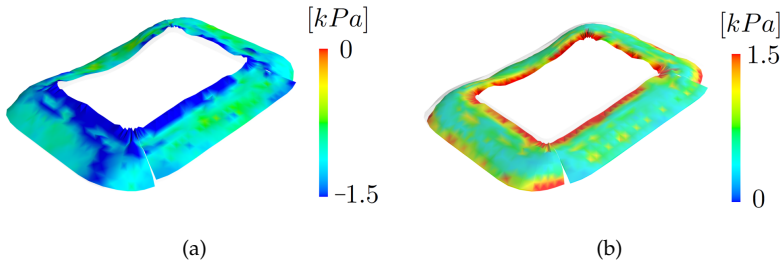


Fig. 4.11. Peak pressures evaluated following Gumbel procedure with non-exceedance probability equal to 80% considering all attack angles: (a) minima and (b) maxima. The values are limited to the range -1.5 to 1.5 [kPa] in order to allow an easier visualization of the distribution.

4.3.4 Global forces

Before proceeding to the evaluation of the structural response, we here consider the global forces acting on each roof sector (see Fig. 4.1 (c)). The time-averaged and the peak values of the global forces in the z direction, F_z , are shown in Fig. 4.12. In particular, we report the time-averaged values, the gaussian envelopes (obtained by adding/subtracting to the mean 3 standard deviations) and the actually observed extreme values. Again, it can be clearly seen that for each sector the worst case condition is represented by the detachment of vortices from an upstream located sector. In some conditions (see for instance *Sector 4* at 60°), the response is strongly non-gaussian, so that the

4.3. Characterization of the flow field

recorded extreme values fall outside the gaussian envelope. We notice that *Sector 3*, probably due to the particular curved shape which makes it stand at a lower height on average, does not appear to interact with vortices detached from *Sector 4*. Its response is generally gaussian with good approximation and more evenly distributed with the attack angle.

For the sake of completeness, we now provide a rough comparison between the obtained results and that which might be deduced applying codes and standards. In particular, the peak dynamic pressure coefficient, C_q can be evaluated as $C_q = 1 + 2gI_u$, being g a peak factor usually equal to 3.5. Considering that $I_u \approx 0.2$ at roof height according to the present profile (see Fig. 4.5), $C_q = 2.4$. Comparing such value to the peak pressure coefficients reported in Fig. 4.12, suggests that: (a) the gaussian envelop, whose uplift maximum value is approximately 1.0 (*Sector2*) suggests a pressure coefficient $C_p = 1.0/2.4 = 0.41$, (b) the actually measured maximum value is 1.6 (still *Sector2*) suggesting a pressure coefficient $C_p = 1.6/2.4 = 0.66$. Such values are well-comparable to those usually found for sub-horizontal structures in codes of practices (see for instance [147]), being a more precise comparison not possible due to the peculiarity of the considered shape.

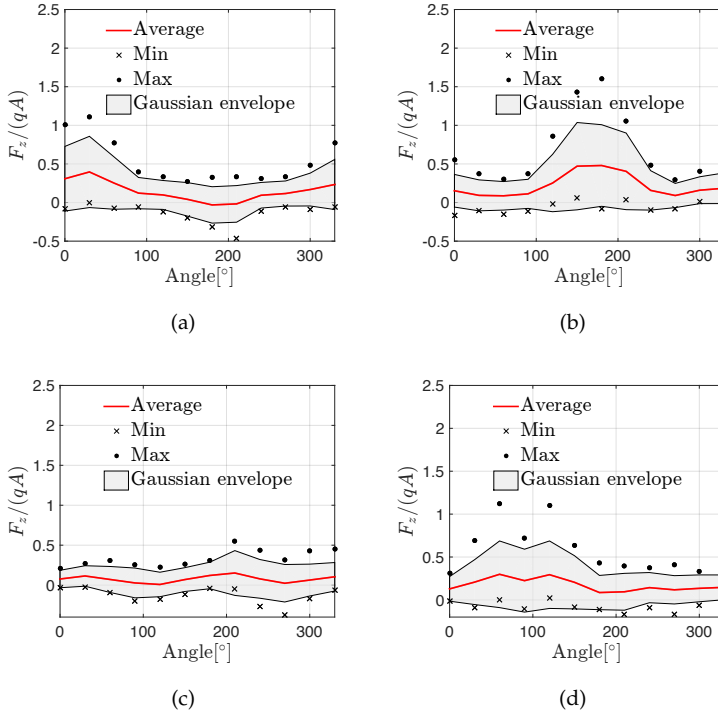


Fig. 4.12. Vertical force acting on each sector: (a) *Sector 1*, (b) *Sector 2*, (c) *Sector 3* and (d) *Sector 4*. Forces are made non-dimensional with respect to the reference pressure, $q = 0.5\rho U_r^2$, and the corresponding reference area, A .

Finally, Fig. 4.13 reports some meaningful statistics of the pressure field at 60° , which can be seen from Fig. 4.12 to be one of the critical angles for *Sector 4*. The figures highlight that very high values are observed at the roof edge, as expected, and that, due to the flow skewness, both \check{C}_p and \hat{C}_p are slightly asymmetric, so also triggering an asymmetric structural response. Notice that extreme values reported in the figure are the extreme punctual unfiltered values measured during the analysis, so explaining the high recorded suction values.

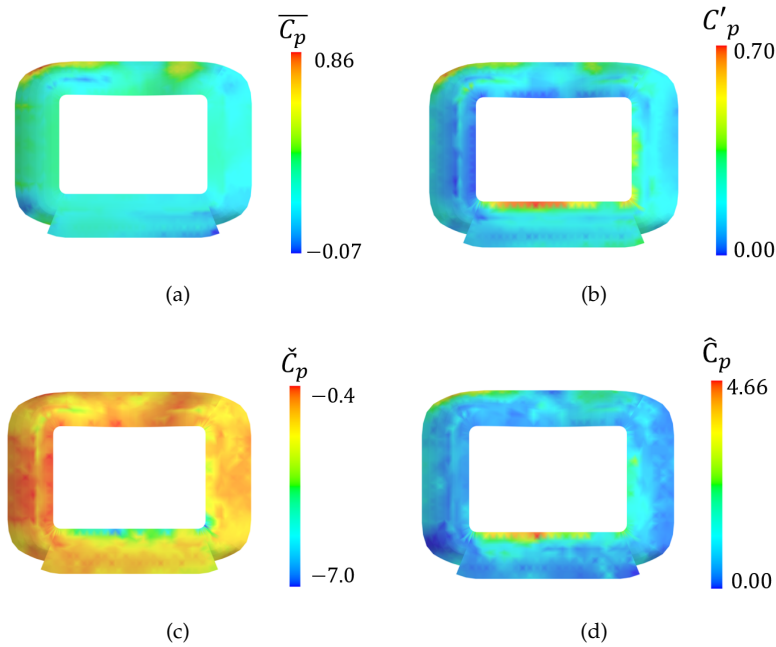


Fig. 4.13. The surface distribution of C_p statistics: (a) \bar{C}_p , (b) C'_p , (c) unfiltered recorded minima (\check{C}_p) and (d) unfiltered recorded maxima (\hat{C}_p).

4.4 Characterization of the structural response

In this section, we provide a description of the model used to evaluate the wind action over the roof. In particular, in Sec. 4.4.1, the mechanical behaviour of the structure is characterized by means of classical structural modes, complemented by the recently proposed Proper Skin Modes (PSMs). Then, in Sec. 4.4.2, we investigate the sensitivity of the results on the extreme value extraction method and the damping ratio (ζ). Finally, the extraction of ESWLs is discussed in Sec. 4.4.3.

4.4.1 Mechanical model

Characterizing the structural response with the purpose of assessing wind loading is relatively straightforward for simple idealized cases but it becomes often cumbersome in applications. The problem lies in the fact that the calculation of the structural response to wind excitation is usually performed by wind engineers outside the structural model software used by the designer. It is thus necessary to build a Reduced Order Model, ROM, of the structure in such a way that the required information can be easily extracted by general purpose commercial softwares, minimizing the overhead on the structural designer required to complete the task, e.g. the use of influence coefficients based on the application of punctual unit forces is theoretically simple but extremely impractical in practice. The procedure should be also conceived in order to be robust against gross human errors, which in the authors experience are extremely probable when reorganizing large datasets as required in this case.

In order to solve the problem, the authors devised a methodology based on the method of static corrections [159]. In particular, the ROM is built starting from usual structural modes, which are then complemented by Proper Skin Modes, PSMs. Such PSMs can be seen as a generalization of well-known influence coefficients based on the application of unitary forces, and actually, can be seen as their modal counterpart. We do not go into details here and interested readers are invited to refer to [159]. Nevertheless, the basic idea is that the structural response is calculated, as usual, in the modal base and static corrections are used to alleviate inaccuracies introduced by its truncation. Such static corrections are calculated by means of PSMs, which depend only on the surface geometry and can be easily calculated as the eigenvectors of a Laplacian operator discretized over the surfaces exposed to the wind action. This has also the positive effect to provide a robust way to check the model results: the response with and without static corrections shall be very similar.

An overview of the structural mode shapes is provided in Fig. 4.14 (only the ones relevant for wind loading are shown). It can be clearly seen that the mode shapes cannot be easily subdivided into global ones (affecting large

4.4. Characterization of the structural response

parts of the structure and mainly the primary structural system) and local ones (affecting small parts of the structure and mainly the secondary structural system). The situation is further complicated by the fact that the original structural model includes very massive parts as grandstands and surrounding walls, which tend to make the modes extraction difficult. Ideally, for the purpose of studying the roof dynamics, it would be advisable to develop a model comprising only the roof and modelling the lower parts with restraints, fixing also all local vibration modes. This nevertheless adds remarkable overheads on the structural designer and decreases inter-operability. We thus decided to consider 100 modes, but even with such a large number, in this case it is difficult to assess the consequences of adopting a truncated modal base.

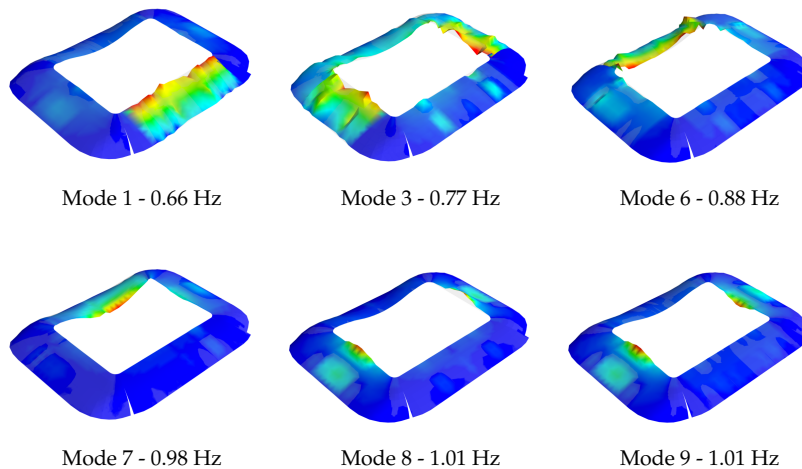


Fig. 4.14. Overview of the first ten structural modes, only those potentially relevant to wind loading are reported. (Colorbar not reported as the structural modes are not defined in amplitude.) (For interpretation of the references to color in this figure legend, the reader is referred to the web version of this article.)

We thus proceed at applying the approach proposed in [159], based on quasi-static corrections calculated from PSMs. In particular, the structural designer

already subdivided the roof in four macro-areas. Five PSMs are extracted separately for each of them, as shown in Fig. 4.15. As it can be seen, the first PSM is always a constant, so taking into account for a uniform pressure distribution. Higher PSMs are naturally ordered by decreasing wavelength, so hierarchically subdividing the pressure field in components mainly affecting the global response first, and the local response as the number of considered modes is increased. In this case, as we mainly investigate the global structural response, we consider only a few modes (5 for each roof sector, 20 in total) as the fifth PSM mode is the first one accounting for pressure variations from the outer to the inner ring (see Fig. 4.15 (c) and (f)). In practice, the procedure simply requires to transmit to the structural designer the 20 load distributions corresponding to the PSMs as nodal forces, run for each a static analysis and collect the results in terms of axial forces and bending moments and, eventually, displacements. The procedure is extremely efficient both in terms of computational time and work needed to extract the necessary information from the structural model, and can be applied to arbitrary complex structures.

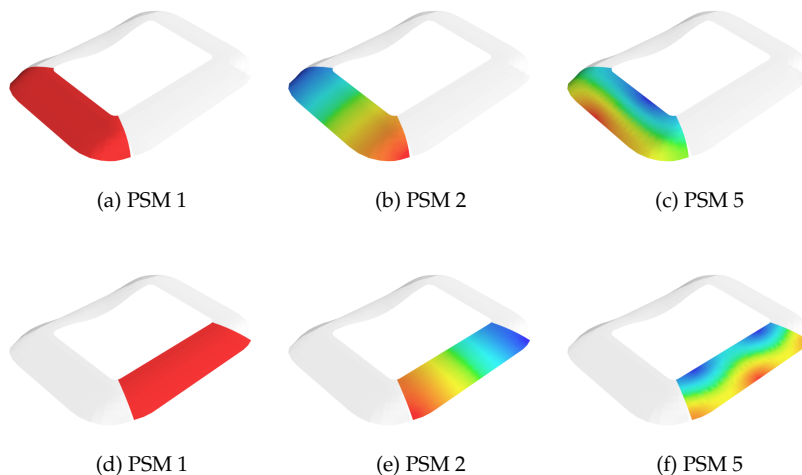


Fig. 4.15. Proper Skin Modes used in the structural response calculation: (a), (b) and (c) for the stadium curve and (d), (e) and (f) for the tribune.

Analyses made with and without static corrections, not here reported for the sake of conciseness, yield very similar results, so confirming that the model is correctly built and that the considered 100 modes allow for a good representation of the structural behaviour.

4.4.2 Sensitivity studies

Once the ROM for the structural response calculation is set up, it is possible to conduct structural analyses for each angle of attack and extract design envelopes (collecting for each member the design values of normal forces and bending moments).

Before proceeding, we deem important to assess the sensitivity of the model to two aspects/parameters which affect the analyses: the peak value extraction method and the adopted structural damping.

With respect to the first aspect, the same difficulties found for the local peak pressures arise here: the simulated time series are representative of 10 min real scale, so that only one 10 min return period extreme value can be extracted. Following the well-known Cook and Mayne approach [114], we target 80% quantiles. Those are estimated assuming a Gumbel distribution for the 2 min extremes and extrapolating the 10 min extremes by shifting it [113]. The approach is rigorously valid if the assumed Gumbel distribution is well-representative of the 2 min extremes, but this is not necessarily the case. Also, by proceeding in this way, only 5 samples are available to estimate the distribution parameters, which potentially leaves space for statistical fluctuations. In order to have a simple check on the results obtained in this way, we firstly compare these results with the extremes actually observed in the time series. In particular, Fig. 4.16 and 4.17 show the scatter plot of the extreme values obtained with the two aforementioned methods, for axial forces and bending moments, respectively (for all structural members). In such figures, results directly observed in the time series are reported in abscissa (denoted as *MinMax*), while in ordinates the extreme obtained using Gumbel approach are shown. The correlation between the two results appears to be very good,

with Gumbel approach providing on average slightly larger extremes, as expected (due to the fact that 80% non-exceedance probability was selected instead of 50%). This simple investigation cannot eliminate the opportunity to use longer time series to estimate quantiles (as usually done in WTT), but confirms that for early design stages, such aspect might be disregarded. From here on we thus proceed with the Gumbel approach.

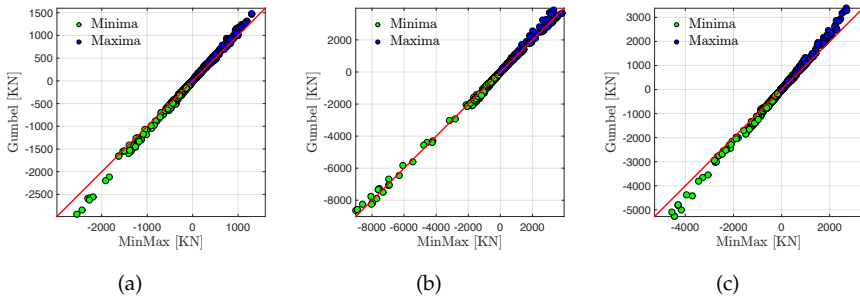


Fig. 4.16. Comparison between extreme values obtained using MinMax and Gumbel approach for axial forces: (a) 0° , (b) 60° and (c) 120° .

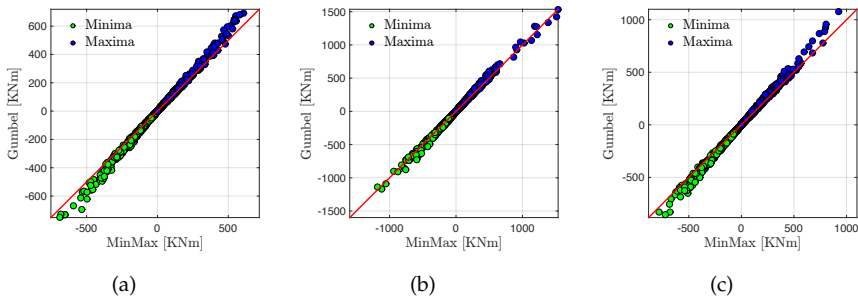


Fig. 4.17. Comparison between extreme values obtained using MinMax and Gumbel approach for bending moments: (a) 0° , (b) 60° and (c) 120° .

Once the extreme value extraction method is defined, it is necessary to carefully assess the effect of damping [166, 167], which is notoriously difficult to be evaluated *a priori*, also due to the presence of aerodynamic damping. Fig.

4.4. Characterization of the structural response

4.18 and 4.19 show the scatter plots between the design values (for each structural member) obtained with ζ , the damping ratio, equal to 0.01 and the corresponding values obtained with $\zeta = 0.02$ and $\zeta = 0.04$ (for all structural modes). The effect of ζ on the axial forces appears to be quite limited, while a deeper effect can be observed for bending moments. When ζ increases from 0.01 to 0.04, the peak axial forces decrease by about 37.5% for 60° and 25.0% for 120° , and the peak bending moments decrease about 50% for both cases. Such evaluations, although preliminary, can be used in order to quantify the potential benefits obtainable from an explicitly dedicated in-depth study and/or the installation of appropriate damping devices. Aiming at obtaining results on the safe side, $\zeta = 0.01$ is adopted in the following.

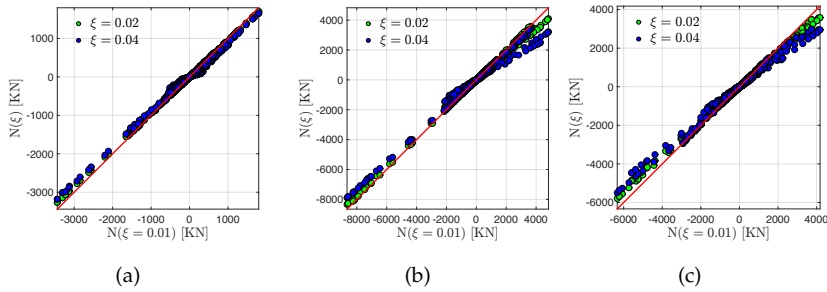


Fig. 4.18. Comparison between extreme axial forces obtained with different damping ratios: (a) 0° , (b) 60° and (c) 120° .

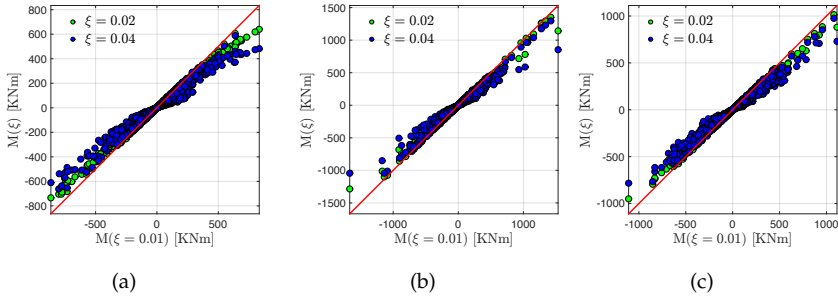


Fig. 4.19. Comparison between extreme bending moments obtained with different damping ratios: (a) 0° , (b) 60° and (c) 120° .

4.4.3 Design envelopes

We are now in the position to calculate the design values for each attack angle and, thus, the design envelopes. In this context it is useful to firstly consider the response obtained by making different hypotheses for the structural response calculation. In particular, Fig. 4.20 (axial forces) and Fig. 4.21 (bending moments) show the design envelopes obtained for different attack angles, considering the static (only time-averaged pressure field applied), the quasi-static (dynamic amplification factor always equal to unity) and the dynamic structural response. The abscissa reports the structural element ID and the ordinate the calculated extreme values. Actually, for the sake of readability, only a part of the envelope is shown, with element ID ranging from 1950 to 2100, being the other parts of the envelope qualitatively similar. It can be seen that for many elements the static response is small, the quasi-static response counts for approximately half the dynamic response, being the other half provided by dynamic amplification. The quasi-static contribution can be substantially regarded as the limit case obtained for high damping levels, so that the potential benefits obtainable by refining the damping specification or installing damping devices can be evaluated for each structural element.

4.4. Characterization of the structural response

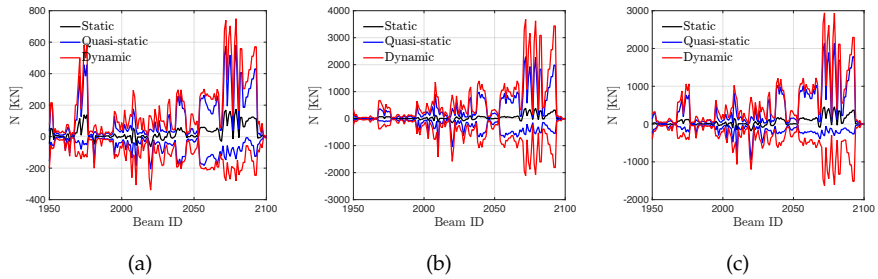


Fig. 4.20. Comparison between design envelopes for axial forces obtained from the static, quasi-static and dynamic components of the structure response: (a) 0° , (b) 60° and (c) 120° .

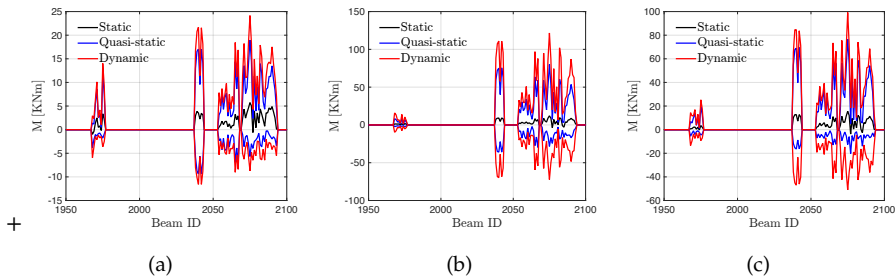


Fig. 4.21. Comparison between design envelopes for bending moments obtained from the static, quasi-static and dynamic components of the structure response: (a) 0° , (b) 60° and (c) 120° .

Finally, the envelope obtained by considering all attack angles with full dynamic analyses is reported in Fig. 4.22.

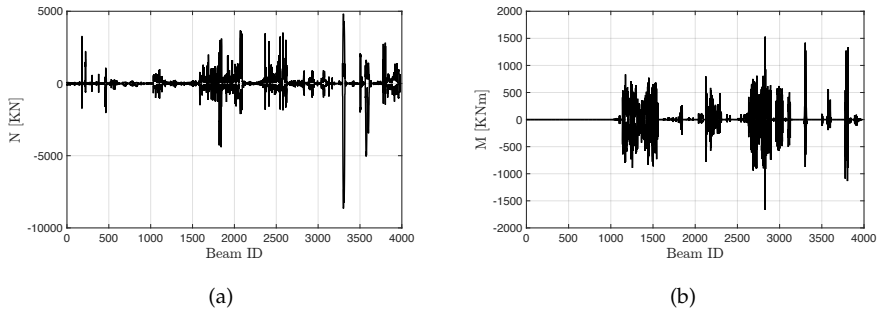


Fig. 4.22. Design envelopes for all structural members considering all wind directions: (a) axial forces and (b) bending moments.

Figure 4.23 reports the percentage of elements which attain the extreme value (maximum and minimum) for each angle of attack. In other words, for each structural element, we individuate the wind angle of attack which yielded the design value. Notice that the two curves are similar, as expected, due to the fact that the response is oscillatory but they are not identical due to the time-average contribution and the dissymmetry (up-lifting and down-pushing) of the wind excitation. Clearly for both, axial forces and bending moments (Fig. 4.23 (a) and (b), respectively), there is a preferential direction along 60° and 240° which is responsible for the dimensioning of the majority of the structural elements, together contributing for approximately 40% of the design values. This again confirms that skew angles are the ones which lead to the most severe effects on the structure.

4.4. Characterization of the structural response

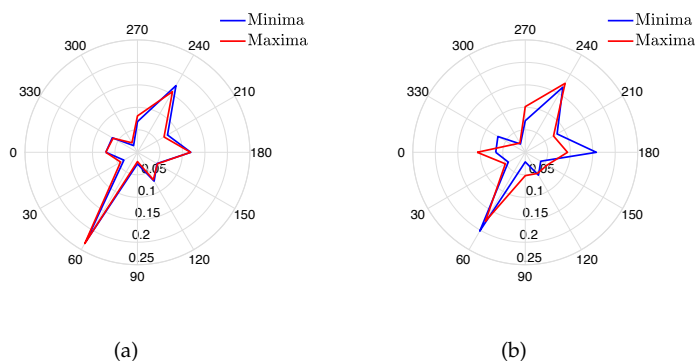


Fig. 4.23. Percentage of structural elements attaining their design value of axial forces (a) and bending moments (b).

As a last step, we show the results obtained when converting the design envelopes in ESWLs. The procedure used to perform such passage are detailed in [160] and we here report in Appendix A.3 only a very brief summary, useful to detail a slight modification here made to ameliorate the previously presented procedure.

Figure 4.24 reports the scatter plot between the design values calculated from dynamic analyses and those obtained from the application of ESWLs for axial forces. In particular, Fig. 4.24 (a), (b) and (c) show the results obtained using 3, 6 and 9 ESWLs respectively. Given the very good matching (results lying on the bisector) already obtained with 3 ESWLs, it means that the structural designer can safely design the main structure, which is composed mainly of truss elements, simply enveloping three static load conditions.

Unfortunately, in the case of the bending moments, which mainly compose the secondary structures, results appear less accurate, see Fig. 4.25. This is probably due to the more localized behaviour of the response, i.e. the secondary structures attain extreme values due to high/low pressure acting on smaller areas compared to the primary structural system. A higher number of PSMs might be considered to ameliorate results, if needed. In fact, we recall that PSMs are naturally ordered in such a way to firstly reconstruct the

most uniform pressure distributions, mainly affecting the primary structural system, and then progressively take into account local features of the pressure field, mainly relevant for secondary structural systems.

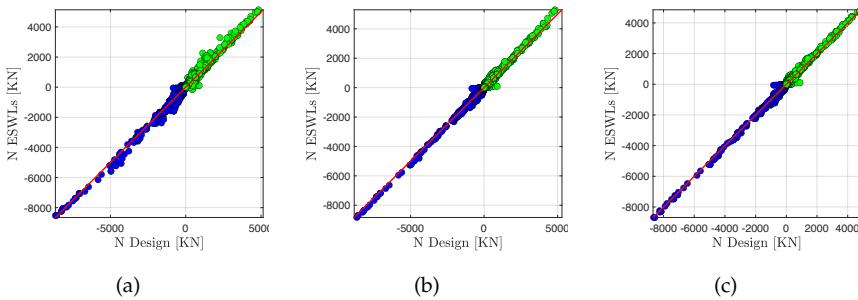


Fig. 4.24. Comparison between the design envelope for axial forces and values obtained from ESWLs: (a) 3 ESWLs, (b) 6 ESWLs and (c) 9 ESWLs.

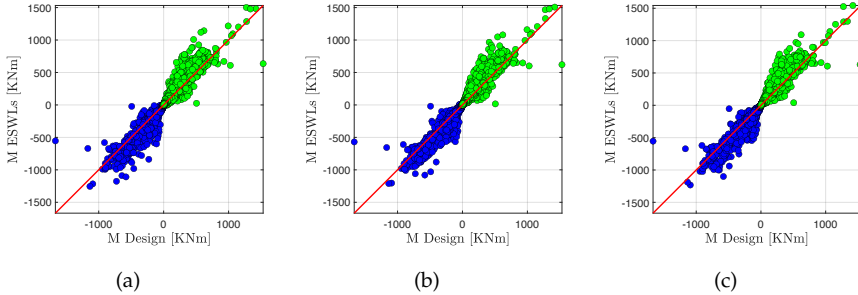


Fig. 4.25. Comparison between the design envelope for the bending moments and values obtained from ESWLs: (a) 3 ESWLs, (b) 6 ESWLs and (c) 9 ESWLs.

4.5 Conclusions

In this paper, we presented the preliminary analyses used to study the response of the new Bologna Stadium roof, taken as emblematic of a complex structure which might benefit from preliminary simulations to assess the effects induced by wind loading excitation. The analyses, run in the early stages

4.5. Conclusions

of the design process and prior to WTT, have been used to provide a first estimate of design values and, more importantly, to inform the subsequent steps of the design development.

In analogy to traditional experimental techniques, the study required the reconstruction of the stadium surroundings and the simulation of the wind flow has been obtained by means of LES. In order to obtain useful information for later design stages, the structural response has been calculated for all angles of attack and ESWLs extracted.

We individuate as key aspects which can benefit from an early assessment during the design process:

1. the expected effects/difficulties introduced by the presence of complex surroundings;
2. approximate individuation of regions characterized by high peak pressures;
3. the sensitivity to structural damping;
4. the evaluation of the relative importance of static, quasi-static and dynamic responses;
5. the individuation of wind directions which lead to stronger effects on the structures.

Thanks to such evaluations, it is possible to proceed to the final design with much deeper confidence regarding the absence of potentially unexpected behaviours and support decision regarding the most promising modifications and in-depth studies which might be undertaken to mitigate the wind-induced response.

5 Conclusions

The present thesis analyses three cases to assess the viability of LES for wind loading assessment for complex structures. A brief summary and the conclusions obtained for each case are given below.

5.1 Simulation of an isolated prism in ABL flow

In this case, LES is used to simulate wind fields around an isolated high-rise building model with an aspect ratio of 1:3:5, standing in ABL flow. Seven wind attack angles from 0° to 90° with an increment of 15° are simulated. The numerical results are validated with experimental results in terms of C_p statistics and global forces.

Globally, LES is capable of predicting the mean and maximum pressure on the building under both perpendicular and skew wind attack angles. Moreover, the evaluation of the global forces (moments) are quite satisfactory. However, the numerical accuracy in terms of root mean square and minimum pressure is poor. For a skew angle of attack, 45° , LES probably failed to capture the flow structures corresponding to the flow separations around the leading edges, showing less agreement of C_p' and minimum C_p with the experimental tests. Furthermore, the studies showed that the prediction errors are neither sensitive to the addition of boundary layer cells for the near-wall treatment nor to the adopted SGS turbulence models.

5.2 Wind loads prediction for the Torre Gioia 22

In this case, the recently designed Torre Gioia 22 has been simulated and the wind loads on it have been evaluated. Six wind attack angles, each 60° from 0° to 300° are simulated. The LES results are validated with wind tunnel tests results and good agreements in terms of C_p statistics and global forces are obtained.

A good balance between numerical cost and accuracy has been obtained considering the following aspects:

- The mesh size adopted in the proximity of the structures is 0.01 and 0.005 time of building height for the main surfaces and geometrical details, respectively.
- The partially-corrected schemes, although are sub-optimal in terms of numerical accuracy, can be adopted for stabilizing the calculations.
- No boundary layer cells are used near the building surfaces, also, avoiding huge amount of computational grids, whose role is often unclear for bluff-body aerodynamics.

The computational costs of the simulations are analyzed and compared with the wind tunnel tests. The results indicate that the cost of running accurate numerical simulations is still comparable, if not higher, than wind tunnel tests. This is particularly true in the case of complex surroundings or multiple design scenarios. However, the use of numerical simulations appears to be already well-suited for cases in which it is possible to define *a priori* a limited number of conditions to be tested.

5.3 Early stages wind load assessment for the new Bologna Stadium roof

In this case, the new large-span roof over the Bologna Stadium is simulated and analyzed. The wind forces on it and the structural response to wind actions are studied based on the simulation results. It is a LES performed in the

5.3. Early stages wind load assessment for the new Bologna Stadium roof

early design stages before the traditional wind tunnel tests, aiming at providing a preliminary estimation of design values and informing the subsequent steps of the design development.

Firstly, the critical wind effects are individuated, including the high peak pressure distribution, the potential effects introduced by the presence of complex surroundings and the wind direction leading to stronger effects. Regarding the structural responses, the relative importance of static, quasi-static and dynamic responses are evaluated. In addition, the sensitivity to structural damping is analyzed.

Although based on the numerical results without experimental validation, these preliminary evaluations can effectively inform later investigations and provide the final design processes with deeper confidence regarding the absence of potentially unexpected behaviours. Such preliminary analyses can support decisions regarding the most promising modifications and in-depth studies which might be undertaken to mitigate the wind-induced response.

A Appendix

A.1 PRFG³

As anticipated the generation of inflow conditions has been the object of numerous research works in recent years and the topic is still attracting the attention of the research community. In particular, the time-varying velocity field applied at the inflow patch must be characterized by statistics compatible with those expected on-site. It is usually assumed that turbulence intensities (one for each velocity component), time-spectra (one for each velocity component) and integral length scales (in general nine of them, three for each velocity component corresponding to the three spatial directions) provide a suitable characterization of the wind field for the purpose of wind loading evaluation.

Different synthetic turbulence generation methods often take different perspectives with respect to what target values should be adopted, although some choices can be easily shown to be equivalent. Additionally, it must be considered that the generated field must be correctly propagated inside the computational domain. Such last requirement can be fulfilled by generating velocity fields which approximate mass and momentum conservation (i.e. the divergence-free condition and Taylor assumption). Another requirement is that the generation of inflow conditions should not sensibly increment the simulation time.

With reference to the notation introduced in Sec. 3.4.5, within techniques of type SA, we find the full simulation of the wind tunnel arrangement and recycling methods. The use of experimental data does not require numerical simulations but it is qualitatively affine to such category. The fulfilling of

Navier-Stokes equations is in this case automatic. The approach is cumbersome from the computational point of view, although the incoming flow can be generated once and then used for all attack angles and cases characterized by the same ABL type. The control of the statistics of the generated ABL is not trivial, analogously to the disposition of roughness blocks and spires for wind tunnel tests. After calibration results are generally well satisfactory.

The category SGwo groups the majority of available synthetic turbulence generation methods. Such methods focus on the generation of synthetic flows characterized by target statistics (to be interpreted in a vast sense including time-spectra, two-point statistics, etc). The implicit assumption underlying such methods is that the synthetic field will be transmitted inside the computational domain without undergoing major modifications in order to impose the fulfillment of Navier-Stokes equations.

Historically, methods which assemble the synthetic field as a superposition of coherent structures privileged the fulfilling of Taylor assumption while methods based on Fourier synthesis privileged the fulfillment of the divergence-free conditions. The implications of such choices have been studied in detail in [110] for the case of a single velocity-wave, showing that only considering at the same time mass and momentum conservation (although linearized) allows a correct transmission of the synthetic field through the inflow patch. If the synthetic flow is built without taking such aspects into account, modifications of the velocity field at short distance from the inflow patch should be expected. Such modifications are operated by the pressure field, so leading to nonphysical pressure fluctuations. It shall be remarked that, despite pressure fluctuations, which are further commented in Appendix A.2, the results from these methods can be satisfactory as corrections might sometimes be small and/or do not sensibly alter the inflow characteristics. Despite the discrepancies between the targeted and the velocity fields actually transmitted through the inflow patch, good results can be often obtained after appropriate calibration.

As described above, it is convenient to generate synthetic fields characterized by both target statistical quantities and appropriate differential properties (i.e.

fulfilling *a priori* approximated versions of the Navier-Stokes equations). This is required in order to allow the field to be transmitted through the inflow patch without undergoing modifications (at least with good approximation). This led to the development of SG methods. In particular, to the authors knowledge, three of the available synthetic turbulence generation methods respect both divergence-free condition and Taylor assumption *a priori*. Two are based on the assembling of coherent structures, the DFSEM and TS methods while one, denoted as PRFG³, proceeds by spectral synthesis. The three methods slightly differ in the specification of the target values with DFSEM and TS privileging control over the Reynolds stress tensor and PRFG³ privileging integral length scales.

We would like to stress again that the topic is still the object of numerous researches and that acceptable results can be obtained with many of the techniques available in the literature, although for some of them an iterative optimization of the target values used for the inflow generation is necessary.

A.2 VBIC

As previously discussed, the synthetic field might (i.e. SA) or might not (i.e. SGwo) approximate Navier-Stokes equations, depending on the adopted turbulence generation method. As anticipated, in the second case pressure fluctuations should be expected. Actually, it must be noticed that synthetic flows generally do not take into account the presence of BCs confining with the inflow patch. Such BCs require the modification of the synthetic field in the proximity of the boundaries and, thus, lead to the insurgence of pressure fluctuations in their proximity even for SG inflows. It thus appears that some nonphysical pressure fluctuations should be expected with all turbulence generation methods when the synthetic field is applied as a Dirichlet condition at the inflow. It must be also noticed that SA methods do not show such difficulties as the field imposed at the inflow is extracted from a numerical simulation which enforces Navier-Stokes and BCs.

The problem can be tackled in three different ways (here it is assumed that

strong global jumps in pressure provided by global mass imbalances are prevented ensuring a constant global mass-flux through the inflow patch). Firstly, it is possible to avoid the problem simply moving the target building sufficiently far from the inflow [83]. The second possibility is to apply velocity at cell centres in a plane located slightly downstream the inflow patch in the predictor step of the pressure-velocity coupling algorithm [168]. Recently, a procedure able to allow to impose the synthetic field at the inflow patch as a standard Dirichlet BC without causing nonphysical pressure fluctuations has been proposed in [34]. The method, denoted as VBIC, allows to correct the synthetic inflow enforcing the divergence-free condition and accounting for the presence of BCs. The corrections are built in order to be of minimal norm over the inflow patch.

A.3 ESWL

The procedure used to perform such passage are detailed in [160] and we here report only a very brief summary, useful to detail a slight modification made to ameliorate the previously presented procedure. The interested reader is invited to refer to the original paper for details.

In short, Equivalent Static Wind Loads (ESWLs) are built as combinations of Proper Skin Modes (PSMs) which, once enveloped, reconstruct the design values. Taking as example the upper envelope, i.e. the maxima, the problem can be thus stated as

$$\mathbf{E}^{rec} = \mathbf{max}(\mathbf{E}^{psm}\mathbf{W}) = \mathbf{max}(\mathbf{E}^{eswl}) \approx \mathbf{E}^{env}, \quad (\text{A.1})$$

where \mathbf{E}^{env} is a vector which collects the extreme effects (e.g. axial forces and bending moments) for all the elements accounting for all attack angles obtained from dynamic analyses, \mathbf{E}^{psm} are the effects induced by the PSMs, \mathbf{W} is an unknown matrix of weighting coefficients to be determined and \mathbf{E}^{rec} is the envelope reconstruction obtained from the ESWLs [169].

The identification of the matrix \mathbf{W} which minimizes the difference between \mathbf{E}^{env} and \mathbf{E}^{rec} amounts to the determination of the ESWLs. It can be thus

A.3. ESWL

written that \mathbf{W} is the matrix which minimizes the target function F_{max} with

$$F_{max} = ||E^{env} - E^{rec}||^2 = ||E^{env} - \mathbf{max}(E^{psm}\mathbf{W})||^2. \quad (\text{A.2})$$

Bibliography

- [1] John D Holmes. *Wind loading of structures*. CRC press, 2007.
- [2] N.L. Panwar, S.C. Kaushik, and Surendra Kothari. "Role of renewable energy sources in environmental protection: A review". In: *Renewable and Sustainable Energy Reviews* 15.3 (2011), pp. 1513–1524.
- [3] Wikipedia contributors. *Wind turbine — Wikipedia, The Free Encyclopedia*. [Online; accessed 7-November-2022]. 2022.
- [4] Wikipedia contributors. *Tacoma Narrows Bridge (1940) — Wikipedia, The Free Encyclopedia*. [Online; accessed 7-November-2022]. 2022.
- [5] Alan G Davenport. "Past, present and future of wind engineering". In: *Journal of Wind Engineering and Industrial Aerodynamics* 90.12-15 (2002), pp. 1371–1380.
- [6] G. Eiffel. "The Eiffel Tower". In: *The New review* 1.2 (July 1889). Last updated - 2010-07-20, pp. 172–181.
- [7] Bruno Chanetz. "A century of wind tunnels since Eiffel". In: *Comptes Rendus Mécanique* 345.8 (2017), pp. 581–594.
- [8] J. E. Cermak. "Applications of Fluid Mechanics to Wind Engineering—A Freeman Scholar Lecture". In: *Journal of Fluids Engineering* 97.1 (Mar. 1975), pp. 9–38.
- [9] Alan G Davenport. "The application of statistical concepts to the wind loading of structures." In: *Proceedings of the Institution of Civil Engineers* 19.4 (1961), pp. 449–472.
- [10] Nicholas Isyumov. "Alan G. Davenport's mark on wind engineering". In: *Journal of Wind Engineering and Industrial Aerodynamics* 104-106 (2012). 13th International Conference on Wind Engineering, pp. 12–24.
- [11] Giovanni Solari. "Wind Loading of Structures: Framework, Phenomena, Tools and Codification". In: *Structures* 12 (2017), pp. 265–285.

-
- [12] Nicholas John Cook. "Review of errors in archived wind data". In: *Weather* 69.3 (2014), pp. 72–78.
- [13] J. Wieringa. "Description requirements for assessment of non-ideal wind stations — for example Aachen." In: *Journal of Wind Engineering and Industrial Aerodynamics* 11.1 (1983), pp. 121–131.
- [14] Christopher Jung and Dirk Schindler. "Changing wind speed distributions under future global climate". In: *Energy Conversion and Management* 198 (2019), p. 111841. ISSN: 0196-8904.
- [15] J.R. Mayne. "The estimation of extreme winds". In: *Journal of Wind Engineering and Industrial Aerodynamics* 5.1 (1979), pp. 109–137.
- [16] Alessio Torrielli, Maria Pia Repetto, and Giovanni Solari. "Extreme wind speeds from long-term synthetic records". In: *Journal of Wind Engineering and Industrial Aerodynamics* 115 (2013), pp. 22–38.
- [17] Christopher Jung and Dirk Schindler. "Wind speed distribution selection – A review of recent development and progress". In: *Renewable and Sustainable Energy Reviews* 114 (2019), p. 109290.
- [18] Alan G Davenport. "Rationale for Determining Design Wind Velocities". In: *Journal of the Structural Division* 86.5 (1960), pp. 39–68.
- [19] Jacques Biétry, Christian Sacré, and Emil Simiu. "Mean Wind Profiles and Change of Terrain Roughness". In: *Journal of the Structural Division* 104.10 (1978), pp. 1585–1593.
- [20] D.M. Deaves. "Computations of wind flow over changes in surface roughness". In: *Journal of Wind Engineering and Industrial Aerodynamics* 7.1 (1981), pp. 65–94.
- [21] Robert N. Meroney. "Wind-tunnel simulation of the flow over hills and complex terrain". In: *Journal of Wind Engineering and Industrial Aerodynamics* 5.3 (1980). *Wind Energy Conversion Systems*, pp. 297–321.
- [22] G. T. Bitsuamlak, T. Stathopoulos, and C. Bédard. "Numerical Evaluation of Wind Flow over Complex Terrain: Review". In: *Journal of Aerospace Engineering* 17.4 (2004), pp. 135–145.
- [23] John C Wyngaard. *Turbulence in the Atmosphere*. Cambridge University Press, 2010.

- [24] J. Armit and J. Counihan. "The simulation of the atmospheric boundary layer in a wind tunnel". In: *Atmospheric Environment* (1967) 2.1 (1968), pp. 49–71.
- [25] P.W. Bearman and T. Morel. "Effect of free stream turbulence on the flow around bluff bodies". In: *Progress in Aerospace Sciences* 20.2 (1983), pp. 97–123.
- [26] QS Li and WH Melbourne. "An experimental investigation of the effects of free-stream turbulence on streamwise surface pressures in separated and reattaching flows". In: *Journal of wind engineering and industrial aerodynamics* 54 (1995), pp. 313–323.
- [27] R. Hillier and N.J. Cherry. "The effects of stream turbulence on separation bubbles". In: *Journal of Wind Engineering and Industrial Aerodynamics* 8.1 (1981), pp. 49–58.
- [28] Fred L. Haan, Ahsan Kareem, and Albin A. Szewczyk. "The effects of turbulence on the pressure distribution around a rectangular prism". In: *Journal of Wind Engineering and Industrial Aerodynamics* 77-78 (1998), pp. 381–392.
- [29] M. Kiya and K. Sasaki. "Free-stream turbulence effects on a separation bubble". In: *Journal of Wind Engineering and Industrial Aerodynamics* 14.1 (1983), pp. 375–386.
- [30] Yue Zhang, Wagdi G. Habashi, and Rooh A. Khurram. "Predicting wind-induced vibrations of high-rise buildings using unsteady CFD and modal analysis". In: *Journal of Wind Engineering and Industrial Aerodynamics* 136 (2015), pp. 165–179.
- [31] Giacomo Lamberti and Catherine Gorlé. "Sensitivity of LES predictions of wind loading on a high-rise building to the inflow boundary condition". In: *Journal of Wind Engineering and Industrial Aerodynamics* 206 (2020), p. 104370.
- [32] Aly Mousaad Aly. "Atmospheric boundary-layer simulation for the built environment: Past, present and future". In: *Building and Environment* 75 (2014), pp. 206–221.
- [33] L. Patruno and M. Ricci. "A systematic approach to the generation of synthetic turbulence using spectral methods". In: *Computer Methods in Applied Mechanics and Engineering* 340 (2018), pp. 881–904.

-
- [34] L. Patruno and S. de Miranda. "Unsteady inflow conditions: A variationally based solution to the insurgence of pressure fluctuations". In: *Computer Methods in Applied Mechanics and Engineering* 363 (2020), p. 112894.
- [35] Y Nakamura. "Bluff-body aerodynamics and turbulence". In: *Journal of Wind Engineering and Industrial Aerodynamics* 49.1-3 (1993), pp. 65–78.
- [36] WH Melbourne et al. "Turbulence, bluff body aerodynamics and wind engineering". In: *Proceedings of the 7th Australasian hydraulics and fluid mechanics conference, Brisbane*. 1980.
- [37] K.C.S. Kwok. "Effect of building shape on wind-induced response of tall building". In: *Journal of Wind Engineering and Industrial Aerodynamics* 28.1 (1988), pp. 381–390.
- [38] Luigi Carassale, Andrea Freda, and Michela Marrè-Brunenghi. "Experimental investigation on the aerodynamic behavior of square cylinders with rounded corners". In: *Journal of Fluids and Structures* 44 (2014), pp. 195–204.
- [39] H. Tanaka and N. Lawen. "Test on the CAARC standard tall building model with a length scale of 1 : 1000". In: *Journal of Wind Engineering and Industrial Aerodynamics* 25.1 (1986), pp. 15–29.
- [40] Yukio Tamura. "Application of damping devices to suppress wind-induced responses of buildings". In: *Journal of Wind Engineering and Industrial Aerodynamics* 74-76 (1998), pp. 49–72.
- [41] Yukio Tamura et al. "Effectiveness of tuned liquid dampers under wind excitation". In: *Engineering Structures* 17.9 (1995). Auxiliary damping systems for mitigation of wind-induced vibration, pp. 609–621.
- [42] G. Piccardo and G. Solari. "Closed form prediction of 3-D wind-excited response of slender structures". In: *Journal of Wind Engineering and Industrial Aerodynamics* 74-76 (1998), pp. 697–708.
- [43] Maria Pia Repetto and Giovanni Solari. "Equivalent static wind actions on vertical structures". In: *Journal of Wind Engineering and Industrial Aerodynamics* 92.5 (2004), pp. 335–357.

- [44] A.W. Irwin. "Perception, comfort and performance criteria for human beings exposed to whole body pure yaw vibration and vibration containing yaw and translational components". In: *Journal of Sound and Vibration* 76.4 (1981), pp. 481–497.
- [45] A.P. Jeary, R.G. Morris, and R.W. Tomlinson. "Perception of vibration - Tests in a tall building". In: *Advances in Wind Engineering*. Amsterdam: Elsevier, 1988, pp. 361–370.
- [46] Alan G Davenport. "An approach to human comfort criteria for environmental wind conditions". In: *Colloquium on building climatology*. 1972.
- [47] W.A. Dalgliesh. "Comparison of model/full-scale wind pressures on a high-rise building". In: *Journal of Wind Engineering and Industrial Aerodynamics* 1 (1975), pp. 55–66.
- [48] K.J. Eaton and J.R. Mayne. "The measurement of wind pressures on two-storey houses at Aylesbury". In: *Journal of Wind Engineering and Industrial Aerodynamics* 1 (1975), pp. 67–109.
- [49] Marc L. Levitan and Kishor C. Mehta. "Texas Tech field experiments for wind loads part 1: building and pressure measuring system". In: *Journal of Wind Engineering and Industrial Aerodynamics* 43.1 (1992). International Conference on Wind Engineering, pp. 1565–1576.
- [50] Marc L. Levitan and Kishor C. Mehta. "Texas tech field experiments for wind loads part II: meteorological instrumentation and terrain parameters". In: *Journal of Wind Engineering and Industrial Aerodynamics* 43.1 (1992). International Conference on Wind Engineering, pp. 1577–1588.
- [51] X. Zhaoa, J.M. Ding, and H.H. Suna. "Structural Design of Shanghai Tower for Wind Loads". In: *Procedia Engineering* 14 (2011). The Proceedings of the Twelfth East Asia-Pacific Conference on Structural Engineering and Construction, pp. 1759–1767.
- [52] Zhen Han et al. "Investigation of Wind-Loads Acting on Low-Aspect-Ratio Cylindrical Structures Based on a Wind Tunnel Test". In: *Applied Sciences* 12.12 (2022).

-
- [53] H. Bendjebbas, A. Abdellah-ElHadj, and M. Abbas. "Full-scale, wind tunnel and CFD analysis methods of wind loads on heliostats: A review". In: *Renewable and Sustainable Energy Reviews* 54 (2016), pp. 452–472.
- [54] Wei Hao, Kai Chen, and Yalin Yan. "Design wind loads for local flexible cladding of structures based on wind tunnel tests". In: *Journal of Building Engineering* 44 (2021), p. 103154.
- [55] Yuhang Li et al. "Comparative Studies of Computational Fluid Dynamic Geometric Models at Multiple Levels of Details in Evaluating Wind Action on Asian Ancient Wooden Tower". In: *International Journal of Architectural Heritage* 0.0 (2021), pp. 1–18.
- [56] A.D. Wnęk and C. Guedes Soares. "CFD assessment of the wind loads on an LNG carrier and floating platform models". In: *Ocean Engineering* 97 (2015), pp. 30–36.
- [57] Gregory A. Kopp, Murray J. Morrison, and David J. Henderson. "Full-scale testing of low-rise, residential buildings with realistic wind loads". In: *Journal of Wind Engineering and Industrial Aerodynamics* 104-106 (2012). 13th International Conference on Wind Engineering, pp. 25–39.
- [58] J.C. Li, S.Y. Hu, and Q.S. Li. "Comparative study of full-scale and model-scale wind pressure measurements on a gable roof low-rise building". In: *Journal of Wind Engineering and Industrial Aerodynamics* 208 (2021), p. 104448.
- [59] Q.S. Li et al. "Wind tunnel and full-scale study of wind effects on China's tallest building". In: *Engineering Structures* 28.12 (2006), pp. 1745–1758.
- [60] Jack E Cermak. "Wind tunnel for the study of turbulence in the atmospheric surface layer". PhD thesis. Colorado State University. Libraries, 1956.
- [61] Jack E Cermak. "Wind-tunnel development and trends in applications to civil engineering". In: *Journal of Wind Engineering and Industrial Aerodynamics* 91.3 (2003), pp. 355–370.
- [62] Sangie Zaitsoff, J Peter C King, and F Bartlett. "Nomination of boundary layer wind tunnel laboratory as a case/asce international historic site". In: *Building Tomorrow's Society* (2018).

- [63] Peter A. Irwin. "Bluff body aerodynamics in wind engineering". In: *Journal of Wind Engineering and Industrial Aerodynamics* 96.6 (2008). 5th International Colloquium on Bluff Body Aerodynamics and Applications, pp. 701–712.
- [64] J. Xie and P.A. Irwin. "Application of the force balance technique to a building complex". In: *Journal of Wind Engineering and Industrial Aerodynamics* 77-78 (1998), pp. 579–590.
- [65] T. Tschanz and A.G. Davenport. "The base balance technique for the determination of dynamic wind loads". In: *Journal of Wind Engineering and Industrial Aerodynamics* 13.1 (1983), pp. 429–439.
- [66] Peter A. Irwin. "Wind engineering challenges of the new generation of super-tall buildings". In: *Journal of Wind Engineering and Industrial Aerodynamics* 97.7 (2009). 12th International Conference on Wind Engineering, pp. 328–334.
- [67] J Xie and A To. "Design-oriented wind engineering studies for CCTV new building". In: *Proceedings of the Sixth Asia-Pacific Conference on Wind Engineering, Seoul, Korea*. 2005.
- [68] Slavica Ristić et al. "Review of methods for flow velocity measurement in wind tunnels". In: *Sci. Rev.* 54.3 (2004).
- [69] Justus GV van Ramshorst et al. "Wind speed measurements using distributed fiber optics: A windtunnel study". In: *Atmos. Meas. Tech. Discuss* 2019 (2019), pp. 1–21.
- [70] Hiroto Kataoka, Yoshiyuki Ono, and Kota Enoki. "Applications and prospects of CFD for wind engineering fields". In: *Journal of Wind Engineering and Industrial Aerodynamics* 205 (2020), p. 104310.
- [71] Jörg Franke. "Introduction to the Prediction of Wind Loads on Buildings by Computational Wind Engineering (CWE)". In: *Wind Effects on Buildings and Design of Wind-Sensitive Structures*. Ed. by Ted Stathopoulos and Charalambos C. Baniotopoulos. Vienna: Springer Vienna, 2007, pp. 67–103.
- [72] Douglas G Fox and Douglas K Lilly. "Numerical simulation of turbulent flows". In: *Reviews of Geophysics* 10.1 (1972), pp. 51–72.

-
- [73] Parviz Moin and Krishnan Mahesh. "Direct numerical simulation: a tool in turbulence research". In: *Annual review of fluid mechanics* 30.1 (1998), pp. 539–578.
- [74] Marcel Lesieur and Olivier Metais. "New trends in large-eddy simulations of turbulence". In: *Annual review of fluid mechanics* 28.1 (1996), pp. 45–82.
- [75] C G Speziale. "Analytical Methods for the Development of Reynolds-Stress Closures in Turbulence". In: *Annual Review of Fluid Mechanics* 23.1 (1991), pp. 107–157.
- [76] J. Smagorinsky. "General circulation experiments with the primitive equations: I. The Basic Experiment". In: *Monthly Weather Review* 91.3 (1963), pp. 99–164.
- [77] Franck Nicoud and Frédéric Ducros. "Subgrid-scale stress modelling based on the square of the velocity gradient tensor". In: *Flow, turbulence and Combustion* 62.3 (1999), pp. 183–200.
- [78] Stefan Heinz. "A review of hybrid RANS-LES methods for turbulent flows: Concepts and applications". In: *Progress in Aerospace Sciences* 114 (2020), p. 100597. ISSN: 0376-0421.
- [79] R. Yoshie et al. "Cooperative project for CFD prediction of pedestrian wind environment in the Architectural Institute of Japan". In: *Journal of Wind Engineering and Industrial Aerodynamics* 95.9 (2007), pp. 1551–1578.
- [80] Bert Blocken, WD Janssen, and Twan van Hooff. "CFD simulation for pedestrian wind comfort and wind safety in urban areas: General decision framework and case study for the Eindhoven University campus". In: *Environmental Modelling & Software* 30 (2012), pp. 15–34.
- [81] Shenghong Huang, QS Li, and Shengli Xu. "Numerical evaluation of wind effects on a tall steel building by CFD". In: *Journal of Constructional Steel Research* 63.5 (2007), pp. 612–627.
- [82] Alexander Michalski et al. "Computational wind engineering of large umbrella structures". In: *Journal of Wind Engineering and Industrial Aerodynamics* 144 (2015), pp. 96–107.
- [83] Marija Bervida and Luca Patruno. "Synthetic generation of the atmospheric boundary layer for wind loading assessment using spectral

- methods". In: *Journal of Wind Engineering and Industrial Aerodynamics* 196 (2020), p. 104040.
- [84] Yin Luo et al. "Large-eddy simulation evaluation of wind loads on a high-rise building based on the multiscale synthetic eddy method". In: *Advances in Structural Engineering* 22.4 (2019), pp. 997–1006.
- [85] Giulio Vita et al. "Effects of inflow condition on RANS and LES predictions of the flow around a high-rise building". In: *Fluids* 5.4 (2020), p. 233.
- [86] Guoyi Jiang and Ryuichiro Yoshie. "Side ratio effects on flow and pollutant dispersion around an isolated high-rise building in a turbulent boundary layer". In: *Building and Environment* 180 (2020), p. 107078.
- [87] Gongbo Zu and Kit Ming Lam. "LES and wind tunnel test of flow around two tall buildings in staggered arrangement". In: *Computation* 6.2 (2018), p. 28.
- [88] Yoshihide Tominaga et al. "Comparison of various revised $k\text{-}\epsilon$ models and LES applied to flow around a high-rise building model with 1: 1: 2 shape placed within the surface boundary layer". In: *Journal of Wind Engineering and Industrial Aerodynamics* 96.4 (2008), pp. 389–411.
- [89] GW Alminhana, AL Braun, and AM Loredou-Souza. "A numerical experimental investigation on the aerodynamic performance of CAARC building models with geometric modifications". In: *Journal of Wind Engineering and Industrial Aerodynamics* 180 (2018), pp. 34–48.
- [90] Jinyang Liu et al. "LES study of windward-face-mounted-ribs' effects on flow fields and aerodynamic forces on a square cylinder". In: *Building and Environment* 200 (2021), p. 107950.
- [91] Yuanlin Yu, Yi Yang, and Zhuangning Xie. "A new inflow turbulence generator for large eddy simulation evaluation of wind effects on a standard high-rise building". In: *Building and Environment* 138 (2018), pp. 300–313.
- [92] Elisa Buffa, Jérôme Jacob, and Pierre Sagaut. "Lattice-Boltzmann-based large-eddy simulation of high-rise building aerodynamics with inlet turbulence reconstruction". In: *Journal of Wind Engineering and Industrial Aerodynamics* 212 (2021), p. 104560.

-
- [93] Jianghua Ke. "RANS and hybrid LES/RANS simulations of flow over a square cylinder". In: *Advances in Aerodynamics* 1.1 (2019), pp. 1–24.
- [94] Bálint Papp, Gergely Kristóf, and Christof Gromke. "Application and assessment of a GPU-based LES method for predicting dynamic wind loads on buildings". In: *Journal of Wind Engineering and Industrial Aerodynamics* 217 (2021), p. 104739.
- [95] Marie Skytte Thordal et al. "Towards a standard CFD setup for wind load assessment of high-rise buildings: Part 1–Benchmark of the CAARC building". In: *Journal of Wind Engineering and Industrial Aerodynamics* 205 (2020), p. 104283.
- [96] Marie Skytte Thordal, Jens Chr Bennetsen, and H Holger H Koss. "Review for practical application of CFD for the determination of wind load on high-rise buildings". In: *Journal of Wind Engineering and Industrial Aerodynamics* 186 (2019), pp. 155–168.
- [97] Luca Bruno, Maria Vittoria Salvetti, and Francesco Ricciardelli. "Benchmark on the Aerodynamics of a Rectangular 5:1 Cylinder: An overview after the first four years of activity". In: *Journal of Wind Engineering and Industrial Aerodynamics* 126 (2014), pp. 87–106.
- [98] Yoshihide Tominaga et al. "AIJ guidelines for practical applications of CFD to pedestrian wind environment around buildings". In: *Journal of Wind Engineering and Industrial Aerodynamics* 96.10 (2008), pp. 1749–1761.
- [99] M Schatzmann, H Olesen, and J Franke. "COST 732 Model Evaluation Case Studies: Approach and Results (Hamburg)". In: (2010).
- [100] Romain Guichard. "Assessment of an improved random flow generation method to predict unsteady wind pressures on an isolated building using large-eddy simulation". In: *Journal of Wind Engineering and Industrial Aerodynamics* 189 (2019), pp. 304–313.
- [101] Wei Wang, Yong Cao, and Tsubasa Okaze. "Comparison of hexahedral, tetrahedral and polyhedral cells for reproducing the wind field around an isolated building by LES". In: *Building and Environment* 195 (2021), p. 107717.
- [102] K. Wijesooriya et al. "Numerical investigation of scale resolved turbulence models (LES, ELES and DDES) in the assessment of wind effects

- on supertall structures". In: *Journal of Building Engineering* 25 (2019), p. 100842.
- [103] Jianlin Liu et al. "LES for pedestrian level wind around an idealized building array—Assessment of sensitivity to influencing parameters". In: *Sustainable Cities and Society* 44 (2019), pp. 406–415.
- [104] Yong Wang and Xinzhong Chen. "Simulation of approaching boundary layer flow and wind loads on high-rise buildings by wall-modeled LES". In: *Journal of Wind Engineering and Industrial Aerodynamics* 207 (2020), p. 104410.
- [105] Yong Cao et al. "Investigation of local severe suction on the side walls of a high-rise building by standard, spectral and conditional POD". In: *Building and Environment* (2022), p. 109047.
- [106] M Ricci et al. "Towards LES as a design tool: Wind loads assessment on a high-rise building". In: *Journal of Wind Engineering and Industrial Aerodynamics* 180 (2018), pp. 1–18.
- [107] AIJ-RLB. *Recommendations for loads on buildings*. 2004.
- [108] TPU. *TPU Aerodynamic Database*. <http://wind.arch.t-kougei.ac.jp/system/eng/contents/code/tpu>. 2007.
- [109] Jörg Franke et al. "Best practice guideline for the CFD simulation of flows in the urban environment—a summary". In: *11th Conference on Harmonisation within Atmospheric Dispersion Modelling for Regulatory Purposes, Cambridge, UK, July 2007*. Cambridge Environmental Research Consultants. 2007.
- [110] L Patruno and M Ricci. "On the generation of synthetic divergence-free homogeneous anisotropic turbulence". In: *Computer Methods in Applied Mechanics and Engineering* 315 (2017), pp. 396–417.
- [111] M. Bervida et al. "Synthetic generation of the atmospheric boundary layer for wind loading assessment using spectral methods". In: *Journal of Wind Engineering and Industrial Aerodynamics* 196 (2020), p. 104040.
- [112] Joel H Ferziger, Milovan Perić, and Robert L Street. *Computational methods for fluid dynamics*. Vol. 3. Springer, 2002.
- [113] Claës Dyrbye and Svend Ole Hansen. *Wind loads on structures*. 1997.

-
- [114] NJ Cook and JR Mayne. "A refined working approach to the assessment of wind loads for equivalent static design". In: *Journal of Wind Engineering and Industrial Aerodynamics* 6.1-2 (1980), pp. 125–137.
- [115] P. Gousseau, B. Blocken, and G.J.F. van Heijst. "Quality assessment of Large-Eddy Simulation of wind flow around a high-rise building: Validation and solution verification". In: *Computers & Fluids* 79 (2013), pp. 120–133.
- [116] Yong Cao, Tetsuro Tamura, and Hidenori Kawai. "Investigation of wall pressures and surface flow patterns on a wall-mounted square cylinder using very high-resolution Cartesian mesh". In: *Journal of Wind Engineering and Industrial Aerodynamics* 188 (2019), pp. 1–18.
- [117] B. Blocken. "50 years of computational wind engineering: past, present and future". In: *Journal of Wind Engineering and Industrial Aerodynamics* 129 (2014), pp. 69–102.
- [118] Yukio Tamura and Pham Van Phuc. "Development of CFD and applications: Monologue by a non-CFD-expert". In: *Journal of Wind Engineering and Industrial Aerodynamics* 144 (2015), pp. 3–13.
- [119] Xingwang Zhao et al. "Optimal design of an indoor environment by the CFD-based adjoint method with area-constrained topology and cluster analysis". In: *Building and Environment* 138 (2018), pp. 171–180.
- [120] Xuelin Zhang et al. "Pedestrian-level wind conditions in the space underneath lift-up buildings". In: *Journal of Wind Engineering and Industrial Aerodynamics* 179 (2018), pp. 58–69.
- [121] C García-Sánchez, G Van Tendeloo, and C Gorlé. "Quantifying inflow uncertainties in RANS simulations of urban pollutant dispersion". In: *Atmospheric Environment* 161 (2017), pp. 263–273.
- [122] C García-Sánchez, J van Beeck, and C Gorlé. "Predictive large eddy simulations for urban flows: Challenges and opportunities". In: *Building and Environment* 139 (2018), pp. 146–156.
- [123] A Dagneu and Girma T Bitsuamlak. "Computational evaluation of wind loads on buildings: a review". In: *Wind Struct* 16.6 (2013), pp. 629–660.
- [124] Marie Skytte Thordal et al. "Towards a standard CFD setup for wind load assessment of high-rise buildings: Part 2–Blind test of chamfered

- and rounded corner high-rise buildings". In: *Journal of Wind Engineering and Industrial Aerodynamics* 205 (2020), p. 104282.
- [125] Jingxue Wang et al. "Characteristics of conical vortices and their effects on wind pressures on flat-roof-mounted solar arrays by LES". In: *Journal of Wind Engineering and Industrial Aerodynamics* 200 (2020), p. 104146.
- [126] Günter Schewe. "Sensitivity of transition phenomena to small perturbations in flow round a circular cylinder". In: *Journal of fluid mechanics* 172 (1986), pp. 33–46.
- [127] B Rocchio, A Mariotti, and MV Salvetti. "Flow around a 5: 1 rectangular cylinder: Effects of upstream-edge rounding". In: *Journal of Wind Engineering and Industrial Aerodynamics* 204 (2020), p. 104237.
- [128] IB Celik, ZN Cehreli, and I Yavuz. "Index of resolution quality for large eddy simulations". In: (2005).
- [129] Fengda Xing, Damith Mohotti, and Kapil Chauhan. "Study on localised wind pressure development in gable roof buildings having different roof pitches with experiments, RANS and LES simulation models". In: *Building and Environment* 143 (2018), pp. 240–257.
- [130] Jingxue Wang et al. "LES study of wind pressure and flow characteristics of flat-roof-mounted solar arrays". In: *Journal of Wind Engineering and Industrial Aerodynamics* 198 (2020), p. 104096.
- [131] Xing Zheng, H Montazeri, and B Blocken. "CFD simulations of wind flow and mean surface pressure for buildings with balconies: Comparison of RANS and LES". In: *Building and Environment* 173 (2020), p. 106747.
- [132] Pham Van Phuc et al. "Wind pressure distributions on buildings using the coherent structure Smagorinsky model for LES". In: *Computation* 6.2 (2018), p. 32.
- [133] Tsuyoshi Nozu et al. "Mesh-adaptive LES for wind load estimation of a high-rise building in a city". In: *Journal of Wind Engineering and Industrial Aerodynamics* 144 (2015), pp. 62–69.

- [134] Andrea Cimarelli, Adriano Leonforte, and Diego Angeli. “Direct numerical simulation of the flow around a rectangular cylinder at a moderately high Reynolds number”. In: *Journal of Wind Engineering and Industrial Aerodynamics* 174 (2018), pp. 39–49.
- [135] Akira Yoshizawa. “Statistical theory for compressible turbulent shear flows, with the application to subgrid modeling”. In: *The Physics of fluids* 29.7 (1986), pp. 2152–2164.
- [136] Hilary Weller. “Controlling the computational modes of the arbitrarily structured C grid”. In: *Monthly Weather Review* 140.10 (2012), pp. 3220–3234.
- [137] B En et al. “Eurocode 1: Actions on Structures—Part 1–4: General Actions—Wind Actions”. In: (2005).
- [138] ESDU. “Characteristics of Atmospheric Turbulence Near the Ground”. In: *Engineering Sciences Data Unit, IHS Group* (2001).
- [139] Giovanni Solari. “Gust buffeting. I: Peak wind velocity and equivalent pressure”. In: *Journal of Structural Engineering* 119.2 (1993), pp. 365–382.
- [140] X. Wu. “Inflow turbulence generation methods”. In: *Annual Review of Fluid Mechanics* 49 (2017), pp. 23–49.
- [141] Charles Mockett, Haase Werner, and Dieter Schwamborn. *Go4Hybrid: Grey Area Mitigation for Hybrid RANS-LES Methods*. Springer-Verlag, 2018.
- [142] CNR. “CNR-DT 207 R1/2018: Istruzioni per la valutazione delle azioni e degli effetti del vento sulle costruzioni”. In: (2018).
- [143] Rescale. *The Real Cost of High Performance Computing*. <https://resources.rescale.com/>. 2020 (accessed: 15,12,2020).
- [144] Edward Walker. “The real cost of a CPU hour”. In: *Computer* 42.4 (2009), pp. 35–41.
- [145] M Majowiecki. “Snow and wind experimental analysis in the design of long-span sub-horizontal structures”. In: *Journal of Wind Engineering and Industrial Aerodynamics* 74 (1998), pp. 795–807.
- [146] BJ Vickery and M Majowiecki. “Wind induced response of a cable supported stadium roof”. In: *Journal of Wind Engineering and Industrial Aerodynamics* 42.1-3 (1992), pp. 1447–1458.

Bibliography

- [147] CNR. *Guide for the assessment of wind actions and effects on structures—CNR-DT 207/2008*. 2008.
- [148] Ning Su, Shitao Peng, and Ningning Hong. “Analyzing the background and resonant effects of wind-induced responses on large-span roofs”. In: *Journal of Wind Engineering and Industrial Aerodynamics* 183 (2018), pp. 114–126.
- [149] Osamu Nakamura et al. “A case study of wind pressure and wind-induced vibration of a large span open-type roof”. In: *Journal of Wind Engineering and Industrial Aerodynamics* 52 (1994), pp. 237–248.
- [150] Ming Gu and Xuan-Yi Zhou. “An approximation method for resonant response with coupling modes of structures under wind action”. In: *Journal of wind engineering and industrial aerodynamics* 97.11-12 (2009), pp. 573–580.
- [151] You Lin Xu et al. “Pseudo-excitation method for vibration analysis of wind-excited structures”. In: *Journal of Wind Engineering and Industrial Aerodynamics* 83.1-3 (1999), pp. 443–454.
- [152] DM Huang, LD Zhu, and W Chen. “Covariance proper transformation-based pseudo excitation algorithm and simplified SRSS method for the response of high-rise building subject to wind-induced multi-excitation”. In: *Engineering Structures* 100 (2015), pp. 425–441.
- [153] M Kasperski and H.J. Niemann. “The LRC (load-response-correlation)-method a general method of estimating unfavourable wind load distributions for linear and non-linear structural behaviour”. In: *Journal of Wind Engineering and Industrial Aerodynamics* 43.1-3 (1992), pp. 1753–1763.
- [154] Ming Gu and Youqin Huang. “Equivalent static wind loads for stability design of large span roof structures”. In: *Wind and Structures* 20.1 (2015), pp. 95–115.
- [155] Tetsuro Tamura, Kojiro Nozawa, and Koji Kondo. “AIJ guide for numerical prediction of wind loads on buildings”. In: *Journal of Wind Engineering and Industrial Aerodynamics* 96 (2006), pp. 1974–1984.
- [156] American Society of Civil Engineers. *Minimum Design Loads for Buildings and Other Structures*. ASCE/SEI 7-10. 2013.

- [157] Yue Zhang, Wagdi G Habashi, and Rooh A Khurram. "Predicting wind-induced vibrations of high-rise buildings using unsteady CFD and modal analysis". In: *Journal of Wind Engineering and Industrial Aerodynamics* 136 (2015), pp. 165–179.
- [158] Anil K Chopra. *Dynamics of structures*. 1975.
- [159] L Patruno et al. "An efficient approach to the evaluation of wind effects on structures based on recorded pressure fields". In: *Engineering Structures* 124 (2016), pp. 207–220.
- [160] L. Patruno et al. "An efficient approach to the determination of Equivalent Static Wind Loads". In: *Journal of Fluids and Structures* 68 (2017), pp. 1–14.
- [161] *MJW structures*. <https://www.majowiecki.com/>. Accessed: 12-01-2022.
- [162] Charles Hirsch. *Numerical computation of internal and external flows: The fundamentals of computational fluid dynamics*. Elsevier, 2007.
- [163] R.I Issa. "Solution of the implicitly discretised fluid flow equations by operator-splitting". In: *Journal of Computational Physics* 62.1 (1986), pp. 40–65.
- [164] Luigi Carassale and Michela Marré Brunenghi. "Statistical analysis of wind-induced pressure fields: A methodological perspective". In: *Journal of Wind Engineering and Industrial Aerodynamics* 99.6 (2011), pp. 700–710.
- [165] M. Liu, X. Chen, and Q. Yang. "Estimation of peak factor of non-Gaussian wind pressures by improved moment-based Hermite model". In: *Journal of Engineering Mechanics* 143.7 (2017), p. 06017006.
- [166] Ji Young Kim et al. "Long-term monitoring of wind-induced responses of a large-span roof structure". In: *Journal of Wind Engineering and Industrial Aerodynamics* 99.9 (2011). 9th UK Conference on Wind Engineering (September, 2010), pp. 955–963.
- [167] Massimo Majowiecki and Nicola Cosentino. "Dynamic aspects of the New Braga Stadium large span roof". In: *Proceedings of IASS symposium*. 2007.
- [168] Yusik Kim, Ian P Castro, and Zheng-Tong Xie. "Divergence-free turbulence inflow conditions for large-eddy simulations with incompressible flow solvers". In: *Computers & Fluids* 84 (2013), pp. 56–68.

Bibliography

- [169] Nicolas Blaise and Vincent Denoël. “Principal static wind loads”. In: *Journal of Wind Engineering and Industrial Aerodynamics* 113 (2013), pp. 29–39.